Relativistic Channeling with Applications to Inertial Confinement Fusion

Luke Ceurvorst

Magdalen College

University of Oxford

A thesis submitted for the degree of

Doctor of Philosophy

Trinity 2017

Acknowledgements

Personal

There are several people whom I'd like to thank for all of their support, both academic and personal, without whom this thesis would not have been possible. First, I'd like to thank my supervisor, Peter Norreys, for all of the support, guidance, and opportunities he has given me over the years. Through him, I was able to grow my experimental skills through several campaigns, gain exposure to multiple branches of plasma physics, and see the big picture behind the research.

I'm also appreciative of Justin Wark, my co-supervisor early in my thesis. He provided key guidance and insights as I began my research and allowed me the freedom to pursue explore channeling rather than opacities.

I'd also like to acknowledge the members of my group, Naren Ratan, Muhammad Kasim, James Sadler, Kevin Glize, and Alex Savin, for all of their advice and insights in the office and for their support outside of it. Other officemates, especially Thomas Preston and Orlando Circosta, also deserve to be named here. I am extremely grateful to have been able to work alongside such fantastic individuals and wonderful friends.

I also owe many thanks to the researchers at the Central Laser Facility. Raoul Trines in particular was there on day one to teach me how particle-in-cell codes work and helped me get my first simulations up and running, not to mention countless conversations about any bugs or strange results along the way.

Speaking of simulations, I'd like to thank Marija Vranic and Jorge Vieira for always making time when I would hit a wall with OSIRIS. They have been a huge help, as have all of those at the Instituto Superior Técnico who work so tirelessly on this code.

I was fortunate enough to participate in multiple experiments at the OMEGA and OMEGA EP facilities. I have to thank Wolfgang Theobald, Dustin Froula, and Steven Ivancic for the opportunity to work with them and learn what it takes to design and execute a successful experiment. I will carry the experience gained at these experiments with me throughout my career.

And of course, I have to express my love and endless appreciation to those closest to me. My family, Brenda, Stephen, Sarah, Matthew, and Christian Ceurvorst have been there for me every step of the way and have been continuously rooting for

me. My partner, Ines Gundlach, has not only been my greatest cheerleader, but has also painstakingly proof-read all of my work. Finally, my friends have been there to keep me sane throughout this whole process. I would not be where I am, academically, professionally, nor personally, without any of you.

Institutional

Many thanks are due to the funding institutions that made this thesis possible. I'd like to thank the OSIRIS consortium for the use of OSIRIS. I would also like to thank the staff of the Central Laser Facility and the Computer Science Department at the Rutherford Appleton Laboratory for the use of the SCARF-LEXICON computer cluster, as well as the ARCHER UK National Supercomputing Service. Much of this work has been carried out within the framework of the EUROfusion Consortium and has received funding from the Euratom research and training programme 2014-2018 under grant agreement No 633053. The views and opinions expressed herein do not necessarily reflect those of the European Commission. I further acknowledge the support of the Plasma HEC Consortium, EPSRC Grant EP/L00023711. The experimental results contained herein are based upon work supported by the Department of Energy National Nuclear Security Administration under Award No. DE-NA0001944 and the New York State Energy Research and Development Authority. I'd also like to acknowledge DOE grant DE-SC0014666 for the support of this work. The FLASH code used in this work was developed in part by the DOE NNSA ASC- and DOE Office of Science ASCR-supported Flash Center for Computational Science at the University of Chicago. The support of DOE does not constitute an endorsement by DOE of the views expressed in this thesis. Part of the research has been supported by JSPS-S class fund (15H05751-70171741).

Abstract

The goal of controlled fusion energy has been pursued by the international community for decades. The majority of research into inertial confinement fusion, one branch of fusion research as a whole, has been focused on central hot spot ignition. However, alternative approaches such as fast ignition present the opportunity to achieve higher gains with reduced symmetry requirements, making them ideal for fusion energy production.

One important component of the original fast ignition scheme is the formation of a persistent low-density channel through an inhomogeneous plasma. This thesis revolves around channeling with laser pulses of highly relativistic intensities through plasmas relevant to fast ignition research, an intensity regime which has not received thorough attention in the existing literature. In this thesis, several particle-in-cell simulations are run to analyze various schemes in an effort to gain greater control over the channeling process.

An expanded physical model of the hosing instability that includes relativistic laser intensities and near-critical densities is presented and derives the density dependence of the hosing equation. This is then tested through simulations, and an examination of its consequences on multiple-pulse channeling schemes is conducted. The results show that the hosing instability grows more rapidly in dense plasmas, reducing the benefits of the multiple-pulse scheme when using realistic pulses of relativistic intensity.

Phenomena such as a ponderomotive self-correction mechanism, self-focusing-induced filamentation, and a modulated wavepacket known as the "pathfinder" pulse all become more relevant at higher pulse intensities. These have interesting consequences for future channeling schemes.

Finally, an experiment performed at the OMEGA EP facility at the Laboratory for Laser Energetics in Rochester, NY, USA is presented and analyzed. This experiment explored the effects of pulse timing, intensity, and focal position on channel formation. The findings of this experiment have important consequences for experimental design and have already improved the results of integrated fast ignition experiments.

Contents

List of Figures

List of Abbreviations

Bold fonts . . Used in equations to represent vectors. Non-bold versions of the same symbols represent their magnitude unless otherwise specified.

Subscripts . . e and i are used to denote the electron and ion species respectively. In the remainder of this list, α will be used as a general placeholder.

$\langle\cdot\rangle$ . . . . Cycle- or time-average.

$\hat{\cdot}$ . . . . Unit vector.

∂_β . . . . Shorthand for $\frac{\partial}{\partial\beta}$.

1D, 2D, 3D . . One-, two-, or three-dimensional, referring in this thesis to spatial dimensions in an image.

$\mathbf{A}$ . . . . Vector potential, typically used to define a pulse in the Coulomb gauge within this work.

$\mathbf{B}$ . . . . Magnetic field as a function of position.

c . . . . Speed of light.

c_s . . . . Sound speed, generally given for the ion acoustic sound speed unless otherwise indicated. $c_s = (Zk_BT_e/m_i)^{1/2}$.

C_β . . . . Heat capacity at constant pressure ($\beta = p$) or constant volume ($\beta = V$).

e . . . . Elementary charge.

$\mathbf{E}$ . . . . Electric field as a function of position.

$\mathbf{j}$ . . . . Current as a function of position within the plasma. $\mathbf{j} = \sum_\alpha q_\alpha n_\alpha \mathbf{v}_\alpha$.

$\mathbf{k}$ . . . . Angular wavenumber of a wave.

m_α . . . . Mass of a species.

n_α . . . . Density of a species as a function of position within the plasma.

n_c . . . . Critical density, or the maximum density to which a pulse is able to propagate into a plasma as defined in Section 2.4.

$\mathbf{p}_\alpha$ . . . . Momentum of a species as a function of position within the plasma.

P_α . . . . Pressure of a species as a function of position within the plasma.

q_α . . . . Charge of a species. For example, $q_e = -e$ and $q_i = Z_i e$.

t . . . . Time as measured in the laboratory frame.

$\mathbf{v}_\alpha$ . . . . Velocity of a species as a function of position within the plasma.

v_g . . . . Group velocity of a wave, $v_g = d\omega/dk$, or the rate at which modulations to a wave's envelope propagate in space.

v_{th} . . . . Root-mean-square thermal velocity, typically of the electron species. $v_{\mathrm{th}} = (k_B T_e/m_e)^{1/2}$.

v_φ . . . . Phase velocity of a wave, $v_\varphi = \omega/k$, or the rate at which the phase of a wave propagates in space.

W . . . . Spot size of a pulse.

Z_α . . . . Charge state.

γ . . . . Lorentz factor.

γ_e . . . . Specific heat ratio for the electron species, C_p/C_V.

ε_0 . . . . Permittivity of free space.

η . . . . Index of refraction.

λ_D . . . . Debye length, or the e-fold length of field shielding within a plasma as defined in Section 2.2.

μ_0 . . . . Vacuum permeability.

$\nu_{\alpha\beta}$ . . . . Collision rate between species α and species β. Note that these may be the same or different species.

ρ . . . . Charge density as a function of position within the plasma. $\rho = \sum_\alpha q_\alpha n_\alpha$.

Φ . . . . Electric scalar potential.

φ . . . . Typically used as the phase of a wave, $\varphi = \mathbf{k} \cdot \mathbf{x} - \omega t$ for a traveling monochromatic wave.

ω . . . . Angular frequency of a wave.

ω_c . . . . Cyclotron frequency, $\omega_c = q_\alpha B/m_\alpha$, or the angular frequency of a charged particle about a uniform magnetic field.

ω_h . . . . Upper hybrid frequency, or the modified angular frequency of electron oscillation perpendicular to a magnetic field present in a plasma as defined in Section 2.3.

ω_L . . . . Angular frequency of a laser pulse.

ω_p . . . . The plasma frequency, or the natural angular frequency of electron oscillation present in a plasma as derived in Section 2.1. $\omega_p^2 = n_e e^2 / m_e \varepsilon_0$.

Ω_p . . . . The plasma ion frequency as derived in Section 2.3.2. $\Omega_p^2 = n_i e^2 / m_i \varepsilon_0$.

AFR . . . . . . Angular filter refractometry. See Section 4.3.4.

BC . . . . Boundary conditions. See Section 3.1.

CLF . . . . . . Central Laser Facility, a part of the Rutherford Appleton Laboratory.

ICF . . . . . . Inertial confinement fusion.

IST . . . . Instituto Superior Técnico, a school of engineering and part of the Universidade de Lisboa (University of Lisbon).

LLE . . . . . . Laboratory for Laser Energetics, a part of the University of Rochester.

MCF . . . . . . Magnetic confinement fusion.

PIC . . . . . . Particle-in-cell. See Section 3.1.

PPC . . . . . . The number of particles per cell. See Section 3.1.

1
Introduction

Nuclear fusion has long been seen as an ultimate goal in the pursuit of clean, sustainable energy. It promises to produce carbon-free energy with far less radioactive waste than today's fission power plants while simultaneously eliminating the risk of a reactor meltdown. This is achieved by using a common isotope of hydrogen as fuel. However, attaining this era-defining technology has remained out of reach since the mid-twentieth century. Research continues today in two primary subdivisions: magnetic confinement fusion (MCF) and inertial confinement fusion (ICF). This chapter introduces the topic of inertial confinement fusion and motivates and outlines the work presented in the remainder of this thesis.

1.1 Nuclear Fusion and Inertial Confinement

A nuclear reaction is exothermic when the mass of the reactants exceeds the mass of the products, and energy is released according to Einstein's famous equation, $\mathcal{E} = \Delta mc^2$ where $\mathcal{E}$ is the energy, Δm the mass difference between the reactants and products, and c the speed of light. Another way to look at this is to examine the binding energy of a nucleus. The binding energy is defined as the energy corresponding to the difference between the sum of the nucleons' masses and the mass of the total nucleus itself. To formalize this [1]:

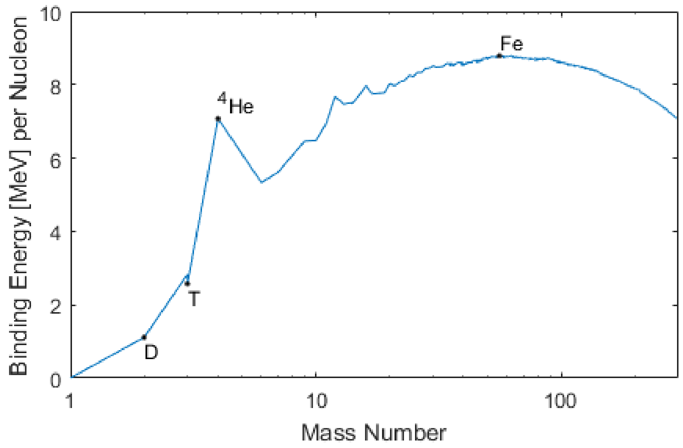

Figure 1.1: Binding energy per nucleon versus atomic mass. As can be seen, the binding energy per nucleon for elements lighter than iron will generally increase with mass number while those heavier than iron will decrease. This accounts for the difference between fusion and fission. Data taken from the National Institute of Standards and Technology [2].

$$B \equiv [Zm_p + (A - Z)m_n - m]c^2 \tag{1.1}$$

where B is the binding energy, Z is the atomic number of the atom, A the atomic mass number, m_p the proton mass, m_n the neutron mass, and m the atomic mass. It is instructive to examine the binding energy per nucleon for various isotopes as plotted in Figure 1.1. As can be seen from this figure, the binding energy per nucleon increases through approximately iron, $A = 56$, after which it begins to decline again. Combining atoms significantly lighter than iron will produce an atom with greater binding energy per nucleon. In other words, the mass of the nucleons will exceed the mass of the atom by a greater margin, resulting in lighter products than reactants. This difference is released as energy. The same argument can be applied to splitting elements with mass significantly greater than iron. This is how both fusion and fission are capable of producing energy despite being superficially opposite processes.

The protons and neutrons which constitute the nucleus of an atom are held together through the strong nuclear force. However, this force is short-ranged and falls off much more rapidly than the Coulomb force which repels the nuclear protons. As a result of the balance between these attractive and repulsive forces, there is a point where a proton will be in an unstable equilibrium. The potential energy at this point – where the potential at infinity is set to be zero – is the Coulomb barrier. If two particles collide with energy exceeding the Coulomb barrier, they will overcome the electromagnetic repulsion, thereby allowing the strong force to take hold and synthesize a new atom.

These high collision velocities are achieved by heating a plasma, thereby increasing the average kinetic energy of the particles. For fusion to occur in the laboratory, temperatures in excess of 10^7 K are required. Further, to ensure that a majority of the fuel in a fusion reactor has the opportunity to collide and fuse, the plasma must be either extremely dense or confined for extended periods of time. High density approaches are pursued in ICF while much longer confinement times at lower densities are the subject of MCF.

These requirements were formalized by Lawson [1, 3] by balancing the energy produced from these reactions to the energy losses of a system due to various processes such as diffusive and bremsstrahlung losses. This produced the Lawson criterion ubiquitous throughout fusion research:

$$n\tau_E T > 3.3 \times 10^{15}\,\mathrm{cm}^{-3}\,\mathrm{s}\,\mathrm{keV} \approx 5.2\,\mathrm{atm}\,\mathrm{s} \tag{1.2}$$

where n and T are the density and temperature of the fuel respectively, and τ_E is the confinement time, formally defined as the time after which the energy content of the plasma has been matched by diffusive losses. Note that the right-hand side of this equation was found by taking the absolute minimum of a more complicated function. Thus the triple product may have a greater threshold requirement depending on the plasma parameters.

ICF attempts to achieve this criterion by compressing a target to extremely high densities, thus reducing the required confinement time. This is most commonly achieved by using a hollow or gas-filled shell of solid density fuel, typically a mix of deuterium and tritium, as a target with an outer layer of ablator material, often polystyrene. Laser pulses are then used to heat the ablator either through direct incidence (direct-drive) or by heating a high-Z container known as a hohlraum (indirect-drive). This hohlraum then emits x-rays which illuminate the target.

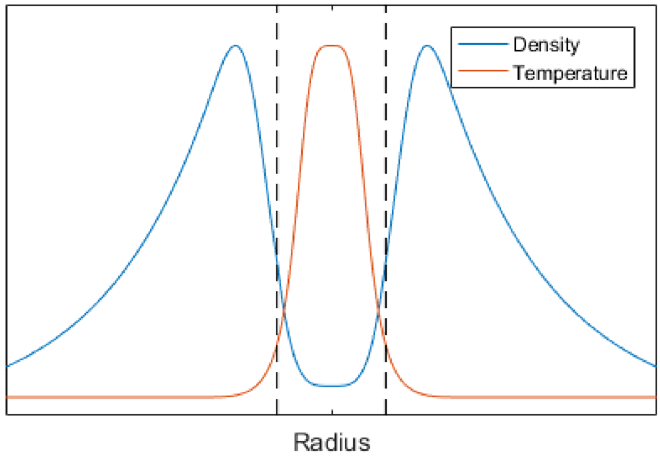

Figure 1.2: Density and temperature schematic of a compressed target in central hot spot ignition. The temperature in the central hot spot of the compressed target increases greatly to create an even pressure throughout the core. The vertical dashed lines indicate the approximate central hot spot region.

Indirect-drive has historically been the primary implosion method as it is capable of providing smoother irradiation, thus causing a more symmetric implosion with a lower chance of shell breakup. Further, indirect-drive produces greater mass ablation [1]. Takabe *et al.* first showed in 1985 that this leads to a reduction in the growth rate of the Rayleigh-Taylor instability, a particularly destructive fluid instability which leads to shell breakup, thereby allowing a more stable implosion to take place [4]. However, this scheme has greatly reduced efficiency as the coupling of the laser energy to the x-ray drive is low due to escaped radiation and hohlraum heating. Further, indirect drive has a more complicated geometry as the target must be enclosed inside the hohlraum, which is typically cylindrically shaped. As a result, research into direct-drive has increased in recent years, especially as pulse profile smoothing techniques have improved [5–8].

In either direct- or indirect-drive, the incident rays ablate the outer layer of the target which expands outwards. Consequently, the rocket effect causes the rest of the target to compress inwards at velocities on the order of $10^7\,\mathrm{cm\,s^{-1}}$ in what is known as the drive phase [1]. The drive pulses then cease and the capsule continues to compress through its own inertia during the coast phase. As the pressure in the centre of the capsule begins to exceed the shell pressures, the deceleration phase begins, converting the shell's kinetic energy into internal energy until stagnation is finally reached. The most heavily researched scheme today is central hot spot ignition [9]. Upon reaching stagnation in this scheme, the target has been isobarically compressed, and the centre of the target has a much lower density than the surrounding compressed shell. To maintain a constant pressure, the temperature of the centre rises dramatically. A schematic of this effect is shown in Figure 1.2.

The temperature at the core of this implosion will be hot enough for fusion to begin. Deuterium and tritium are the most common isotopes to be used as fuel as they have the greatest fusion cross-section, and, as illustrated in Figure 1.3, their maximum cross-section occurs at the lowest temperature, just 64 keV [1]. The total rest energy of deuterium and tritium is slightly lower than an excited state of ^{5}He, separated by just 107 keV [10]. As a result, over 99% of D-T reactions produce ^{5}He as an intermediate product [10, 11]. This unstable isotope of helium then decays into ^{4}He+n and releases 17.6 MeV of energy. This is one of the largest yields of any fusion process. This and other hydrogen reactions of interest include [1]:

$$\begin{aligned} &\mathrm{D+T} \rightarrow \alpha\ (3.5\,\mathrm{MeV}) + \mathrm{n}\ (14.1\,\mathrm{MeV}) \\ &\mathrm{D+D} \rightarrow \mathrm{T}\ (1.01\,\mathrm{MeV}) + \mathrm{p}\ (3.03\,\mathrm{MeV}) \\ &\mathrm{D+D} \rightarrow {}^3\mathrm{He}\ (0.82\,\mathrm{MeV}) + \mathrm{n}\ (2.45\,\mathrm{MeV}) \\ &\mathrm{T+T} \rightarrow \alpha + 2\mathrm{n} + 11.3\,\mathrm{MeV} \end{aligned} \tag{1.3}$$

As these reactions continue to occur, alpha particles continue to heat the surrounding plasma through Coulomb collisions. If the Lawson criterion is met, this creates more energy than is lost to convection and radiation losses, and a burn wave forms, igniting the capsule and burning a large fraction of the fuel. It is worth noting that the confinement time in ICF can be determined by the time a sound wave takes to travel across the capsule. This value is given roughly as R/c_s where R is the compressed capsule's radius and $c_s = (k_B T_e/m_i)^{1/2}$ is the sound speed. This can then be substituted into the Lawson criterion and simplified to give [1]:

$$\rho R = n\tau_E m_i c_s \geq 1\,\mathrm{g\,cm^{-2}} \tag{1.4}$$

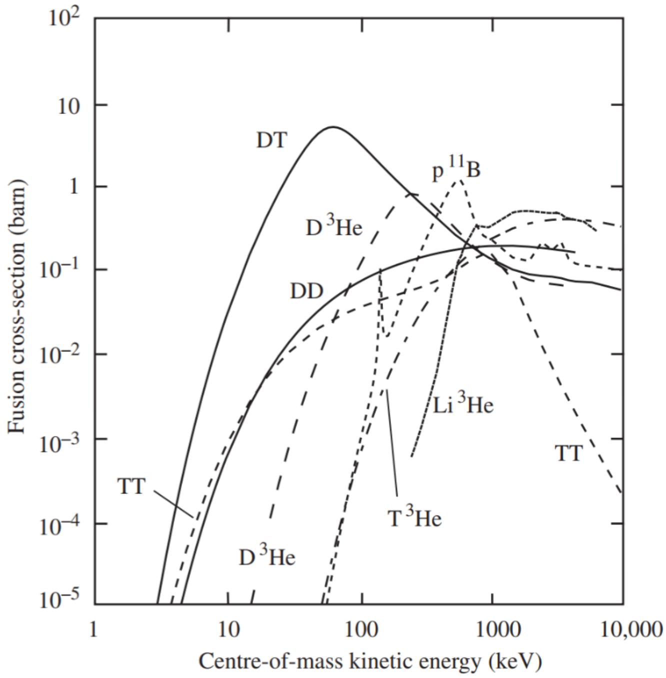

Figure 1.3: Fusion cross-section versus centre-of-mass energy for various fuel sources. The DD curve represents the sum of all DD reactions. Image taken from Atzeni and Meyer-ter-Vehn [1]

where $\rho = m_i n$ is the mass density of the plasma. This puts a minimum on ρR, known as the areal density. As with Equation 1.2, the right-hand side of this equation is an absolute minimum and the actual requirement will generally be greater. Areal density also appears when determining the ability of the plasma to stop and contain alpha particles. As such, it is a useful measure of the compression of a plasma.

This approach to fusion has shown great progress over the years. Recently, experiments at the National Ignition Facility at the Lawrence Livermore National Laboratory in California, USA have produced results reaching the alpha-heating regime – where more energy was produced by the implosion than was incident upon the target [12]. However, the total input required to deliver that energy was still far greater due to inefficiencies in the delivery system such as hohlraum losses. Progress beyond this point and towards the burning plasma regime has proven difficult to accomplish. In order to produce the central hot spot, high implosion velocities are required. This necessitates the use of thin shells which are prone to hydrodynamic instabilities. These instabilities often lead to the breakup of the shell and the mixing of the shell material with the fuel [13–15]. This disrupts the fusion process, thereby limiting the gains thus far achievable with central hot spot ignition [16, 17].

1.2 Fast Ignition

An alternative approach to ignition in ICF was proposed by Max Tabak *et al.* in 1994 wherein the compression and ignition phases are separated [18]. In order to achieve this, the DT fuel capsule is compressed isochorically rather than isobarically to $\sim 400\,\mathrm{g\,cm^{-3}}$ with an areal density of $\sim 2\,\mathrm{g\,cm^{-2}}$. The requirements of this compression are greatly relaxed compared to conventional central hot spot ignition as the drive pulses do not need to ignite the capsule. This allows for much more stable and efficient implosions while still achieving high gains by permitting lower shell velocities to be used [19, 20]. These lower implosion velocities allow smaller in-flight-aspect-ratios (the ratio of shell radius to shell thickness) to be utilized to prevent shell breakup and thus allow more target mass to be imploded using the same driver energy [21].

Ignition is then triggered by a short-duration petawatt laser pulse which, upon hitting the critical isosurface of the surrounding plasma, generates a diverging beam of fast electrons. The fast electrons then travel forward to the dense core where they collisionally deposit their energy. Around 20 kJ of energy must be deposited in approximately 20 ps over a radius of about 20 µm in the compressed target for ignition to be achieved [22, 23]. This requires the divergence of the electron beam to be kept to a minimum, and the electrons must have energy in the 1-3 MeV range to be stopped collisionally in the compressed core [24].

In order to reduce the divergence of the electron beam and to give more control over the electron spectrum, the original fast ignition scheme proposed the concept of channeling [18]. Before the ignition pulse is sent into the plasma, another high-intensity beam propagates through the plasma, penetrating as close to the compressed core as possible. This creates a low-density channel which, if properly designed, could extend beyond the original critical surface, thus preventing the plasma from significantly altering the ignition pulse's properties and lending more control over the fast electron spectrum while minimizing total divergence. This concept was based in large part on early experimental work showing the expulsion of a plasma from a laser pulse's path in the early 1990s [25–27].

The energy requirements for the channeling beam to reach the critical surface of a plasma with a 430 μm scale length have been modeled with two-dimensional particle-in-cell codes and are expected to range between approximately 1.7 kJ and 20.4 kJ for channeling intensities of $10^{18}\,\mathrm{W\,cm^{-2}}$ and $10^{21}\,\mathrm{W\,cm^{-2}}$ respectively [28]. While sizable, these energies are still marginal in comparison to the megajoule implosions used at the National Ignition Facility. Further, by separating these pulses, the two beams may be optimized for their respective purposes.

Since the introduction of this approach, several experimental campaigns have been conducted to study various facets of fast ignition. These studies have ranged from scaled-down proof of concept experiments which successfully showed high-gain fusion efficiencies [29] to topic-specific studies of the coupling of the laser pulse to fast electrons [30,31] and the transport of these electrons through the plasma [32–35]. Research into channeling has been performed using both long-duration, low-intensity pulses [36,37] and short (≤ 1 ps), high-intensity ($\sim 10^{18}-10^{19}\,\mathrm{W\,cm^{-2}}$) pulses [38–40]. Still, several challenges continue to exist today, and due to the predicted increased energy requirements [28], the bulk of the literature studying the channeling process has neglected the ultra-intense regime ($\sim 10^{19} - 10^{21}\,\mathrm{W\,cm^{-2}}$).

1.3 Thesis Outline

This thesis focuses on the author's research into the application of ultra-intense beams to form channels in the context of inertial confinement fusion. This research was split between both numerical and experimental investigations. While contributions to several additional experiments were made, it would not be practical nor necessarily interesting to go into detail here, and as such, only those directly relevant to the thesis description are elucidated herein. The remainder of this work is then organized as follows.

Chapter 2 introduces the background theory necessary to examine the phenomena described in this thesis. This includes a brief introduction to the relevant plasma physics, the interaction of light with plasma, and the generation of channels both in underdense and overdense plasmas.

Chapter 3 presents the results of several numerical campaigns which were performed independently from experiments. This primarily includes the simulation of various schemes intended to provide greater control over the channeling process, an expanded physical model for the hosing instability, and various simulations designed to explore the consequences of this model. Through the study of these simulations, a ponderomotive self-correction mechanism is described and a strong cause of filamentation is identified. Much of the work presented in this chapter has been published in the scientific literature [41].

Chapter 4 briefly discusses the generation of laser pulses and some of the diagnostics commonly used in this research. This chapter serves as an introduction for the following chapter.

Chapter 5 presents the results from a selection of the experiments which focused on the generation of channels in conditions relevant to fast ignition inertial confinement fusion. This includes two fully-integrated fast ignition experiments. However, as the author's primary contributions to these experiments were to advise and examine the channeling pulse, the analysis of these experiments as presented here limits its scope to the performance of these pulses and then utilizes the results to contextualize the central experiment of this thesis: an OMEGA EP experiment focused on optimizing the channeling depth of a pulse. This optimization experiment, for which the writer is the first author, has been presented at two conferences in April 2017, winning the "Best Poster Competition" prize at the 44$^{\text{th}}$ IoP Plasma Physics Conference and an honorable mention at the Omega Laser User Group meeting. This chapter forms the basis of a manuscript which is being drafted for submission to Physical Review.

Finally, Chapter 6 summarizes the work presented in this thesis, what conclusions can be drawn from it, and plans for further research on this topic.

1.4 Author Contributions

Throughout this manuscript, the contributions of various collaborators are noted and discussed. However, for clarity, this section details the specific contributions of the author and his collaborators to the work presented here.

Chapters 1, 2, and 4 summarize the preexisting results in the literature, and thus are the outcome of the tireless work of numerous others. The author's own research and views are presented in Chapters 3, 5, and 6.

All OSIRIS [42] simulations analysed in this thesis were performed by the author. This work was possible thanks to the hard work of the OSIRIS consortium, consisting of the Instituto Superior Técnico (IST) of the University of Lisbon and the University of California, Los Angeles, who themselves wrote, tested, and continuously developed this particle-in-cell code. The fine-tuning and verification of these simulations came from several useful and detailed discussions, primarily with Raoul Trines of the Central Laser Facility (CLF), part of the Rutherford Appleton Laboratory, and Marija Vranic of IST. The plasma density scale lengths used in these simulations were based on Hydra [43] simulations run by Robbie Scott of CLF, though the author later confirmed these results by running Hydra simulations of his own.

The experiments discussed in Chapter 5 were designed by Wolfgang Theobald and Steven Ivancic of the Laboratory for Laser Energetics (LLE), a branch of the University of Rochester. The author advised on the channeling beam's parameters, suggesting the focal position and pulse intensities be investigated in the parameter scan experiment. Additionally, all of the data analysis for the parameters scan experiment apart from Osaka University's multi-angle electron spectrometer was performed by the author. The electron spectrometer was analysed by Hideaki Habara of Osaka University. The FLASH [44] simulations were performed by Shu Zhang of the University of California, San Diego, and the technique for analysing the angular filter refractometry (AFR) results was invented by Dan Haberberger and colleagues of LLE [45]. While the final script for analysing these AFR images was written by the author, it was heavily based upon discussions with Steven Ivancic and his scripts. The fully-integrated fast ignition experiments were analysed by the LLE team. The author provided particle-in-cell simulation support for this experiment to investigate the effects of temperature and beam speckling on filamentation.

Finally, the analysis and simulation design presented in this thesis was influenced by detailed discussions with the author's group. Special acknowledgements go to Naren Ratan, Muhammad Kasim, James Sadler, Alex Savin, Kevin Glize, and Peter Norreys for their crucial advice and guidance on the interpretation of many of the results shown herein.

2
The Physics of Laser-Plasma Interactions

Plasma is the most abundant state of visible matter in the universe and constitutes several celestial bodies such as stars, gaseous nebulae, the Van Allen radiation belts, and indeed the majority of interstellar hydrogen. More importantly for this thesis, it is the state of matter found in controlled nuclear fusion research, and thus it is important to understand both what a plasma is and how it behaves. In general, a plasma is not simply any ionized gas. Rather, it must exhibit three additional traits [46].

A plasma must exhibit what is known as "collective behavior". In a neutral gas, particles are unaffected by electromagnetic fields and respond only to collisions. As a result, fluid evolution within such a gas is defined by local interactions. However, in a plasma, the particles have charges, which means that local concentrations and movements give rise to electric and magnetic fields which affect distant particles. As will be discussed in Section 2.6.1, a sufficiently hot plasma can even be considered collisionless, allowing collisions to be neglected entirely, and the plasma still evolves through long-range electromagnetic interactions. Collective behavior then means that the motion of a plasma depends not only on local conditions, but on the entire state of the plasma.

Additionally, a plasma must be "quasi-neutral". As will be discussed in Section 2.2, when a probe charge is placed within a plasma, the electrons move swiftly to shield out the effects of the electric and magnetic fields. This is done in such a way that the field from the external charge is attenuated over a distance known as the Debye length. Thus, if the dimensions of the plasma are much greater than the Debye length, the plasma remains largely neutral, and the ion charge density remains nearly identical to the electron charge density. Still, slight density fluctuations are present to allow interesting electromagnetic interactions to occur. Further, for shielding to be a statistically valid concept, there must be enough particles within the plasma to perform this shielding. Thus a plasma must be both large in spatial extent compared to the Debye length, and it must have a large enough density that many particles are contained within a Debye-length sphere.

Finally, the evolution of the plasma must be defined predominantly by electromagnetic forces rather than hydrodynamic forces. As will be seen in Section 2.1, particles in a plasma naturally oscillate. This behavior has a large effect on the macro-behavior of the plasma. However, if the charged particles collide with neutral atoms faster than they naturally oscillate, this behavior is suppressed and the gas tends towards hydrodynamic evolution. Thus the frequency of typical oscillations must exceed the charge-neutral collision frequency.

The remainder of this chapter presents the laser-plasma interaction theory required to understand the evolution of a plasma. This begins with the basics of a plasma, working primarily from the arguments of Chen [46], and continues on towards the specialized field of laser-plasma channeling as described in the existing literature. This is done to gain an understanding of the phenomena and analysis present throughout the subsequent chapters of this thesis.

2.1 The Plasma Frequency

The existence of two overlapping, oppositely charged fluids means that should any charge separation exist within the plasma, the fluids will adjust to shield out the electrostatic fields. Because the electrons are thousands of times lighter than the ions, the vast majority of movement will come from the electron species. In fact, many of the phenomena observed in plasmas using picosecond-duration laser pulses are explained with the assumption that the ions are fixed in space. In this case, one must only consider the equations governing the electron fluid along with the Poisson equation, which read respectively as [46]:

$$m_e n_e \left[\frac{\partial \mathbf{v}_e}{\partial t} + (\mathbf{v}_e \cdot \boldsymbol{\nabla})\, \mathbf{v}_e \right] = -n_e e \left(\mathbf{E} + \mathbf{v}_e \times \mathbf{B} \right) - \boldsymbol{\nabla} P_e - m_e n_e \nu_{ei} \left(\mathbf{v}_e - \mathbf{v}_i \right) \quad (2.1)$$

$$\frac{\partial n_e}{\partial t} + \boldsymbol{\nabla} \cdot (n_e \mathbf{v}_e) = 0 \quad (2.2)$$

$$\boldsymbol{\nabla} \cdot \mathbf{E} = \frac{e}{\varepsilon_0} \left(Z n_i - n_e \right) \quad (2.3)$$

Here m is the mass, n the density, $\mathbf{v}$ the velocity, and P the pressure of each species with e subscripts indicating they belong to the electron species and i subscripts indicating the ion species. Bold fonts indicate vectors. ν_{ei} is the electron-ion collision rate, Z the charge state, and t, e, $\mathbf{E}$, $\mathbf{B}$, and ε_0 all have their conventional assignments of time, elementary charge, electric field, magnetic field, and the permittivity of free space respectively.

Herein, Equation 2.1 shall be referred to as the electron fluid equation, and Equation 2.2 the electron continuity equation. They may be derived through kinetic theory which will briefly be outlined here. Assume a distribution function, $f_e(t, \mathbf{x}, \mathbf{v})$, for the electron species. In other words, f_e is defined so that the number of electrons between $\mathbf{x}_0$ and $\mathbf{x}_1$ with velocities between $\mathbf{v}_0$ and $\mathbf{v}_1$ is given by $\int_{\mathbf{x}_0}^{\mathbf{x}_1} \int_{\mathbf{v}_0}^{\mathbf{v}_1} f_e d\mathbf{v} d\mathbf{x}$. Assuming that the number of electrons remains constant and the force on the particles is entirely electromagnetic implies $df/dt = 0$. This yields the Vlasov equation:

$$\begin{aligned} 0 &= \frac{\partial f_e}{\partial t} + \frac{\partial \mathbf{x}}{\partial t} \cdot \frac{\partial f_e}{\partial \mathbf{x}} + \frac{\partial \mathbf{v}}{\partial t} \cdot \frac{\partial f_e}{\partial \mathbf{v}} \\ &= \frac{\partial f_e}{\partial t} + \mathbf{v} \cdot \boldsymbol{\nabla} f_e - \frac{e}{m_e} \left(\mathbf{E} + \mathbf{v}_e \times \mathbf{B} \right) \cdot \frac{\partial f_e}{\partial \mathbf{v}} \end{aligned} \quad (2.4)$$

The electron continuity equation is found by taking the zeroth moment of this equation, which simply means in this case to integrate over velocity space. Similarly, the electron fluid equation can be found by multiplying Equation 2.4 by $m_e \mathbf{v}$ and integrating over velocity space to take the first moment of the equation. The actual derivation from this point is omitted for brevity, though it should be noted that a roughly Maxwellian thermal distribution is assumed in these derivations. Further, isotropy is assumed so that the pressure effects may be treated with a scalar rather than a tensor value. The reader is referred to Chen [46] for a more thorough treatment.

Consider the case of a cold ($P_e = 0$), collisionless ($\nu_{ei} = 0$), uniform, and neutral plasma at rest with no external fields applied. Any charge separation would cause the electrons to move towards the ions in order to restore charge neutrality. However, because of their inertia, they would overshoot the ions and begin to oscillate about them. To see this, take a linear perturbation of the fluid variables about an equilibrium state. For example, let $n_e = n_{e0} + n_{e1}$ where n_{e0} is the equilibrium density and n_{e1} is the perturbation. Note that since the plasma equilibrium was assumed to be neutral, $n_{e0} = Zn_{i0}$ where Z is the charge state. Further, the plasma is assumed to be uniform and at rest with no externally applied fields, and the ions are assumed to be immobile given the timescale of the electron oscillations. Thus:

$$\boldsymbol{\nabla} n_0 = n_{i1} = v_0 = E_0 = B_0 = 0 \tag{2.5}$$

$$\frac{\partial n_0}{\partial t} = \frac{\partial v_0}{\partial t} = \frac{\partial E_0}{\partial t} = \frac{\partial B_0}{\partial t} = 0 \tag{2.6}$$

where v, E, and B are the magnitudes of $\mathbf{v}$, $\mathbf{E}$, and $\mathbf{B}$ respectively. Expanding on Equations 2.1-2.3 and keeping only the first order terms gives:

$$m_e n_{e0} \frac{\partial \mathbf{v}_{e1}}{\partial t} = -n_{e0} e \mathbf{E}_1 \tag{2.7}$$

$$\frac{\partial n_{e1}}{\partial t} + n_{e0} \boldsymbol{\nabla} \cdot \mathbf{v}_{e1} = 0 \tag{2.8}$$

$$\boldsymbol{\nabla} \cdot \mathbf{E}_1 = -\frac{e}{\varepsilon_0} n_{e1} \tag{2.9}$$

These equations are solved by assuming simple oscillatory solutions for all perturbed variables, $n_{e1}(\mathbf{x}, t) = n_{e1} e^{i(\mathbf{k}\cdot\mathbf{x} - \omega t)}$ and similar for v_1 and E_1. In this case, $\partial/\partial t \to -i\omega$ and $\boldsymbol{\nabla} \to i\mathbf{k}$ and, by applying these operations to Equation 2.7, $\hat{\mathbf{v}}_{e1} = \hat{\mathbf{E}}_1 = \hat{\mathbf{k}}$ where hat notation indicates unit vectors. Thus the equations are simplified to:

$$i m_e n_{e0} \omega v_{e1} = n_{e0} e E_1 \tag{2.10}$$

$$\omega n_{e1} = n_{e0} k v_{e1} \tag{2.11}$$

$$ikE_1 = -\frac{e}{\varepsilon_0} n_{e1} \tag{2.12}$$

Combining these equations by eliminating the perturbed quantities and assuming that v_{e1} does not vanish yields:

$$m_e \varepsilon_0 \omega^2 = n_{e0} e^2 \tag{2.13}$$

Dropping the 0 subscript and letting $\omega = \omega_p$ for future referencing gives the well-known plasma frequency:

$$\omega_p \equiv \sqrt{\frac{n_e e^2}{m_e \varepsilon_0}} \tag{2.14}$$

This is one of the most fundamental parameters of a plasma and represents the natural oscillations of the electron species about the ion species. Because m_e is quite small, the plasma frequency is usually very high in inertial confinement fusion scenarios. In physical units, $f_p \equiv \omega_p / 2\pi$ may be approximated as:

$$f_p \approx 9000 \sqrt{n_{\mathrm{cc}}}\ \mathrm{Hz} \tag{2.15}$$

where n_{cc} is the electron density in units of cm^{-3}. The majority of this thesis deals with plasmas possessing densities between $10^{19}\,\mathrm{cm}^{-3}$ and $10^{22}\,\mathrm{cm}^{-3}$, putting the plasma frequency on the order of $10^{13}\,\mathrm{Hz}$ to $10^{15}\,\mathrm{Hz}$.

2.2 Debye Shielding

The previous section suggested that fields generated within plasmas are able to be shielded out primarily through electron motion. This was applied to natural charge separations occurring within the plasma itself. However, suppose an externally generated potential was applied inside an infinitely large plasma. Just as in the last section, the electrons quickly move due to the resulting electric field, effectively shielding it out. If the plasma were cold, they would do so perfectly by forming a thin sheath around the potential, allowing no fields to exist within the plasma. However, if the electrons had some finite temperature, $k_B T_e$ where k_B is the Boltzmann constant, those electrons at the edge of the sheath have enough energy to escape the partially shielded potential, thus allowing the field to extend deeper into the plasma. Let the potential, Φ, at the centre of the coordinate system be held at a constant. Poisson's equation gives [46]:

$$\nabla^2\Phi = -\frac{e}{\varepsilon_0}\left(Zn_i - n_e\right) \tag{2.16}$$

Defining the densities at infinity to be $Zn_i = n_e = n_0$, it can be shown that [46]:

$$n_e = n_0 e^{e\Phi/k_B T_e} \tag{2.17}$$

Keeping the ions fixed and combining Equations 2.16 and 2.17 together yields:

$$\nabla^2\Phi = \frac{n_0 e}{\varepsilon_0}\left(e^{e\Phi/k_B T_e} - 1\right) \tag{2.18}$$

In the region where $|e\Phi/k_B T_e|$ is small, Equation 2.18 is then Taylor expanded. Keeping only the linear terms produces:

$$\nabla^2\Phi = \lambda_D^{-2}\Phi \tag{2.19}$$

where the Debye length has been defined as:

$$\lambda_D \equiv \sqrt{\frac{\varepsilon_0}{e^2}\frac{k_B T_e}{n_e}} = \frac{v_{\mathrm{rms}}}{\omega_p} \tag{2.20}$$

where $v_{\mathrm{rms}} = \sqrt{k_B T_e/m_e}$ is the electron root mean square thermal velocity.

Equation 2.19 may then be solved for a point charge by assuming spherical symmetry so that $\nabla^2 = r^{-2}(d/dr)[r^2(d/dr)]$, resulting in:

$$\Phi = \frac{q}{4\pi\epsilon_0 r}e^{-r/\lambda_D} = \Phi_{\mathrm{vac}}e^{-r/\lambda_D} \tag{2.21}$$

where Φ_{vac} is the potential of a point charge in vacuum. The Debye length is therefore another fundamental parameter which indicates the attenuation length of a potential in a plasma, or alternatively, how deep into a plasma the fields from a potential penetrate.

This parameter may be expressed in physical units by:

$$\lambda_D \approx 7.4 \times 10^9 \left(\frac{T_{\mathrm{eV}}}{n_{\mathrm{cc}}}\right)^{1/2} \mathrm{nm} \tag{2.22}$$

where T_{eV} is the electron temperature times the Boltzmann constant in units of eV. For the regions of interest in this thesis, this may range from around 1 nm to 100 nm depending on the plasma density and temperature.

2.3 Electrostatic Waves

2.3.1 Langmuir Waves

Section 2.1 described electron oscillations about fixed ions in cold plasmas which do not propagate. However, when the electron species has some finite temperature, a different dispersion relation is found. In this scenario, the pressure can no longer be neglected and $\boldsymbol{\nabla} P_e = \gamma_e k_B T_e \boldsymbol{\nabla} n_e$ where $\gamma_e = C_p/C_V$ is the ratio of specific heats known as the adiabatic index. Including this term in Equation 2.1 and solving the system of equations in the same manner as performed in Section 2.1, the new dispersion relation is given as [46]:

$$\omega^2 = \omega_p^2 + \gamma_e k^2 v_{\mathrm{rms}}^2 \tag{2.23}$$

This is known as the Bohm-Gross dispersion relation and shows that the oscillations will form waves which propagate through space. These are known as Langmuir waves or plasma waves. In the 1-D case of a planar Langmuir wave, there is only one degree of freedom, and $\gamma_e = 3$. The propagation is possible because now in addition to the restoring electric field, which is responsible for the plasma frequency, there is now an added pressure term which accelerates the high density regions back to their equilibrium locations. This added energy causes the electrons to overshoot the ions by an even greater distance and thus continue propagation forward through the plasma. Note, however, that Langmuir waves are different from electron acoustic waves in that they are primarily driven by Lorentz forces.

2.3.2 Ion Acoustic Waves

Electrons are not the only species which carry waves. Waves also propagate through the ion species, though generally the timescales involved are much larger due to the relatively greater mass. The equations which describe the ion species are similar to those for electrons. In particular, the ion fluid equation and ion equation of continuity are identical to those of electrons. However, because the timescale applicable to ion motions is far longer than that for electrons, instead of using Poisson's equation, one can take the plasma approximation of $n_e = n_i$ due to the effects of Debye shielding. In this case, Equations 2.1, 2.2, and 2.17 are taken for ions rather than electrons, and after assuming $\mathbf{E} = -\boldsymbol{\nabla}\Phi$, $\boldsymbol{\nabla}P_i = \gamma_i k_B T_i \boldsymbol{\nabla} n_i$, and $Z = 1$, the relevant equations are given as [46]:

$$m_i n_i \left[\frac{\partial \mathbf{v}_i}{\partial t} + (\mathbf{v}_i \cdot \boldsymbol{\nabla})\,\mathbf{v}_i\right] = -e n_i \boldsymbol{\nabla}\Phi - \gamma_i k_B T_i \boldsymbol{\nabla} n_i \tag{2.24}$$

$$\frac{\partial n_i}{\partial t} + \boldsymbol{\nabla} \cdot (n_i \mathbf{v}_i) = 0 \tag{2.25}$$

$$n_i = n_e e^{e\Phi/k_B T_e} = n_e \left(1 + \frac{e\Phi}{k_B T_e} + \cdots\right) \tag{2.26}$$

Solving this system of equations in the usual manner and noting that by Equation 2.26, $n_{i1} = n_{i0} \exp\left(e\Phi_1/k_B T_e\right)$, a final dispersion relation is found to be:

$$\frac{\omega}{k} = \left(\frac{k_B T_e + \gamma_i k_B T_i}{m_i}\right)^{1/2} \tag{2.27}$$

This is the dispersion relation for ion acoustic waves which travel at a fixed sound speed. As with a normal sound wave, these have regions of compression and rarefaction. The ions will primarily spread out due to their thermal distribution which is what gives rise to the second term in Equation 2.27. However, there is also rarefaction caused by the ions' positive charges repelling one another. The less perfect the shielding by the electrons, the more this effect will be felt. This accounts for the first term in Equation 2.27, but note that despite this physical picture, there is no dependence on the Debye length. This is due to the plasma assumption originally made of $n_e = Zn_i$. If Poisson's equation were used instead, the full dispersion relation would be given as [46]:

$$\frac{\omega}{k} = \left(\frac{k_B T_e}{m_i}\frac{1}{1 + k^2\lambda_D^2} + \frac{\gamma_i k_B T_i}{m_i}\right)^{1/2} \tag{2.28}$$

As can be seen from this equation, the correction is minor for all ion acoustic waves except for those with wavelengths smaller than the Debye length where single particle interactions are important. If one were to allow $k^2\lambda_D^2 \gg 1$ and assume $T_i \to 0$, the dispersion relation would simply be $\omega^2 = n_0 e^2/\varepsilon_0 m_i \equiv \Omega_p^2$, which is easily recognizable to be the ion equivalent of the plasma frequency. Generally though, $k^2\lambda_D^2 \ll 1$ and $T_e \gg T_i$, which means $\omega \approx c_s k$ where $c_s = (k_B T_e/m_i)^{1/2}$ is defined as the plasma's sound speed.

2.3.3 Magnetic Fields Adjustments

The electrostatic waves presented here have all assumed no magnetic fields. However, the situation changes still further with the introduction of externally applied magnetic fields. For instance, electrostatic electron oscillations perpendicular to a magnetic field will be modified so that $\omega^2 = \omega_p^2 + \omega_c^2 \equiv \omega_h^2$ where $\omega_c = eB/m_e$ is the cyclotron frequency [46]. In this case, the electrons' revolution about the magnetic field acts as an additional restoring force and thus increases the frequency to what is known as the upper hybrid frequency.

2.4 Electromagnetic Waves

Of obvious importance to laser-plasma interactions is the propagation of an electromagnetic wave through a plasma. Initially taking no externally applied fields ($\mathbf{E}_0 = \mathbf{B}_0$), the relevant Maxwell equations are [46]:

$$\boldsymbol{\nabla} \times \mathbf{E}_1 = -\dot{\mathbf{B}}_1 \tag{2.29}$$

$$\boldsymbol{\nabla} \times \mathbf{B}_1 = \mu_0 \left(\mathbf{j}_1 + \varepsilon_0 \dot{\mathbf{E}}_1\right) \tag{2.30}$$

where μ_0 is the vacuum permeability and Newton's dot notation has been used to represent time derivatives. Taking the time derivative of Equation 2.30 while taking the curl of Equation 2.29 and combining yields:

$$\begin{aligned} -\mu_0 \left(\frac{\partial \mathbf{j}_1}{\partial t} + \varepsilon_0 \ddot{\mathbf{E}}_1\right) &= \boldsymbol{\nabla} \times (\boldsymbol{\nabla} \times \mathbf{E}_1) \\ &= \boldsymbol{\nabla}(\boldsymbol{\nabla} \cdot \mathbf{E}_1) - \boldsymbol{\nabla}^2 \mathbf{E}_1 \end{aligned} \tag{2.31}$$

The second step above makes use of a standard vector identity. Taking the regime where the laser frequency is fast enough that the ions can be assumed to be fixed over the length of a cycle, the current will be entirely due to electron motion:

$$\mathbf{j}_1 = -n_{e0} e \mathbf{v}_{e1} \tag{2.32}$$

Now assuming an $\exp[i(\mathbf{k} \cdot \mathbf{x} - \omega t)]$ dependence and noting that to first order:

$$\frac{\partial \mathbf{v}_1}{\partial t} = -\frac{e}{m_e} \mathbf{E}_1 \tag{2.33}$$

Equation 2.31 simplifies to give the well-known dispersion relation for electromagnetic waves:

$$\omega^2 = \omega_p^2 + c^2k^2 \tag{2.34}$$

2.4.1 Consequences of Dispersion Relation

This equation has a very important implication. If a pulse's angular frequency is less than the plasma frequency, k must be imaginary and the pulse will be evanescent. In this case, $k = i(\omega_p^2 - \omega^2)^{1/2}/c$, leading to an exponential attenuation of the pulse with a skin depth, δ, of [46]:

$$\delta = \frac{c}{(\omega_p^2 - \omega^2)^{1/2}} \tag{2.35}$$

Thus, any pulse of given frequency ω_L is not able to effectively propagate into a plasma beyond a density which causes the plasma frequency to equal the laser frequency. This density is known as the critical density and is given when $k = 0$ as:

$$n_c \equiv \frac{m_e \varepsilon_0 \omega_L^2}{e^2} \tag{2.36}$$

When the electron density is below this value, the plasma is said to be underdense. Conversely, an overdense plasma is one which possesses an electron density in excess of this value. In an inhomogeneous plasma with both an underdense and an overdense region, the surface separating the two is called the critical surface.

Another interesting property of plasmas can be seen in the relationship between the group and phase velocities. Defining the index of refraction to be:

$$\eta \equiv c/v_\varphi = ck/\omega \tag{2.37}$$

it can be seen from Equation 2.34 that:

$$v_g = \frac{d\omega}{dk} = c^2/v_\varphi = c\eta \tag{2.38}$$

In other words, within a plasma, the group index (c/v_g) of an electromagnetic pulse is simply the reciprocal of the refractive index.

2.4.2 Magnetic Field Generation

A pulse propagating through a plasma will leave in its wake a persistent DC magnetic field. This is a nonlinear effect which stems from the electron fluid's orbits when the magnetic field is included. This can be seen by following the arguments presented in Gibbon [47]. After a short pulse has completed propagation through a plasma, it will leave a wake formation behind it which takes the form of an approximately sinusoidal density perturbation. This plasma wave will generate a nonlinear current which will form a current loop. This can be seen mathematically by taking the curl of the electron fluid equation and eliminating the electric field using Faraday's law:

$$\boldsymbol{\nabla} \times \frac{\partial \mathbf{p}}{\partial t} + \boldsymbol{\nabla} \times [(\mathbf{v} \cdot \boldsymbol{\nabla})\mathbf{p}] = e\frac{\partial \mathbf{B}}{\partial t} - e\boldsymbol{\nabla} \times (\mathbf{v} \times \mathbf{B}) \tag{2.39}$$

The variables here all pertain to the electron species, so the e subscript has been dropped. This is simplified using vector identities to:

$$\begin{aligned} \frac{\partial \boldsymbol{\Omega}}{\partial t} &= \boldsymbol{\nabla} \times (\mathbf{v} \times \boldsymbol{\Omega}) \\ \boldsymbol{\Omega} &\equiv \frac{1}{m}\boldsymbol{\nabla} \times (\mathbf{p} - e\mathbf{A}) \end{aligned} \tag{2.40}$$

$\boldsymbol{\Omega}$ is the fluid vorticity and $\mathbf{A}$ is the magnetic vector potential, with $\mathbf{B} = \boldsymbol{\nabla} \times \mathbf{A}$. Notice that if $\boldsymbol{\Omega} = 0$ before the pulse begins propagation — that is, the plasma initially has no vorticity — then it will remain zero. In this case:

$$e\mathbf{B} = \boldsymbol{\nabla} \times \mathbf{p} \tag{2.41}$$

Inserting this equation into the electron fluid equation and noting that $\mathbf{v} = \mathbf{p}/\gamma m$ where γ is the Lorentz factor, it can be shown that:

$$e\mathbf{v} \times \mathbf{B} + (\mathbf{v} \cdot \boldsymbol{\nabla})\mathbf{p} = mc^2\boldsymbol{\nabla}\gamma \tag{2.42}$$

which then simplifies to

$$\frac{\partial}{\partial t}(\mathbf{p} - e\mathbf{A}) = \boldsymbol{\nabla}(e\Phi - \gamma mc^2) \tag{2.43}$$

This is a useful restatement of the Lorentz equation and is used in much of the literature for the analysis of relativistic fluid equations [48, 49]. The electron density is then found through Poisson's equation. This is combined with the above equations to give an expanded equation for the fluid momentum:

$$\frac{\partial^2 \mathbf{p}}{\partial t^2} + c^2 \boldsymbol{\nabla} \times (\boldsymbol{\nabla} \times \mathbf{p}) + \frac{\omega_p^2}{\gamma} \mathbf{p} = -mc^2 \boldsymbol{\nabla} \frac{\partial \gamma}{\partial t} - \frac{\mathbf{p}}{\gamma m} \boldsymbol{\nabla} \cdot \left(\frac{\partial \mathbf{p}}{\partial t} + mc^2 \boldsymbol{\nabla} \gamma \right) \tag{2.44}$$

Inserting this into Equation 2.41 yields the magnetic field. The final analysis of this equation is rather complex and not necessary for understanding here, though the important dependence when $a_0 \gg 1$ is $B_0 \propto a_0^2/W^2$ and $\boldsymbol{\nabla} \times \hat{\mathbf{B}} = -\hat{\mathbf{k}}$ where W is the laser spot size in units of c/ω_p and $a_0 = e|\mathbf{A}|/mc$ is the dimensionless vector potential. Thus, more intense, tightly focused pulses will generate the strongest DC magnetic fields pointing in the left-hand azimuthal direction.

This derivation is illustrative of the processes involved in persistent magnetic fields in a plasma, though it focuses on generation in the wake of a pulse. In the case of highly relativistic pulses channeling through a plasma, the effects are even more pronounced as the ponderomotive force will drive the electrons in the channel forward at nearly the speed of light. This results in a current which will approach en_ec in magnitude, thus generating magnetic fields at as distance r from the propagation axis on the order $B = \mu_0 en_e cr/2\pi$ [50]. These strong magnetic fields may reach kilotesla levels and persist long after the pulse has completed propagation ($\sim$100 ps). This is an important phenomenon in channeling as it allows the channel to maintain its structure beyond hydrodynamic predictions due to the $\mathbf{j} \times \mathbf{B}$ force [24].

2.4.3 Faraday Rotation

Just as was the case with electrostatic waves, electromagnetic waves' dispersion relationships will be greatly modified by the presence of a magnetic field. As an example, consider the case where a pulse is traveling along a magnetic field, that is $\mathbf{k} \parallel \mathbf{B}$ Taking $\mathbf{B}_0 = B_0\hat{\mathbf{z}}$, the x and y components of $\mathbf{v}_e$ are given as [46]:

$$\begin{aligned} v_x &= \frac{-ie}{m_e\omega}\left(E_x + v_y B_0\right) \\ v_y &= \frac{-ie}{m_e\omega}\left(E_y + v_x B_0\right) \end{aligned} \tag{2.45}$$

Substituting these values into the current, $\mathbf{j}_1 = -en_e\mathbf{v}$, and solving Equation 2.31 yields:

$$(\omega^2 - c^2k^2)E_x = \frac{\omega_p^2}{1-\omega_c^2/\omega^2}\left(E_x - \frac{i\omega_c}{\omega}E_y\right)$$
$$(\omega^2 - c^2k^2)E_y = \frac{\omega_p^2}{1-\omega_c^2/\omega^2}\left(E_y + \frac{i\omega_c}{\omega}E_x\right) \quad (2.46)$$

Finally, solving these two equations leaves a final set of dispersion relations given by:

$$\eta_R^2 = 1 - \frac{\omega_p^2/\omega^2}{1-(\omega_c/\omega)} \quad (2.47)$$

$$\eta_L^2 = 1 - \frac{\omega_p^2/\omega^2}{1+(\omega_c/\omega)} \quad (2.48)$$

These dispersion relations are for R and L waves respectively which correspond to right-hand and left-hand circular polarisation and have been plotted in Figure 2.1. There are lower cutoffs at $\omega = ((\omega_c^2 + 4\omega_p^2)^{1/2} \pm \omega_c)/2$ which are labeled in the figure ω_R and ω_L. In circular polarisation, the electrons will move in a circular path about the axis of propagation of the pulse (see Section 2.5.1). By including a magnetic field, these electrons will have additional cyclotron motion which will either go against their rotation about this axis, as with L waves, or will enhance it, R waves. Thus right-hand and left-hand circularly polarised pulses will propagate at different velocities with Figure 2.1 clearly showing R waves traveling faster than L waves when $\omega > \omega_R$. As a side note, from these dispersion relations, it is evident that there does exist a region $\omega < \omega_C$ where R waves are able to propagate. This is known as the whistler mode.

The total effect of this difference in phase velocities is a rotation of linearly polarised light. Any linearly polarised pulse can be thought of as a superposition of an R wave and an L wave of equal frequency separated by a phase δ. Setting $\lambda_\alpha = 2\pi c/\omega\eta_\alpha$ where $\alpha = R$ or L, after a distance d of propagation along a constant magnetic field in a uniform plasma, the waves will have undergone $N_\alpha = d/\lambda_\alpha$ cycles, leading to a phase offset for each of $\delta_\alpha = 2\pi \cdot \mathrm{mod}(d, \lambda_\alpha)$. The relative phase $\Delta\delta = \delta_R - \delta_L$ will then have shifted, leading to a net rotation of the linear

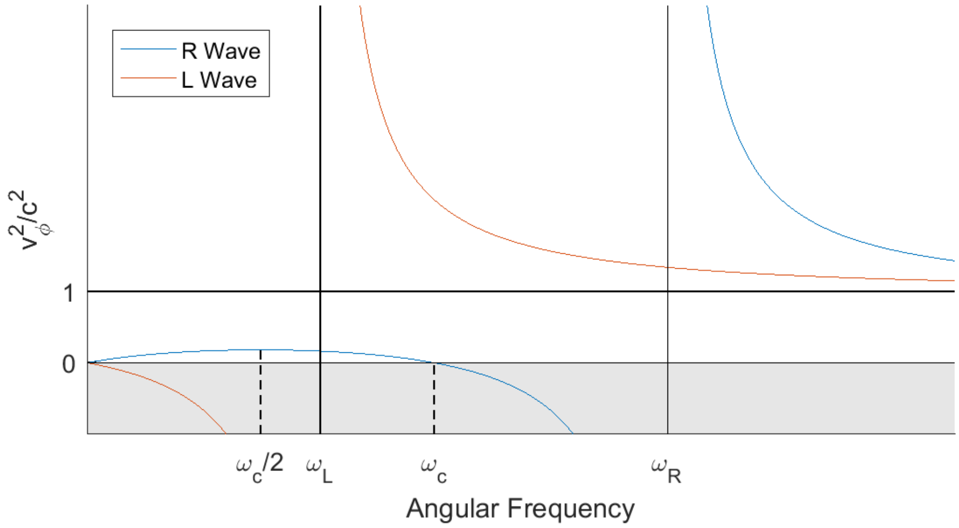

Figure 2.1: Phase velocity of R and L waves. The square of the phase velocities for right-hand and left-hand circular polarised waves along a magnetic field have been plotted against the angular frequency. Only the regions where these values are greater than zero represent physically relevant propagation.

pulse at this point. As will be seen in Chapter 4, this allows for magnetic fields to be measured in experiments.

2.4.4 Cotton-Mouton Effect

The dispersion relation of an electromagnetic pulse will also be altered when propagating perpendicularly to a magnetic field. In this case, rather than being dependent upon right-hand or left-hand polarisation, the dependence now lies upon the plane of the electric field. In the case where the pulse's electric field is parallel to the external magnetic field, the starting equations are the same as for an unmagnetized plasma since the initial velocity perturbation from the electric field will be parallel to the magnetic field. Thus the dispersion relation is unchanged, and the index of refraction is given by [46]:

$$\eta_O^2 = 1 - \frac{\omega_p^2}{\omega^2} \tag{2.49}$$

These types of waves are called O waves, meaning ordinary waves.

If, however, the pulse's electric field is perpendicular to the external magnetic field, a new set of equations must be derived. Taking $\mathbf{B}_0 = B_0\hat{\mathbf{z}}$ again and setting

$\mathbf{E}_1 = E_x\hat{\mathbf{x}} + E_y\hat{\mathbf{y}}$, the initial velocities can be shown through Fourier analysis to be:

$$\begin{aligned} v_x &= -\frac{ie}{m\omega}(E_x + v_y B_0) \\ v_y &= -\frac{ie}{m\omega}(E_y - v_x B_0) \end{aligned} \tag{2.50}$$

As was done in the case of Faraday rotation, substituting these values into the current and solving Equation 2.31 yields:

$$\begin{aligned} \left[\omega^2\left(1-\frac{\omega_c^2}{\omega^2}\right)-\omega_p^2\right]E_x + i\frac{\omega_p^2\omega_c}{\omega}E_y = 0 \\ \left[(\omega^2-c^2k^2)\left(1-\frac{\omega_c^2}{\omega^2}\right)-\omega_p^2\right]E_y - i\frac{\omega_p^2\omega_c}{\omega}E_x = 0 \end{aligned} \tag{2.51}$$

This set of equations is then solved in order to find the final dispersion relation of:

$$\eta_X^2 = 1 - \frac{\omega_p^2}{\omega^2}\frac{\omega^2-\omega_p^2}{\omega^2-\omega_h^2} \tag{2.52}$$

This is the dispersion relation for X waves, otherwise known as extraordinary waves. Now the initial perturbation to the electrons' velocities is perpendicular to $\mathbf{B}_0$, and as a result, their orbits will be altered. This acts as an additional restoring force. As was done for Faraday rotation, the phase velocities for X and O waves have been plotted in Figure 2.2. Interestingly, the left cutoffs for the X wave match those found for the L and R waves. At $\omega > \omega_R$, the X wave clearly travels faster than the O wave.

The net effect of this difference in phase velocities is now a change in the ellipticity of a pulse. Any pulse can be thought of as a superposition between two linear pulses, one an X wave and the other an O wave, with a relative phase difference of $\Delta\delta$. If $\Delta\delta = 0$ or π, the pulse will be linear, whereas if $\Delta\delta = \pi/2$ or $3\pi/2$, it will be circular. Because of the birefringent properties of a magnetized plasma, the relative phase between the X and O waves will change in the exact same manner as occurred for R and L waves. It is this change in $\Delta\delta = \delta_X - \delta_O$ which defines the change in ellipticity. This phenomenon is known as the Cotton-Mouton effect.

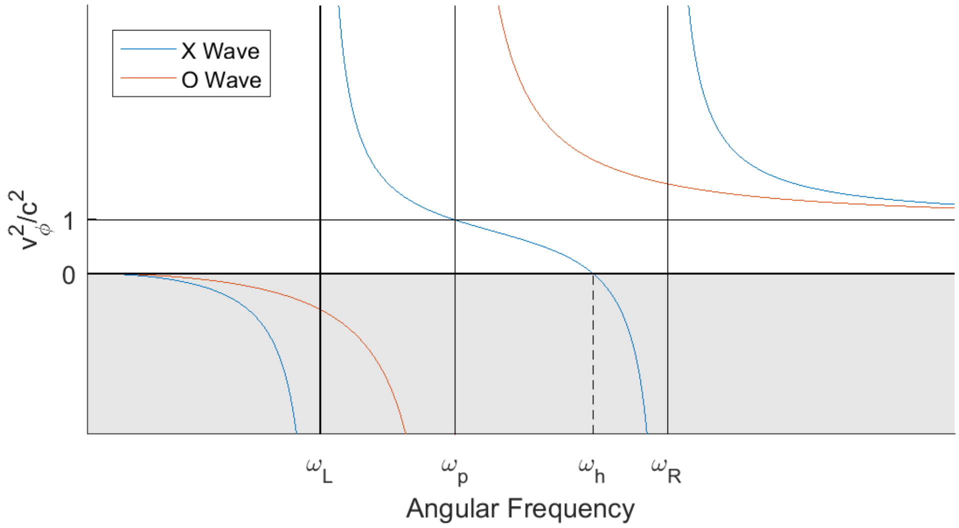

Figure 2.2: Phase velocity of X and O waves. The square of the phase velocities for X and O waves have been plotted against the angular frequency. Only the regions where these values are greater than zero represent physically relevant propagation.

2.4.5 Parametric Instabilities

When a laser pulse is propagating through a plasma, it has a chance to decay into multiple waves. This nonlinear wave-wave interaction is common in plasmas and is known as a parametric instability. Parametric instabilities give rise to various phenomena in laser-plasma interactions such as the filamentation instability, discussed in Section 2.7.4, and affect the overall propagation of a laser pulse. It is therefore important to understand the mechanisms which cause these instabilities in order to analyse the work presented in the remainder of this thesis.

These instabilities occur when a pump wave, often an electromagnetic wave, drives two other waves. Each of these waves will beat with the pump wave, and it is because of these beat patterns that the generated waves are able to grow and amplify one another. Parametric instabilities may therefore be treated as coupled oscillators. Further, the energy for the these waves comes from the pump, but if the pump is strong enough, it will be relatively unaffected by the generated waves. In this case, the coupled oscillator behaviour may be treated with linear theory as will be done below [46].

Assuming small damping or growth rates and small frequency shifts, it can be shown through coupled harmonic oscillator equations that, in order to conserve momentum and energy, the total frequency and wavenumber must be matched [46]. For instance, a pulse (ω_0, k_0) will decay within a plasma to form a forward-traveling ion acoustic wave (ω_1, k_1) and a reflected electromagnetic wave (ω_2, k_2). Then $\omega_0 = \omega_1 + \omega_2$ and $k_0 = k_1 + k_2$ with each of the waves following their dispersion relations given in previous sections. This type of parametric instability is known as Brillouin backscattering. Any wave in a plasma will decay into multiple other waves as long as these conditions are met.

Figure 2.3 shows parallelogram constructions for various three-wave parametric instabilities. In order, these are (a) stimulated Brillouin scattering, (b) parametric decay, (c) two-plasmon decay, and (d) electron decay instabilities. The narrow hyperbola in each image is the basic electromagnetic dispersion relation, the wide hyperbola the plasma wave relation, and the straight lines the ion acoustic wave relation as given by Equations 2.34, 2.23, and 2.27 respectively. By plotting each wave as a vector from the origin to a position on its dispersion relation and constructing a parallelogram, both wave matching criteria and the dispersion relations are satisfied.

Analysis of these diagrams reveals much about the requirements for certain instabilities. For instance, consider the two-plasmon decay instability shown in Figure 2.3(c). Here, an electromagnetic wave decomposes into two plasma waves, one forward and one backward traveling. Frequency matching requires that the two plasma waves' frequencies must add to the original electromagnetic wave's frequency. These waves must exist with $\omega_{\text{Langmuir}} \geq \omega_p$ each, so the electromagnetic wave's frequency must be at least $\omega \geq 2\omega_p$. This puts a limit on the density of the plasma for this instability to occur because $\omega^2 \geq (2\omega_p)^2$ implies $n_e \leq n_c/4$. A pulse is not able to decay into two Langmuir waves above quarter critical densities because the two plasma waves would have more energy than the original pulse. A similar argument holds for stimulated Raman scattering, where an electromagnetic wave decays into a plasma wave and another electromagnetic wave.

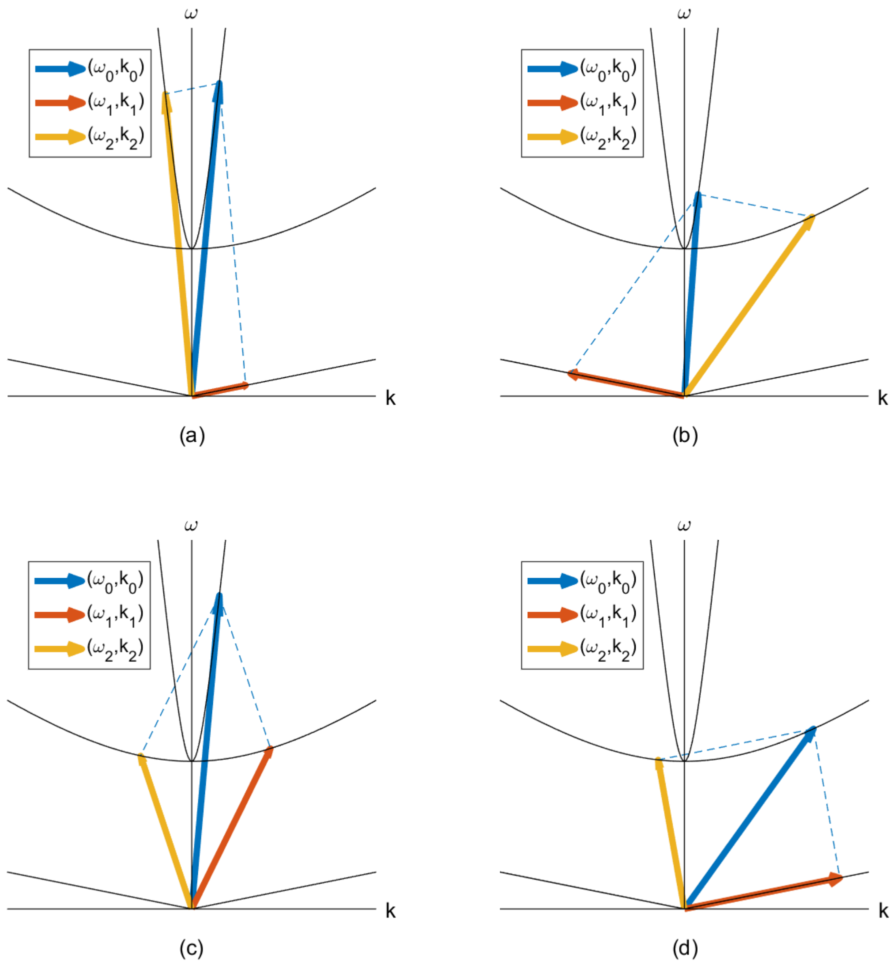

Figure 2.3: Parametric instabilities. The dispersion relations for electromagnetic (narrow hyperbola), Langmuir (wide hyperbola), and ion acoustic (straight lines) waves are shown in black in these phasespace diagrams. The original wave (blue) decays into two waves (yellow and red) through frequency and wavenumber matching. The instabilities shown are (a) stimulated Brillouin backscattering instability, (b) parametric decay instability, (c) two-plasmon decay instability, and (d) electron decay instability.

In principle, these instabilities can occur at any intensity. However, when damping occurs in the plasma, for example, through collisions or a phenomenon known as Landau damping, the growth of the instabilities is limited and an intensity threshold is created. This is seen by adding a damping term, $2\Gamma(dx/dt)$, to each of the coupled harmonic oscillator equations which derived the frequency and wavenumber matching equations:

$$\begin{aligned} \frac{d^2x_1}{dt^2} + \omega_1^2 x_1 + 2\Gamma_1 \frac{dx_1}{dt} &= c_1 x_2 E_0 \\ \frac{d^2x_2}{dt^2} + \omega_2^2 x_2 + 2\Gamma_2 \frac{dx_2}{dt} &= c_2 x_1 E_0 \end{aligned} \tag{2.53}$$

By taking $\omega \approx \omega_1$ and $\omega_0 - \omega \approx \omega_2$, as they are non-resonant (neither approximation is exact), these equations can be Fourier analysed assuming $x_1 \to x_1 \cos(\omega t)$, $x_2 \to x_2 \cos[(\omega - \omega_0)t]$, and $E_0 \to E_0 \cos(\omega_0 t)$ and simplified to:

$$(\omega^2 - \omega_1^2 + 2i\omega\Gamma_1)[(\omega_0 - \omega)^2 - \omega_2^2 - 2i(\omega_0 - \omega)\Gamma_2] = \frac{1}{4} c_1 c_2 E_0^2 \tag{2.54}$$

The lowest intensity threshold occurs at perfect resonance when the previously made approximations become exact. Therefore, when $\omega = \omega_1$ and $\omega_0 - \omega = \omega_2$:

$$I_{\text{thresh}} = 8c\varepsilon_0 \frac{\omega_1 \Gamma_1}{c_1} \frac{\omega_2 \Gamma_2}{c_2} \tag{2.55}$$

Thus if either wave is undamped, there is no intensity threshold.

Each of these instabilities has a certain growth rate which is found by allowing ω in Equation 2.54 to be complex. To illustrate this, consider stimulated Brillouin scattering. The density modulation n_1 which forms the ion wave is represented by x_1 and the reflected wave's electric field E_2 is represented by x_2. In this case, the coupling variables are given as [46]:

$$\begin{aligned} c_1 &= \varepsilon_0 k_1^2 \omega_p^2 / \omega_0 \omega_2 m_i \\ c_2 &= \omega_p^2 \omega_2 / n_0 \omega_0 \end{aligned} \tag{2.56}$$

Now assume that the intensity of the initial wave is far above the intensity threshold so that damping terms are safely neglected and let $\omega = \omega_s + i\Theta$. Assuming $\Theta^2 \ll \omega_s^2$ and $n \ll n_c$, Equation 2.54 becomes at resonance:

$$(2i\omega_s\Theta)(-2i\omega_2\Theta) = 4\omega_s\omega_2\Theta^2 = \frac{1}{4} k_1^2 \Omega_p^2 v_{\text{osc}}^2 \tag{2.57}$$

where $v_{\mathrm{osc}} \equiv eE_0/m_e\omega_0$ is the maximum quiver velocity of an electron in an electromagnetic wave neglecting relativistic corrections.

Now due to the far greater slope of the electromagnetic wave dispersion relation compared to the ion acoustic wave dispersion relation, it can be approximated that $\omega_2 \approx \omega_0$ and $k_1 \approx 2k_0 = 2\omega_0^2/c^2$. This can be easily seen from Figure 2.3(a). Substituting these values and solving for Θ then gives the final equation for the growth rate of the Brillouin scattering instability:

$$\Theta = \frac{v_{\mathrm{osc}}}{2c}\left(\frac{\omega_0}{\omega_s}\right)^{1/2}\Omega_p \tag{2.58}$$

The same methodology is applied to derive the growth rates for other parametric instabilities as well.

2.4.6 Absorption

Parametric instabilities are one way for an electromagnetic wave to transfer its energy to the plasma. However, there are many other mechanisms which lead to pulse depletion. For instance, consider a laser pulse propagating through an inhomogeneous plasma incident upon the critical surface at an oblique angle. The electric field of the pulse has a component along the density gradient into the plasma oscillating at $\omega = \omega_p$. Thus it is able to resonantly drive a Langmuir wave through the plasma, resulting in what is known as resonant absorption.

Note that the resonance breaks down when the oscillation of the electrons in the electric field exceeds the scale length of the plasma. Resonant absorption is therefore not effective at sharp density surfaces. Instead, another form of collisionless absorption is observed known as Brunel heating [51], otherwise known as not-so-resonant resonant absorption or simply vacuum heating [52]. In this scenario, a pulse is obliquely incident upon a sharp boundary between vacuum and a highly overdense plasma. The electrons at the edge of the plasma are drawn out into the vacuum region during one half-cycle of the electric field and get rapidly accelerated back into the plasma during the second half-cycle. Because the plasma is highly overdense, the skin depth is extremely small, and as a result, the electron will continue to propagate into the plasma.

A similar effect occurs when $a_0 > 1$ and the pulse is nearly normal to the boundary surface. In this case, the $\mathbf{v} \times \mathbf{B}$ part of the Lorentz force is non-negligible and will cause surface electrons to be sent into the plasma at velocities increasing with a_0. This is shown in greater detail in Section 2.5. These electrons are then lost to the laser field in the same manner as for Brunel heating. This process is called relativistic $\mathbf{j} \times \mathbf{B}$ heating.

There are several other mechanisms that lead to absorption using collisions as well, such as inverse bremsstrahlung which is discussed in Section 2.6.2, and the skin effect, wherein the pulse becomes evanescent after reaching the critical surface and oscillates the electrons within its skin depth. These electrons then collide with other particles, causing diffusion of the energy away from the pulse and into the plasma [46].

2.5 Single Electron Interactions

While working from the basic equations of motion, Equations 2.1-2.3, is useful to describe a wide variety of waves and instabilities within a plasma, the interaction of an extremely intense pulse with particles and plasmas requires a more robust treatment [47]. Including relativistic effects, the Lorentz force and conservation of energy for an electron in an electromagnetic field are given by:

$$\frac{d\mathbf{p}}{dt} = \frac{d}{dt}(\gamma m_e \mathbf{v}) = -e(\mathbf{E} + \mathbf{v} \times \mathbf{B}) \tag{2.59}$$

$$\frac{d}{dt}(\gamma m_e c^2) = -e(\mathbf{v} \cdot \mathbf{E}) \tag{2.60}$$

where $\mathbf{p}$ is momentum and $\gamma = (1 - v^2/c^2)^{1/2}$ is the Lorentz factor. Now define an elliptically polarised pulse traveling in the $\hat{x}$ direction to be:

$$\mathbf{A} = (0, \delta A_0 \cos\varphi, (1 - \delta^2)^{1/2} A_0 \sin\varphi) \tag{2.61}$$

where $\varphi = \omega t - kx$ and δ is a measure of ellipticity ($\delta = 0$, ± 1 for linear, $\pm 1/\sqrt{2}$ for circular polarisations). To simplify this problem, these equations are then normalized using $t \to \omega t$, $x \to kx$, $\mathbf{v} \to \mathbf{v}/c$, $\mathbf{p} \to \mathbf{p}/mc$, and $\mathbf{a} \to e\mathbf{A}/mc$. Using the defined vector potential with Equation 2.61 and integrating the transverse component of Equation 2.59 yields:

$$\mathbf{p}_\perp - \mathbf{a} = \mathbf{p}_{\perp 0} \tag{2.62}$$

Here $\mathbf{p}_{\perp 0}$ is a constant derived from the integration step. Similarly, subtracting the longitudinal components of Equations 2.59 and 2.60 and integrating yields:

$$\gamma - p_x = \alpha \tag{2.63}$$

where α is some constant of motion. In deriving this equation, it was noted that since $\mathbf{a}$ is dependent solely upon the variable $(x - t)$, $\partial_x \mathbf{a} = -\partial_t \mathbf{a}$ where the shorthand $\partial_\beta = \partial/\partial\beta$ has been used.

To find a way to relate $\mathbf{p}_\perp$ to p_x, the Lorentz factor can be rewritten as $\gamma = (1 + p^2)^{1/2}$, or in other words, $\gamma^2 = 1 + p_x^2 + p_\perp^2$. Using this equation with Equation 2.63 to eliminate p_x gives the equation to determine the constant of motion:

$$p_x = \frac{1 - \alpha^2 + p_\perp^2}{2\alpha} \tag{2.64}$$

Finally, it should be observed that:

$$\frac{d\varphi}{dt} = \frac{\partial\varphi}{\partial t} + \frac{p_x}{\gamma}\frac{\partial\varphi}{\partial x} = 1 - \frac{p_x}{\gamma} = \frac{\alpha}{\gamma} \tag{2.65}$$

which implies:

$$\mathbf{p} = \gamma\frac{d\mathbf{r}}{dt} = \gamma\frac{d\varphi}{dt}\frac{d\mathbf{r}}{d\varphi} = \alpha\frac{d\mathbf{r}}{d\varphi} \tag{2.66}$$

In the following section, this equation will be useful in finding the path of a particle in an intense field.

2.5.1 Laboratory Frame

Taking an electron initially at rest in the laboratory frame means that $p_x(t = 0) = p_\perp(t = 0) = 0$. Then by Equation 2.64, $\alpha = 1$. Solving for the momenta gives [47]:

$$\begin{aligned} p_x &= \frac{a_0^2}{4}\left[1 + \left(2\delta^2 - 1\right)\cos 2\varphi\right] \\ p_y &= \delta a_0 \cos\varphi \\ p_z &= \left(1 - \delta^2\right)^{1/2} a_0 \sin\varphi \end{aligned} \tag{2.67}$$

Now integrating by making use of Equation 2.66 gives the orbits for a particle in the lab frame:

$$
\begin{aligned}
x &= \frac{a_0^2}{4}\left(\varphi + \frac{2\delta^2 - 1}{2}\sin 2\varphi\right) \\
y &= \delta a_0 \sin\varphi \\
z &= -(1-\delta^2)^{1/2} a_0 \cos\varphi
\end{aligned}
\tag{2.68}
$$

where $a_0 = eA_0/mc$. These orbits are plotted in Figure 2.4 for the linear pulse defined by $\delta = 1$ both on the ordinary axes, $kx - ky$, and the self-similar axes, $kx/a_0^2 - ky/a_0$. As can be seen in this figure, as the value of a_0 increases, the electrons are displaced further from the axis and have a much greater longitudinal step. This is due to the increased field strengths which will be able to accelerate the electrons further away. Further, the electron's longitudinal position is monotonically increasing with φ. As the electron is accelerated in one direction by the electric field, the magnetic field will adjust its trajectory to the forwards direction. Upon switching signs, the electric field then slows the particle down and eventually reverses its direction. However, the magnetic field also will have flipped signs, and as a result, when the electron has reversed direction, the magnetic field will still cause its path to point forward as it was before. Thus the electron continues on monotonically for the duration of the plane wave.

2.5.2 Centre of Oscillation Frame

Notice that there is always motion in the same direction in x. Taking the cycle average, $\langle\cdot\rangle$, of the momentum gives a constant drift velocity of [47]:

$$\frac{v_D}{c} = \langle v_x \rangle = \frac{a_0^2}{4 + a_0^2} \tag{2.69}$$

It is then desirable to observe the orbits of the particles in the frame moving along with the particle at velocity v_D. Taking the cycle average of Equation 2.64 and taking $\mathbf{p}_\perp = \mathbf{a}$ gives:

$$\alpha = \left(1 + \langle a^2 \rangle\right)^{1/2} = \left(1 + \frac{a_0^2}{2}\right)^{1/2} \equiv \gamma_0 \tag{2.70}$$

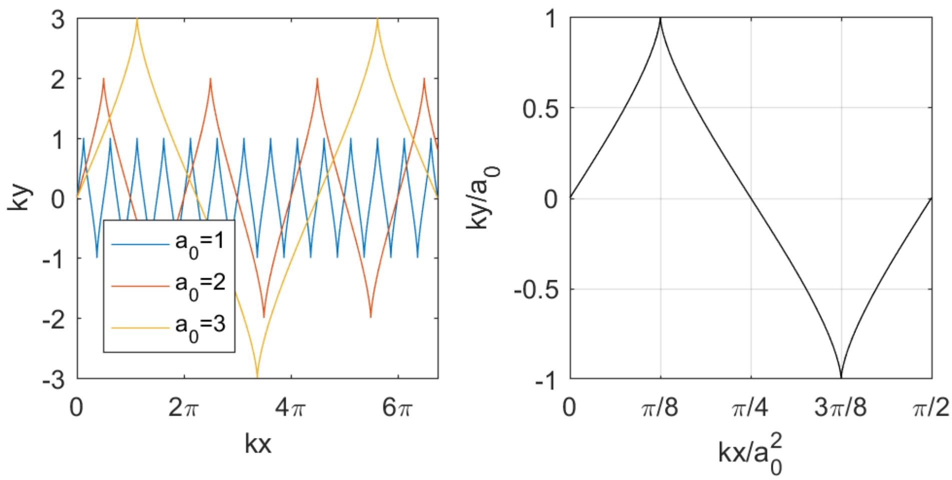

Figure 2.4: Single particle orbits in a linear electromagnetic field in the laboratory frame. On the left, the orbits are plotted against kx and ky to show how varying the value of a_0 alters the path the particle takes. On the right, these axes have been normalized as indicated to show the self-similar orbit.

The momenta are then given by:

$$\begin{aligned} p_x &= \left(2\delta^2 - 1\right) \frac{a_0^2}{4\gamma_0} \cos 2\varphi \\ p_y &= \delta a_0 \cos\varphi \\ p_z &= \left(1 - \delta^2\right)^{1/2} a_0 \sin\varphi \end{aligned} \tag{2.71}$$

Integrating as before to find the orbits yields:

$$\begin{aligned} x &= \left(\delta^2 - \frac{1}{2}\right) \frac{a^2}{4\gamma_0^2} \sin 2\varphi \\ y &= \delta \frac{a_0}{\gamma_0} \sin\varphi \\ z &= -\left(1 - \delta^2\right)^{1/2} \frac{a_0}{\gamma_0} \cos\varphi \end{aligned} \tag{2.72}$$

The results of these orbits in the co-moving frame to the centre of oscillation are shown in Figure 2.5. As can be seen, in this frame, the particles follow a figure eight motion about a centre drift. This figure eight widens as the value of a_0 increases, but not infinitely so. As $a_0 \to \infty$, $\gamma_0 \to a_0/\sqrt{2}$, thus limiting the size of the figure eight to $kx_{\max} = 1/4$ and $ky_{\max} = \sqrt{2}$ as can be seen from Equations 2.72 and Figure 2.5.

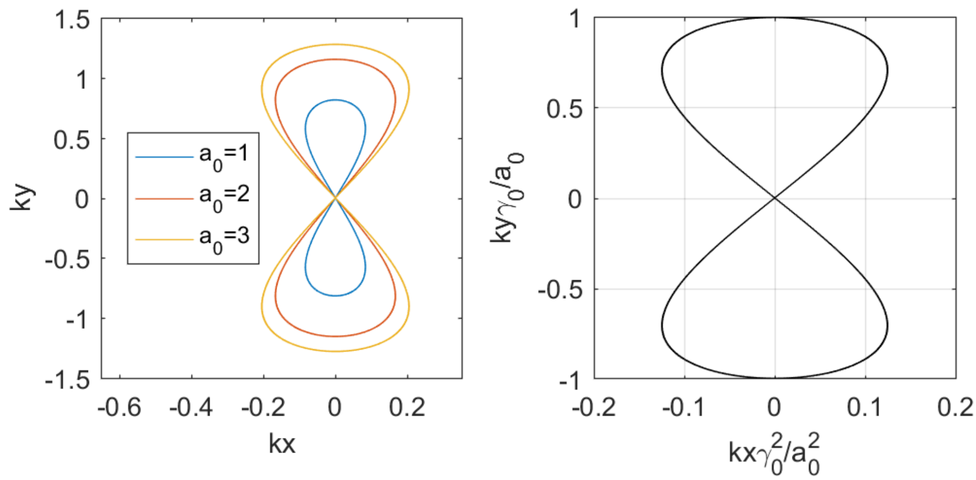

Figure 2.5: Single particle orbits in a linear electromagnetic field in the centre of oscillation frame. On the left, the orbits are plotted against kx and ky to show how varying the value of a_0 alters the path the particle takes. On the right, these axes have been normalized as indicated to show the self-similar orbit.

2.5.3 Relativistic Effects

Notice that if the particles are initially cold, that is $\mathbf{p}_{\perp 0} = 0$, then Equation 2.62 shows that the dimensionless transverse momentum is just $\mathbf{p}_\perp = \mathbf{a}$. As a result, when $a_0 = 1$, the electrons' kinetic energies will be on the order of their rest energies. At this point, the pulse is said to be of relativistic intensity. To determine what physical units this corresponds to, note that $a_0 = e|\mathbf{E}|/m_e\omega c$. From this, it can be shown that:

$$\begin{aligned} a_0^2 &= I\lambda^2 \frac{e^2}{2\pi^2\varepsilon_0 m_e^2 c^5} \\ &= \frac{I\lambda_\mu^2}{1.37 \times 10^{18}\,\mathrm{W\,cm^{-2}}} \end{aligned} \tag{2.73}$$

where λ_μ is the wavelength given in micrometers. Therefore, a 1 µm wavelength pulse is said to be relativistic when its intensity is on the order of $1.37 \times 10^{18}\,\mathrm{W\,cm^{-2}}$.

The relativistic motion causes a mass increase for each electron so that the cycle-averaged Lorentz factor is given as $\gamma = (1 + \langle a^2 \rangle)^{1/2}$. This equation depends on the polarisation of the pulse, but for the most common cases of linear and circular polarisation [47]:

$$\gamma = \begin{cases} \sqrt{1 + a_0^2/2} & \text{Linear Polarisation} \\ \sqrt{1 + a_0^2} & \text{Circular Polarisation} \end{cases} \tag{2.74}$$

Several effects arise due to this relativistic mass increase. First, consider the physical processes involved in determining the critical density. When the plasma frequency matches the pulse frequency, the electrons are able to naturally shield out the electromagnetic pulse and the wave becomes evanescent. However, the forced oscillation in a relativistically intense pulse causes the electrons' mass to increase, thereby adjusting the plasma frequency to $\omega_{\gamma p}^2 = n_e e^2/(\gamma m_e)\varepsilon_0 = \omega_p^2/\gamma$. Thus the critical density is increased by a factor of γ, $n_{\gamma c} = \gamma n_c$. This effect is known as relativistically induced transparency.

Not only does relativistically induced transparency allow a relativistic pulse to propagate to higher densities, but it has a profound influence on the shape of a finite-width pulse as well. Taking intensity into account, the phase velocity is given by $v_\phi/c = (1 - n_e/\gamma n_c)^{-1/2}$. γ is dependent upon the intensity of the pulse at any given point, so even in a homogeneous plasma, the sides of a relativistic pulse where the intensity is weaker will have a greater phase velocity than the high intensity centre. This causes the pulse to focus inward in a process known as relativistic self-focusing.

2.5.4 Ponderomotive Force

The previous subsections have assumed a plane wave, infinite in extent. However, considerations must be made for the case of a finite pulse. In this case, particles experience a force exerted by an inhomogeneous wave which causes a net displacement away from the higher intensity regions. This is because the particle is accelerated from the high intensity region towards the low intensity region during its first half-cycle of oscillation. However, during the second half-cycle when a homogeneous field would have returned it to its original position, the intensity of the field is weaker, and as a result, the particle is not accelerated back towards the high intensity region as strongly, thereby experiencing a cycle-averaged drift. This nonlinear effect is known as the ponderomotive force. Typically it is most easily derived using

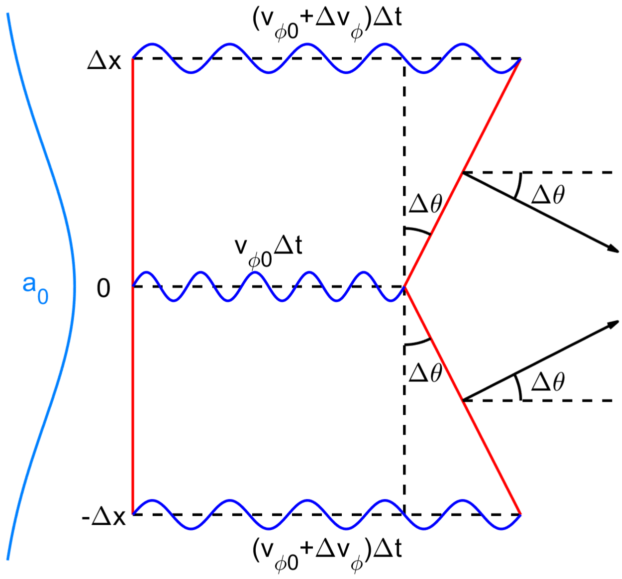

Figure 2.6: Relativistic self-focusing. The intensity profile is indicated by the a_0 curve. After propagating for a time, Δt, the phase front of a pulse is distorted to cause self-focusing as indicated by the red lines. This is the result of the high intensity causing a shift in the critical density, thereby causing a phase velocity gradient to form.

perturbative Fourier analysis as was done in Sections 2.1-2.4. However, should the fields reach relativistic intensities - that is, intensities high enough to cause the particles to reach relativistic velocities - simple harmonic motion is no longer guaranteed. Thus, a more robust approach must be used. In this case, a Lagrangian method [53] will be used, though covariant analyses [54] are equally appropriate.

The relativistically correct form of the Lagrangian for a particle of charge q and mass m in an arbitrary electromagnetic field is given by:

$$L(\mathbf{x}, \mathbf{v}, t) = -\frac{mc^2}{\gamma} + q\mathbf{v}\cdot\mathbf{A} - q\Phi. \tag{2.75}$$

where Φ is again the electric scalar potential and γ the Lorentz factor.

Assuming there exists a centre of oscillation and taking the action-angle variables, $S(\mathbf{x}, t)$ and $\varphi(\mathbf{x}, t)$ where S is the action and φ is the angle ($\varphi = \mathbf{k}\cdot\mathbf{x} - \omega t$ in the case of a monochromatic traveling wave), Hamilton's principle gives:

$$\delta S = \delta \int_{\varphi_1}^{\varphi_2} L \frac{dt}{d\varphi} d\varphi \tag{2.76}$$

Because both S and φ are Lorentz invariant, $\mathcal{L}(\varphi) \equiv L(\mathbf{x}_0(\varphi), \mathbf{v}_0(\varphi), t(\varphi))/(\partial_t \varphi)$ will be as well. Assuming φ is normalized to 2π, the cycle-averaged Lagrangian is given by:

$$\mathcal{L}_0 = \frac{1}{2\pi} \int_{\varphi}^{\varphi+2\pi} \mathcal{L}(\varphi') d\varphi' \tag{2.77}$$

which now depends only on the centre of oscillation coordinates $\mathbf{x}_0(\varphi)$, $\mathbf{v}_0(\varphi)$, $t(\varphi)$, thereby allowing analysis of the cycle net effects only. It is important to cycle-average over the invariant phase instead of time as the particles are permitted to approach relativistic velocities.

The oscillation centre of motion is then determined by the Lagrange equations of motion:

$$\frac{d}{dt}\left(\frac{\partial L_0}{\partial \mathbf{v}_0}\right) - \frac{\partial L_0}{\partial \mathbf{x}_0} = 0 \tag{2.78}$$

where the Lagrangian has been transformed back from its invariant form, $L_0 = \mathcal{L}_0 \partial_t \varphi$.

The Hamiltonian of a point charge in an electric field is $H = \mathbf{p}\cdot\mathbf{v} - L$. Introducing the effective mass $m_{\text{eff}} = L_0 \gamma_0 / c^2$, in any inertial frame where the centre of oscillation moves at $\mathbf{v}_0$, the Lagrangian and Hamiltonian are simplified to:

$$\begin{aligned} L_0 &= -\frac{m_{\text{eff}} c^2}{\gamma_0} \\ H_0 &= \gamma_0 m_{\text{eff}} c^2 \\ \gamma_0 &= \left(1 - \frac{v_0^2}{c^2}\right)^{-1/2} \\ \mathbf{p}_0 &= \gamma_0 m_{\text{eff}} \mathbf{v}_0 \end{aligned} \tag{2.79}$$

In the co-moving frame where at a time t, $\mathbf{v_0}(t) = 0$, the ponderomotive force can be found through the combination of Equations 2.78 and 2.79:

$$\mathbf{f}_p^N = \frac{d\mathbf{p}_0}{d\tau} = \frac{\partial L_0}{\partial \mathbf{x}_0} = -c^2 \boldsymbol{\nabla} m_{\text{eff}} = -mc^2 \boldsymbol{\nabla} \gamma \tag{2.80}$$

where the N superscript indicates that it is a Newtonian force, and τ is then the proper time.

As shown in Equation 2.74, given an electromagnetic wave, the Lorentz factor for an electron oscillating in the wave's fields is $\gamma = (1+a_0^2/\alpha)^{1/2}$ where $\alpha = 1$ for circular and $\alpha = 2$ for linear polarisation. It is worth observing that in the limit of $a_0 \ll 1$, by substituting $a_0 = eE/mc\omega$ and taking the linear polarisation case, Equation 2.80 can be expanded to the more familiar non-relativistic ponderomotive force:

$$\begin{aligned} \mathbf{f}_p^N \approx -mc^2\boldsymbol{\nabla}\left(1+\frac{a_0^2}{4}\right) &= -mc^2\boldsymbol{\nabla}\frac{e^2E^2}{4m^2c^2\omega^2} \\ &= -\frac{1}{4}\frac{e^2}{m\omega^2}\boldsymbol{\nabla}E^2 \end{aligned} \tag{2.81}$$

2.5.5 DC Fields

One final point of exploration worth considering is the motion of a charged particle in the presence of persisting fields [46]. As will be seen later in this thesis, hole-boring and channeling form long-lasting azimuthal magnetic fields along the sides of the channels which allow the channel to persist for a relatively long duration. Thus it is important to understand how individual particles interact with these fields. Since this section is meant only to describe the basic phenomena, a simple Fourier analysis is acceptable.

Consider a particle with charge q and mass m in a magnetic field, $\mathbf{B}$, experiencing an external force, $\mathbf{F}$. This force could for instance be caused by an electric field, $\mathbf{F} = q\mathbf{E}$. Then:

$$m\frac{d}{dt}\mathbf{v} = \mathbf{F} + q\mathbf{v}\times\mathbf{B} \tag{2.82}$$

Taking $\mathbf{B} = B\hat{\mathbf{z}}$, the z component will not be affected by the magnetic term, and thus the particle will respond to the applied force along the magnetic field as if the field were not present. Now choose $\hat{\mathbf{x}}$ so that $\mathbf{F} = F_x\hat{\mathbf{x}} + F_z\hat{\mathbf{z}}$. Then it can be shown that:

$$\frac{d^2}{dt^2}\left(v_y + \frac{F_x}{qB}\right) = -\omega_c^2\left(v_y + \frac{F_x}{qB}\right) \tag{2.83}$$

where $\omega_c = qB/m$ is the cyclotron frequency. Note that if the substitution $v_f = v_y + F_x/qB$ is made, this represents simple harmonic motion. Thus the particle has some drift perpendicular to the magnetic field around which it oscillates at the cyclotron frequency.

To find the generalized version of this drift, the $md\mathbf{v}/dt$ term can be ignored since this just generates the cyclotron motion. Dropping this term from Equation 2.82 and taking the cross product with $\mathbf{B}$ gives:

$$\mathbf{F} \times \mathbf{B} = q\mathbf{B} \times (\mathbf{v} \times \mathbf{B}) = qB^2\mathbf{v} - (\mathbf{v} \cdot \mathbf{B})\mathbf{B} \tag{2.84}$$

Thus the component transverse to the magnetic field is given as:

$$\mathbf{v}_f = \frac{\mathbf{F} \times \mathbf{B}}{qB^2} \tag{2.85}$$

As can be seen from this equation, when a magnetic field is present, the overall drift of a particle actually travels perpendicularly to the externally applied force due to cyclotron motion. The greater the magnetic field, the higher the cyclotron frequency and the smaller the Larmor radius, $r_L = v_\perp/\omega_c$. Thus for intense magnetic fields, particles will have tighter orbits about their centre drift paths, often misleadingly known as the lines of force. This property is important especially in magnetic confinement fusion and has been used in the past as a method to confine a plasma using magnetic mirrors.

2.6 Plasma Formation

2.6.1 Coulomb Collisions

As will be discussed in the following subsection, much of the ionization that occurs from a laser pulse incident on a solid at intensities below $10^{15}\,\mathrm{W\,cm^{-2}}$ is caused by Coulomb collisions. Thus it is important to understand the nature of these interactions. Since a plasma consists of multiple species of charged particles, collisions result from deflections caused by the Coulomb interaction, which explains the origin of the term "Coulomb collisions".

The collisions between electrons and ions within a plasma will transfer momentum from one species to the other. The rate of change of momentum from the electrons to the ions is denoted by $\mathbf{P}_{ei}$ and from the ions to the electrons as $\mathbf{P}_{ie}$. In order to conserve momentum, the total transferred from one species to the other must be equal, so $\mathbf{P}_{ie} = -\mathbf{P}_{ei}$. This momentum transfer is written in the usual manner as [46]:

$$\mathbf{P}_{ei} = m_e n(\mathbf{v}_i - \mathbf{v}_e)\nu_{ei} \tag{2.86}$$

and similar for $\mathbf{P}_{ie}$. Here, ν_{ei} is the electron-ion collision frequency.

With the goal of determining ν_{ei}, consider a test particle of mass m_t and charge q_t approaching a fixed particle of charge q_f at speed v_0 and let b be the distance of closest approach in the particle's path neglecting the Coulomb force, otherwise known as the impact parameter. Then in circular coordinates with the fixed charge at the origin and using Newton's notation, the test particle will experience radial and angular forces given respectively by:

$$\begin{aligned} m_t(\ddot{r} - r\dot{\theta}^2) &= \frac{q_t q_f}{4\pi\varepsilon_0 r^2} \\ m_t(r\ddot{\theta} + 2\dot{r}\dot{\theta}) &= 0 \end{aligned} \tag{2.87}$$

These equations result from the radial nature of the Coulomb force. Combining these equations to find the energy of the system then yields:

$$\frac{1}{2}m_t(\dot{r}^2 + r^2\dot{\theta}^2) + V(r) = \frac{1}{2}m_t v_0^2 \tag{2.88}$$

where $V(r)$ is the potential energy. $\dot{\theta}$ can be eliminated by conservation of angular momentum, and thus, solving for θ and substituting $s = b/r$ and $A = q_t q_f / 2\pi\varepsilon_0 m_t v_0^2 b$, it can be shown that:

$$\begin{aligned} \theta &= \int_0^{b/r} \left(1 - s^2 - As\right)^{-1/2} ds \\ &= \tan^{-1}\left[\frac{A}{2} + \frac{b}{r}\left(1 - A\frac{b}{r} - \frac{b^2}{r^2}\right)\right] \end{aligned} \tag{2.89}$$

The point where the force is most strongly felt will be where $dr/d\theta = 0$. At this point, the test particle will have been deflected by $\chi/2$ where χ is the total asymptotic deflection angle. Equation 2.89 then is solved at this point to find:

$$\tan\left(\frac{\chi}{2}\right) = \frac{q_t q_f}{4\pi\varepsilon_0 m_t v_0^2 b} \tag{2.90}$$

For low-angle collisions, $\tan(\chi/2) \approx \chi/2$. Now consider the case of an electron and an ion. Because of its mass, the ion will be treated as the fixed particle with the electron acting as the test particle. The number of collisions the electron undergoes in a time, t, between the impact parameter range of b to $b + db$ is $N_{\text{collide}} = n_i(v_0 t)(2\pi b db)$ which can be thought of as the density of collision points times the volume of a hollow cylinder of thickness db, radius b, and length $v_0 t$. Thus, the total deflection angle is found by adding up all of the small angle collisions over the impact parameter. This amounts to an integration of $N_{\text{collide}}\chi^2$ over b. However, due to divergence of the integral, this must be performed from some minimum to some maximum angle:

$$\sum \chi^2 \approx \int_{b_{\min}}^{b_{\max}} 2\pi n_i v_0 t \chi^2(v_0, b) b db = \frac{Z^2 e^4}{2\pi\varepsilon_0^2} \frac{n_i t}{m_e^2 v_0^3} \ln \Lambda \tag{2.91}$$

where $\ln \Lambda \equiv \ln(b_{\max}/b_{\min})$ is known as the Coulomb logarithm. The choices of v_0, $b_{\min}$ and $b_{\max}$ vary. Typically $b_{\max} = \lambda_D$ since beyond the Debye length, the ion will be mostly shielded by the electrons, resulting in no collisions beyond this point. One choice for $b_{\min}$ is the impact parameter which results in 90° scattering, or $b_{\min} = e^2/4\pi\varepsilon_0 m_e v_0^2$. Finally, assuming a Maxwellian distribution in the electron species, v_0 is chosen to be $v_{\text{rms}} = \sqrt{k_b T_e/m_e}$. Thus [55]:

$$\sum \chi^2 \approx \frac{Z^2 e^4}{2\pi\varepsilon_0^2} \frac{n_i t}{m_e^{1/2}(k_b T_e)^{3/2}} \ln \Lambda \tag{2.92}$$

Finally, to find the collision frequency, one must determine the cross section, $\sigma = \pi b^2$, using the impact parameter which causes the electrons to deflect 90°. This impact parameter can be approximated by solving Equation 2.90 for $\chi = 90°$. Then $\nu_{ei} = n_i v_0 \sigma$. Note, however, that most large-angle deflections of a particle in a plasma are actually due to a series of small-angle deflections, and simply solving Equation 2.90 for $\chi = 90°$ neglects these effects. A more accurate derivation involves finding the change in velocity of the test particle as a function of time, averaging it over the impact parameter, and finding the time it takes for the change in the root-mean-square velocity to equal the velocity itself. This allows several small-angle collisions to be included as well [47]. However, the results of the two methods are identical in form except for a factor of $\ln \Lambda$. This important factor can alter the collision frequency by an order of magnitude. Using $v_0 = v_{\mathrm{rms}}$, the collision frequency is given by:

$$\nu_{ei} = \frac{n_e Z e^4}{16\pi\varepsilon_0^2 m_e^{1/2}(k_B T_e)^{3/2}} \ln\Lambda \tag{2.93}$$

Notice that $\nu_{ei} \propto n_e Z (k_B T_e)^{-3/2}$. This implies that as a plasma gets more dense, it becomes more collisional, which makes sense given the physical picture. However, as the plasma heats up, the electrons will have greater average velocities. As a result, they will spend less time interacting with the ions during their orbits, thus lowering the total deflection. At higher temperatures, the collisional frequency becomes negligible, and thus the plasma can be treated as collisionless. The mean free path of a charged particle is given as approximately $\lambda_{ei} = v_{\mathrm{rms}}/\nu_{ei}$. This is given more simply as [46]:

$$\lambda_{ei} \approx 3.4 \times 10^{17} \frac{T_{\mathrm{eV}}^2}{n_{\mathrm{cc}} \ln\Lambda} \mathrm{\mu m} \tag{2.94}$$

For a hydrogen plasma with $n = 10^{21}\,\mathrm{cm}^{-3}$, $T = 1\,\mathrm{keV}$, and $\ln\Lambda = 10$, the mean free path is $\lambda_{ei} \approx 34\,\mathrm{\mu m}$. Thus, when the interaction region is of this scale, collisions are negligible, and the plasma must be treated kinetically rather than hydrodynamically. As will be discussed in Chapter 3, this is important in deciding which type of simulation code is best suited to investigate the physics of interest.

2.6.2 Ionization

Now that the process of collisions has been described, it is possible to review the ionization of a solid to create a plasma [47]. Several processes lead to the ionization of a target. However, the dominant mechanism for ionization when the intensity of a laser pulse is under approximately $10^{15}\,\mathrm{W\,cm^{-2}}$ is collisional absorption, otherwise known as inverse bremsstrahlung absorption. While the laser pulse is incident upon neutral atoms, its electric field will cause the free electrons to accelerate. As these free electrons oscillate, they will collide with the ions, effectively transferring the energy from the laser pulse to the particles. This leads to heating of the target, and eventually the bound electrons will be released. Additionally, these newly freed electrons will then be able to oscillate with the laser field and transfer energy to the neutral atoms as well, leading to avalanche ionization.

At high intensities or with greater frequencies, different forms of ionization take place. The electric field of a high-intensity pulse acts to lower the barrier energy trapping the bound electrons. This is depicted in Figure 2.7. As can be seen from this image, one side of the potential will have been lowered so that energies below the typical ionization level will be able to escape via quantum tunneling, thus leading to tunnel ionization. The longer this potential structure is maintained, the more likely the electrons are to escape in this method. Thus, tunnel ionization is more likely to occur at high intensities when the frequency of the pulse is low. A special case exists where the barrier is suppressed to below the electron's energy state. In this case, no tunneling is required and the electron will spontaneously escape, a process known as barrier suppression ionization.

This is contrasted with multiphoton ionization wherein multiple photons are simultaneously absorbed by a bound electron to escape the potential well. Here, when the frequency is high, fewer photons are required to ionize the atoms, thereby increasing the likelihood of occurrence. Because of this, multiphoton ionization is more likely to occur at high intensities when the frequency of the pulse is high.

To determine whether multiphoton or tunnel ionization will occur, Keldysh proposed in 1965 to use what is now known as the Keldysh parameter [56]:

$$\gamma_K = \frac{\omega}{eE}\sqrt{2m_e V_I} \tag{2.95}$$

where E is the electric field amplitude and V_I is the zero-field ionization energy. Clearly then, $\gamma_K \gg 1$ indicates that multiphoton ionization is expected to dominate while $\gamma_K \ll 1$ indicates a preference for tunnel ionization.

2.6.3 Hydrodynamic Expansion

Once the target has been ionized, it is able to expand outwards, driven by the plasma pressure. Assuming a large spatial extent of the plasma, this can be treated as a

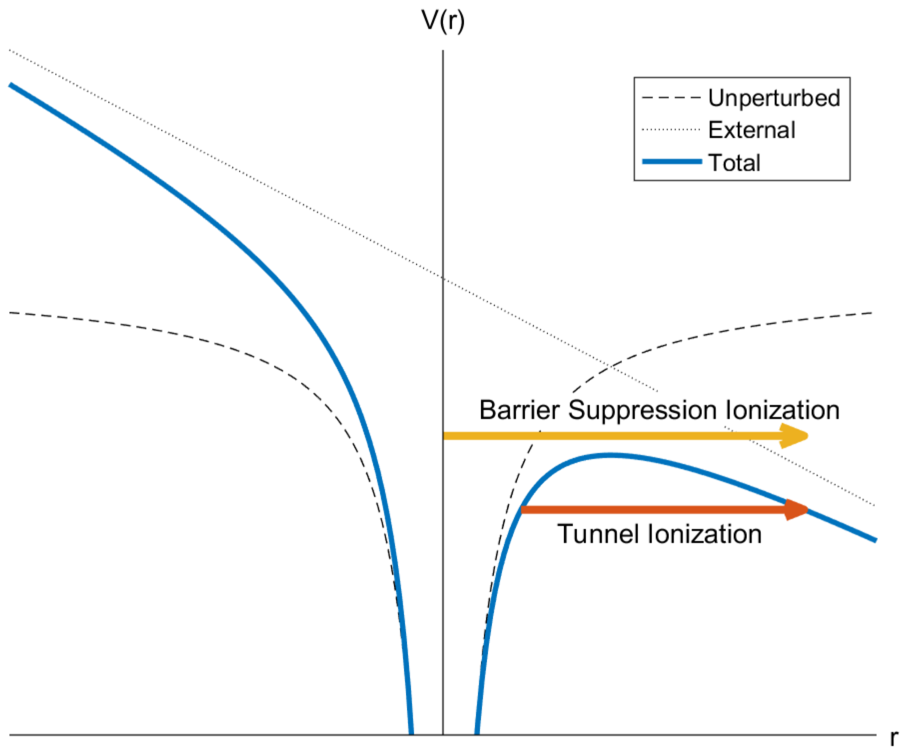

Figure 2.7: Tunnel and barrier suppression ionization. The altered potential is shown in blue. The red arrow indicates an example energy where an electron would be able to escape the potential via quantum tunneling while the yellow arrow indicates an example energy which would allow an electron to spontaneously escape.

1D expansion. It can be shown that by neglecting electron inertia and combining the electron and ion fluid equations, one is left with [57]:

$$\begin{aligned} \frac{\partial n_i}{\partial t} + \frac{\partial}{\partial z}(n_i v_i) &= 0 \\ \frac{\partial v_i}{\partial t} + v_i \frac{\partial v_i}{\partial z} &= -c_s^2 \frac{1}{n_i} \frac{\partial n_i}{\partial z} \end{aligned} \tag{2.96}$$

n and v are both dependent upon z and t. However, it can be guessed that there exists functions f and g such that $n(z,t) = f(\xi)$ and $v(z,t) = g(\xi)$ where $\xi = z/t$. Then, letting $f' = \partial_\xi f$ and similarly for g', Equation 2.96 is rewritten as:

$$\begin{aligned} f'(g - \xi) + f g' &= 0 \\ g'(g - \xi) + c_s^2 \frac{f'}{f} &= 0 \end{aligned} \tag{2.97}$$

Solving these equations for f and g and rewriting everything in terms of the original variables gives the final set of equations for describing the 1D hydrodynamic growth of the system [57]:

$$\begin{aligned} n &= n_0 e^{-\frac{z}{c_s t}} \\ v &= c_s + \frac{z}{t} \end{aligned} \tag{2.98}$$

Thus the expected density profile of an ablated plasma is an exponential with scale length $c_s t$. Notice that c_s is dependent upon the electron temperature, so higher intensities which heat up the plasma to greater levels will generally cause greater scale lengths to form.

2.7 Laser-Plasma Channeling

The primary focus of this thesis is channeling in plasmas similar to those found in inertial confinement fusion. The aim of this process is to create a persistent low-density channel in the plasma using a laser pulse as discussed in more detail in Chapter 3. When the pulse propagates through an underdense plasma, this process is known as channeling, whereas if it is incident upon an overdense plasma, it is called hole-boring. While these two processes are similar in their goals, different physics are involved in each scenario. The following subsections are primarily focused on channeling due to its increased complexity, with a brief summary of hole-boring at the end.

2.7.1 Channel Profiles

Initially, take a linearly polarised pulse of frequency ω and constant intensity passing through an underdense plasma of density n and consider the timescale, τ, such that [60]:

$$\Omega_p^{-1} \gg \tau \gg \omega_p^{-1} \tag{2.99}$$

where Ω_p is the ion plasma frequency as defined in Section 2.3.2. Because $\tau \gg \omega_p^{-1}$, the electrons will have time to relativistically oscillate and the bulk motions are observed. Further, $\Omega_p^{-1} \gg \tau$ implies that ion dynamics can be neglected. Therefore, the physical picture for the channeling process within this timescale can be described as follows. The laser pulse enters an underdense plasma and ponderomotively expels the electron species out of its path as described in Section 2.5.4. This evacuation of the electrons creates a charge separation which in turn sets up strong electric fields, thus limiting the expulsion of the electrons and forming a standing profile which will be derived in the remainder of this subsection. Beyond this timescale, the electrons will remain balanced between the ponderomotive force and the charge separation fields long enough so that the ions then have time to expand outwards in a Coulomb explosion [58, 59], resulting in a low-density channel through the plasma. To see this, one must balance the ponderomotive force with the restoring fields by looking at the components perpendicular to the channel, given as:

$$e\boldsymbol{\nabla}_\perp \Phi = mc^2 \boldsymbol{\nabla}_\perp \gamma + \frac{1}{n_e}\boldsymbol{\nabla}_\perp (n_e k_B T_e) \tag{2.100}$$

where $\gamma = (1 + a^2/2)^{1/2}$ is the Lorentz factor given to the electrons through quiver motion in a linear pulse and the plasma pressure has been included on the right-hand side of the momentum equation. Further, the ion motion can be defined by the momentum and continuity equations for the ion species, given respectively by:

$$\begin{aligned} \frac{d}{dt}\mathbf{v}_i &= -\frac{Ze}{m_i}\boldsymbol{\nabla}_\perp \Phi \\ \frac{\partial n_i}{\partial t} + \boldsymbol{\nabla}_\perp (n_i \mathbf{v}_i) &\approx \frac{\partial n_i}{\partial t} + n_{i0}\boldsymbol{\nabla}_\perp \mathbf{v}_i = 0 \end{aligned} \tag{2.101}$$

Note that the ponderomotive effects have been neglected in the momentum equation due to the much greater mass of ions causing them to generally not be affected on the timescales examined here for realistic intensities. It has also been assumed that $T_i \ll T_e$.

Now to make some further simplifying assumptions, assume that the perturbations to the ion density are very small, $n_{i1}/n_{i0} \ll 1$ where $n_i = n_{i0} + n_{i1}$, and $a^2 \ll 1$. This means that the channels described here are not accurate for moderate densities or relativistically intense pulses as are primarily utilized in this thesis, and because of this, the derivation presented here is meant only to be illustrative of the physical picture. The analysis required for more accurate modeling is far more complex and not directly necessary for the remainder of this work and has

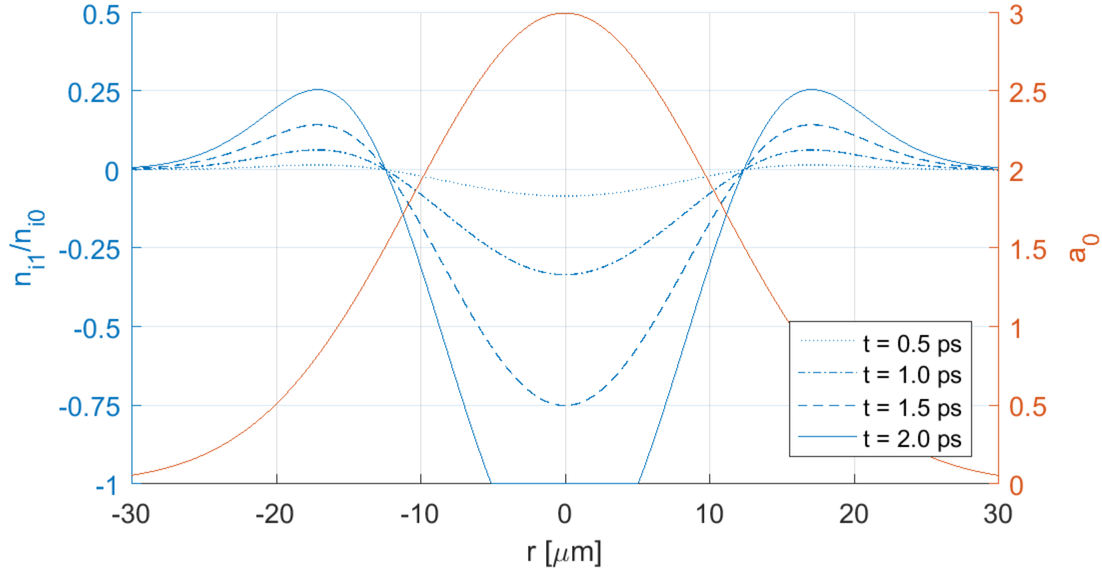

Figure 2.8: Evolution of a channel. The numerical integration of Equation 2.102 is shown at various times in blue and overlayed with the pulse's dimensionless vector potential. The channel is considered empty when $n_{i1} < -n_{i0}$.

been omitted for the sake of simplicity. The reader is directed to the derivations which allow for multifilament structures and charge conservation presented in 2D by Cattani, *et al.* in 2001 [48] and in 3D by Kim, *et al.* in 2002 [49].

Combining Equations 2.100 and 2.101 with these assumptions and simplifying gives [60]:

$$\left(\frac{\partial^2}{\partial t^2} - c_s^2 \boldsymbol{\nabla}_\perp^2\right) \frac{n_{i1}}{n_{i0}} \approx \frac{Zm_e}{m_i} c^2 \boldsymbol{\nabla}_\perp^2 \left(1 + \frac{a^2}{2}\right)^{1/2} \tag{2.102}$$

where $c_s = (Zk_BT_e/m_i)^{1/2}$ is the sound speed. This equation is simply an inhomogeneous wave equation and can be integrated to give the final density profile. For example, consider a pulse with profile $a = a_0 \exp(-r^2/W^2)$ where $a_0 = 3$ and $W = 15\,\mu\text{m}$ in a plasma where $m_i = 4590 m_e$, $Z = 1$, and $T_e = 1\,\text{keV}$. Figure 2.8 shows the results of numerically integrating Equation 2.102 at various times in the case of 3D cylindrical geometry where $\boldsymbol{\nabla}_\perp^2 = r^{-1}\partial_r(r\partial_r)$. As the plasma is ejected from the channel, a surrounding high-density sheath forms. The structure of this sheath varies greatly depending upon the intensity of the pulse and the plasma parameters. Note that after 2 ps, the unphysical result of $n_{i1} < -n_{i0}$ appears, meaning the total density would be negative. One approach to managing this is to simply set $n_i = 0$ in regions where it would have otherwise been negative. However, this does not address charge conservation and must be treated as an approximation only.

2.7.2 P-Plane: Surface Waves

While the last section looked strictly at bulk perturbations which occur on timescales much greater than ω^{-1}, there are several other phenomena which occur on smaller timescales which lead to large, observable effects. Take again a pulse propagating through a plasma, and consider the p-plane, that is, the plane which contains the pulse's electric field. In this plane, the electric field of the pulse will couple to the high-density electron sheath that will have formed around the channel. At the head of the pulse, this force will cause the electrons to cluster against the field. When the electric field switches direction, so too does the force on the electrons, and they will cluster on the opposite channel wall. Because these clusterings are density increases, the phase velocity will be increased on the clustered side, resulting in refraction of the pulse away from the high density. The back-and-forth nature of this behavior results in surface waves forming on the walls of the channel [61].

To see this analytically, consider the frame co-moving with the pulse, $x_g = x - v_g t$ where the pulse has been chosen to propagate in x. The electric field in this frame will oscillate at a frequency:

$$\omega_0 = \omega(1 - v_g/v_\phi) = \omega(1 - \eta^2) = \omega_p^2/\omega \tag{2.103}$$

This will cause the pulse to hose back and forth and will excite antisymmmetric surface waves. The dispersion relation for this mode has been shown to be approximately [61]:

$$\omega_{\mathrm{sw}} = \frac{ck_{\mathrm{sw}}}{\sqrt{1 + \delta/W}} \tag{2.104}$$

where W is the channel width and $\delta = c/\omega_p$ is the skin depth.

The surface waves can alternatively be looked at as excitations resulting from the radiation of the strong oscillating currents at the sharp front of the laser pulse [61, 62]. The Doppler-shifted frequency of emitted surface waves from this oscillating source is given by:

$$\omega_{\text{sw}} = \frac{\omega_0}{1 - v_g/v_{\phi,\text{sw}}} \tag{2.105}$$

where $v_{\phi,\text{sw}} = \omega_{\text{sw}}/k_{\text{sw}}$ is the phase velocity of the surface wave. This equation is rewritten as:

$$\omega_{\text{sw}} - k_{\text{sw}} v_g = \omega_0 = \frac{\omega_p^2}{\omega} \tag{2.106}$$

Then assuming $\delta \ll W$ and taking $\lambda_{\text{sw}} = 2\pi/k_{\text{sw}}$ to be the wavelength of the surface waves:

$$\lambda_{\text{sw}} \approx \lambda \frac{n_c}{n_e}\left(1 - \frac{v_g}{c}\right) \tag{2.107}$$

where λ is the wavelength of the laser pulse.

In the limit of $v_g \ll c$, this equation has experimentally and numerically been shown to accurately predict the wavelength of surface waves [63].

2.7.3 S-Plane: Solitons

Another feature of underdense channeling is the formation of low-density bubbles surrounding the channeling pulse in the plane perpendicular to the electric field of the pulse, the s-plane. These bubbles form as light from the channel escapes and propagates through the plasma. The escaped light will be downshifted until the plasma it is propagating through appears overdense. At this point, the electromagnetic energy is trapped and ponderomotively expels the electrons. Before the ions have time to move, this structure is known as an electromagnetic soliton. Given enough time, the ions follow the electrons and a post-soliton forms. Traditionally in mathematics and physics, a soliton is any wave packet which travels at a constant velocity without distorting its shape. Bulanov *et al.* first predicted and numerically observed electromagnetic solitons in 1992 [62], noting that they possessed a near-fixed shape and drift velocity, thus imparting the name to this phenomenon.

The analysis of the actual formation of the solitons is not of importance to this thesis, though much work exists in the literature [62–69]. However, it is important to determine how electromagnetic energy can escape a channel. Take a simplified model [68] where the channel has density n_{in}, the walls of the channel have density n_{w}, and the rest of the plasma has density n_{out}, all of which are normalized to n_c. If α is the angle between the channel wall and the incoming light within the channel and θ is the angle between the channel wall and the escaped light through the background plasma, then Snell's law states:

$$\cos\theta = \cos\alpha\sqrt{\frac{1-n_{\mathrm{in}}}{1-n_{\mathrm{out}}}} \tag{2.108}$$

The angle α can be determined by taking the ratio of the perpendicular and longitudinal k values:

$$\tan\alpha = \frac{k_\perp}{k_\parallel} \tag{2.109}$$

The perpendicular wavenumber must be some multiple of π/W where W is the channel width, and the total wavenumber must satisfy $\omega = ck$ for the pulse assuming $n_{\mathrm{in}} \ll 1$. That is:

$$\begin{aligned} k_\perp &= \frac{m\pi}{W} \\ k_\parallel &= \sqrt{\frac{\omega^2}{c^2} - k_\perp^2} \end{aligned} \tag{2.110}$$

where m is a non-zero integer.

The critical angle for total internal reflection is again given by Snell's law as:

$$\sin\alpha_c = \sqrt{\frac{1-n_{\mathrm{w}}}{1-n_{\mathrm{in}}}} \tag{2.111}$$

This puts a minimum on the leakage mode number, m, so that:

$$m > \frac{2W}{\lambda}\sqrt{\frac{n_{\mathrm{w}}-n_{\mathrm{in}}}{1-n_{\mathrm{in}}}} \tag{2.112}$$

This equation fixes the angles at which light will escape from a channel and shows that it is more difficult for light to leak when n_{w} increases, the channel widens, or n_{in} increases (assuming $n_{\mathrm{w}} > 1$). Note that the light is only able to escape in the s-plane due to resonant absorption limiting the amount of escaped light in the p-plane.

2.7.4 Filamentation Instability

One of the most destructive instabilities involved in the channeling process is the filamentation instability. This causes the pulse to divide into several narrow channels instead of staying as one unified channel. Combined with the hosing instability, which is described in detail in Chapter 3, each of these beamlets will then be redirected, causing the pulse to break up and eliminating any channeling efficiency.

While there are several causes of filamentation, they all ultimately result from a density perturbation forming in the plasma which then causes part of the pulse to refract away from its peaks [70]. If this perturbation is in the centre of the pulse, it will lead to splitting. These perturbations may be initially present in the plasma, though this is not required. In a homogeneous, collisionless plasma with a high intensity pulse, the primary mechanism is the ponderomotive force. If the pulse is not perfect and has several speckles, where the intensity profile is extremely modulated due to interference patterns within the beam, the ponderomotive force will not push the plasma completely out of its path, but will instead force it towards the bottom of its intensity wells, forming density perturbations in the centre of the pulse. This is known as ponderomotive filamentation. However, at lower intensities in a collisional plasma, filamentation will occur due to thermal effects. If the mean free path of an electron is less than the filament width, inverse bremsstrahlung heating will lead to a hydrodynamic expansion. This expels the plasma from the high-intensity regions and leads to self-focusing within this filament width in what is called thermal filamentation.

Bingham, *et al.* in 1984 described filamentation as a four wave process wherein an initial electromagnetic wave $(\omega_0, \mathbf{k}_0)$ interacts with a density perturbation $(\Omega, \mathbf{k})$ at one position resulting in an altered electromagnetic wave $(\omega_1, \mathbf{k}_0 - \mathbf{k})$. Similarly, another position will interact with a density perturbation pointing in the opposite direction resulting in $(\omega_2, \mathbf{k}_0 + \mathbf{k})$. The net effect is a focusing of the pulse between these perturbations. If the pulse is wide enough so that this focusing will occur at multiple locations in its transverse plane, it will break apart into multiple beamlets as a result of this focusing. This is shown schematically in Figure 2.9.

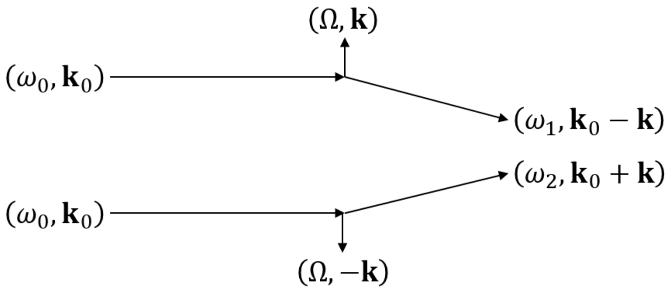

Figure 2.9: Diagram of wave vectors for filamentation. An electromagnetic pulse will couple to the density perturbations in the plasma, leading to strong focusing in these regions. If this occurs in more than one location of the pulse, it will filament into smaller beamlets.

Though the derivation is too long to include here, the basic approach is similar to that used in Section 2.4.5. By using wave matching and perturbative analysis, it can be shown that the growth rate for filamentation is given as [70]:

$$\Gamma_{\text{fil}} = \frac{e^2\omega_p^2}{8n_e^2\omega_0^2\omega_1 v_{\text{th}}^2}\left(1 + \frac{1}{7.6k_\perp^2\lambda_{\text{mfp}}}\right) \tag{2.113}$$

where $\lambda_{\text{mfp}} = v_{\text{th}}/\nu_{ei}$ is the mean-free-path length of the electron species. The first term in the parenthesis corresponds to ponderomotive filamentation while the second term comes from thermal filamentation. Thus the ratio between the two, $\gamma_f = 300\lambda_{\text{mfp}}^2/\lambda_\perp^2$ where λ_f is the filament width, defines whether thermal ($\gamma_f < 1$) or ponderomotive ($\gamma_f > 1$) filamentation is dominant.

2.7.5 Hole-Boring

Up until this point, the physical picture has been a pulse propagating through an underdense plasma, expelling electrons which in turn pull the ions along with them. However, for completeness, this subsection focuses instead on hole-boring, when a pulse is incident upon an overdense plasma. In this case, the low-density channel is not formed directly through ponderomotive forces, but rather through a transfer of momentum from the photons to the ions.

First, it is important to determine the pressure exerted by photons. The intensity of a pulse at any point is the amount of energy passing through an area per unit time, or in other words, its energy flux. Assuming a monochromatic beam, each photon carries energy $\hbar\omega$ and momentum $\hbar k$. Then to find the momentum flux of a pulse, one must simply take the energy flux and multiply it by $\hbar k/\hbar\omega = c^{-1}$. Thus the momentum flux is given by I/c. A change in the momentum flux will result in pressure upon the reflecting surface.

Now it is possible to construct a simple model to describe the hole-boring process [71]. Consider a pulse incident from the left upon a cold overdense plasma which is boring at velocity v_{hb}. Assume $v_{\mathrm{hb}} \ll c$ and take the frame co-moving with the hole-boring front. In this simple model, both the ions and photons will be assumed to be perfectly reflected with every reflected ion/photon having the same energy as their approach. The momentum flux to the left of the front then is just made up of the approaching pulse, I/c and its reflected momentum, $-I/c$. On the right side of the front, the ions are approaching the front at v_{hb} so that their momentum flux is given by $-n_i m_i v_{\mathrm{hb}}^2$, and their reflected counterparts have a momentum flux of $n_i m_i v_{\mathrm{hb}}^2$. By conservation of momentum:

$$\frac{I}{c} - n_i m_i v_{\mathrm{hb}}^2 = -\frac{I}{c} + n_i m_i v_{\mathrm{hb}}^2 \tag{2.114}$$

Solving for v_{hb} gives:

$$\frac{v_{\mathrm{hb}}}{c} = \sqrt{\frac{I}{m_i n_i c^3}} \equiv \Xi_{\mathrm{hb}} \tag{2.115}$$

Since v_{hb} in this case is non-relativistic, the ions will simply be reflected in the lab frame at $2v_{\mathrm{hb}}$.

This can be extended to allow for relativistic hole-boring velocities which occurs when $I \sim n_i m_i c^3$ by noting that in the moving frame, the intensity of the light will differ from the lab frame, I_0 due to a Doppler shift by

$$\frac{I}{I_0} = \frac{1 - v_{\mathrm{hb}}/c}{1 + v_{\mathrm{hb}}/c} \tag{2.116}$$

Using this fact, the correct hole-boring velocity is then shown to be [72]:

$$\frac{v_{\mathrm{hb},\gamma}}{c} = \frac{\Xi_{\mathrm{hb}}}{1 + \Xi_{\mathrm{hb}}} \tag{2.117}$$

and the reflected ion energy, $\mathcal{E}_i$, in the lab frame is given as:

$$\frac{\mathcal{E}_{i,\gamma}}{m_i c^2} = \frac{2\Xi_{\mathrm{hb}}^2}{1 + 2\Xi_{\mathrm{hb}}} \tag{2.118}$$

Note that while these relativistic equations were originally derived and tested against simulations assuming circular polarisation [72], the derivation consists exclusively of momentum conservation and relativistic Doppler shifts. Neither of these phenomena are dependent upon polarisation, and thus, these results apply independently of polarisation as well.

2.7.6 Channel Depths

As discussed in Section 2.7.5, the hole-boring velocity is found by balancing the momentum flux of reflected ions and photons in the channel front's frame. In order to find the hole-boring depth, d_{hb}, of a pulse of fixed intensity and duration in the limit where n_e is comparable to n_c, all that remains is to integrate the hole-boring velocity over the duration of the pulse's propagation. In the simplest case of constant density and a flat-top pulse – that is, one which begins and ends instantaneously while maintaining a constant intensity in between – all that is required is to multiply the over-dense hole-boring velocity by the duration of the pulse, τ, to obtain:

$$d_{\mathrm{hb}} = \Xi_{\mathrm{hb}} c\tau = a_0 c\tau \left(\frac{n_c}{2n_e} \frac{Z m_e}{m_i} \right)^{1/2} \tag{2.119}$$

It is worth observing that the derivation of Eq. 2.119 assumes that the hole-boring velocity is non-relativistic (i.e. $I \ll \rho c^3$). To allow for relativistic hole-boring speeds, the number density and mass in the plasma momentum flux must each be multiplied by a Lorentz factor, and the intensity of the pulse will undergo a Doppler shift between the laboratory and channel front frames. As discussed in Section 2.7.5, these combined effects result in a lowered hole-boring velocity of $v_{\mathrm{hb}}/c = \Xi_{\mathrm{hb}}/(1 + \Xi_{\mathrm{hb}})$. Additionally, due to the fact that the rear of the pulse will now require extra time to reach the channel front, the pulse's propagation time in the laboratory frame will be larger than the pulse duration according to $\tau_{\mathrm{prop}} = \tau/(1 - v_{\mathrm{hb},\gamma}/c) = (1 + \Xi_{\mathrm{hb}})\tau$ [72]. Note however that by multiplying the relativistically correct hole-boring velocity by the propagation time yields the exact same equation as Eq. 2.119, thereby showing that this equation is consistent at all relevant intensity levels given a constant density profile.

While these equations are fairly robust at higher densities, discrepancies arise at densities below critical where the assumptions made in deriving Eq. 2.119 break down [73]. In this regime, the pulse will channel through the plasma instead of hole-bore. A more accurate description of the channeling depth, d_{ch}, is obtained by noting that the laser pulse initially interacts with the electron species primarily through the ponderomotive force, and after transferring its energy to electron quiver motion, this energy is then subsequently converted to several other forms which constitute the complex absorption process [74,75]. As a result, one can approximate d_{ch} by equating the deposited pulse energy to the quiver energy given to the electron species. To find this value, note that the energy given to each electron through the ponderomotive force is found by integrating Eq. 2.80, $\int \vec{f}_P \cdot d\vec{r} = (\gamma - 1)mc^2$ where $\gamma = (1 + a_0^2/\alpha)^{1/2}$, $\alpha = 1$ for circular polarisation and $\alpha = 2$ for linear polarisation. Multiplying this by the number of electrons in the channel gives $U_P = (\gamma - 1)mc^2 d_{\mathrm{ch}} \bar{n}_e A$ where A is the cross-sectional area of the pulse, the volume of the channel has been approximated as $V = A d_{\mathrm{ch}}$, and the average density $\bar{n}_e = V^{-1} \int n_e \; dV$.

The total ponderomotive energy needs to be equated to the amount of laser energy used to create the channel, $U_L = \zeta I A \tau = (1/2) \zeta n_c m c^3 a_0^2 A \tau$ where ζ is the coupling parameter indicating the fraction of the pulse energy contained within the channel. This value can vary in 2D simulations with little filamentation present from $\zeta \approx 1$ in p-polarisation [74] to values as low as $\zeta \approx 0.6$ in s-polarisation [64]. The difference between the two polarisations lies in the escaping pulse energy in s-polarisation case which will then continue on to form soliton-like structures [64–66, 68, 76] as described in Section 2.7.3. Equating $U_L = U_P$ gives the channeling depth:

$$d_{\mathrm{ch}} = \frac{n_c}{2\bar{n}_e} \frac{a_0^2}{\gamma - 1} \zeta c \tau \equiv \Xi_{\mathrm{ch}} c \tau \tag{2.120}$$

Despite the simplistic assumptions made in deriving this equation, it has been shown to be a reasonable estimate for sub-picosecond pulses in relativistically transparent plasmas. Willingale *et al.* used a low-intensity approximation with the assumption of linear polarisation in the p-plane so that $\gamma - 1 \approx a_0^2/4$, $\zeta = 1$, and thus $d_{\text{ch}} \approx 2c\tau n_c/n_e$ and showed strong agreement between 2D PIC simulations and this final depth calculation [74]. However, it should be noted that for higher densities and longer pulse durations, the channel walls will become over-critical, thereby reducing the speed down to the hole-boring velocity. Thus d_{ch} and d_{hb} serve as upper and lower bounds respectively for the depth of a channel without significant hosing. It is also worth observing that the opposite assumption $a_0 \gg 1$ leads to $d_{\text{ch}} \approx c\tau\alpha n_{\gamma c}/2n_e$ where $n_{\gamma c} = \gamma n_c$ is the relativistically adjusted critical density, thereby reflecting the role of relativistic transparency in the channeling process.

Finally, note that d_{ch} was calculated by equating Lorentz invariant values. As a result, the average channeling velocity can be found by simply dividing d_{ch} by the pulse's total propagation time, $\tau + d_{\text{ch}}/c$, yielding:

$$\frac{v_{\text{ch}}}{c} = \frac{\Xi_{\text{ch}}}{1 + \Xi_{\text{ch}}} \tag{2.121}$$

This equation exactly mirrors Equation 2.117. In the regime of interest for this thesis, plasmas will generally be within an order of magnitude of critical density and $0.85 \leq a_0 \leq 30$. As a result, it can be assumed that $\Xi_{\text{hb}} \ll 1$ while $\Xi_{\text{ch}} \gg 1$

3

Numerical Studies and the Hosing Instability

Among the tools available for investigating laser-plasma interactions, numerical simulations provide the greatest access to information, giving the researcher the ability to observe all of phase space and even track individual particles. However, this of course comes at the cost of real-world accuracy. In an ideal case, individual particles would be simulated, taking into account field strengths and all interactions, and a high degree of accuracy could be obtained by refining the simulation's resolution. Unfortunately, this is unrealistic as the computational cost is well beyond what is feasible with today's technologies. As a result, various simulation methods have been developed to investigate plasma physics phenomena. Two of the most prevalent techniques are particle-in-cell (PIC) and radiation magneto-hydrodynamics simulations. Each has its advantages and disadvantages and is used to investigate different regimes of interest.

Radiation magneto-hydrodynamics codes, or "hydro" codes for short, treat the plasma as a fluid, largely ignoring kinetic effects but allowing larger-scale phenomena to be investigated. There are different varieties of hydro codes, though they generally fall into one of two categories. In both, the simulation is initially divided up into some form of grid. A Lagrangian hydro code then tracks the evolution of individual cells, allowing the grid to warp and move with each fluid parcel, while an Eulerian hydro code fixes the grid in place and calculates the flow between adjacent cells. Both of these methods are generally adequate for describing fluid instabilities and looking at the evolution of a centimeter-scale three dimensional system over a relatively large amount of time (nanoseconds). In general, hydro codes are only suitable when the collisional mean free path of the particles is far smaller than the interaction region, as described by Equation 2.94. For the purposes of this thesis, radiation hydrodynamic simulations from HYDRA [43], an arbitrary Lagrangian-Eulerian code, and FLASH [44], an Eulerian code with Lagrangian tracking particles, were used primarily to determine the plasma profile with which a high-intensity pulse would be likely to interact in inertial confinement fusion and the experiment discussed in Chapter 5. However, the interactions with short scale lengths required alternative simulation methods.

To address this, the bulk of the numerical investigations examined herein, and indeed all that are critically analysed, were performed using the PIC code, OSIRIS [42]. PIC codes attempt to recreate kinetic effects by modeling groups of particles. These groups – often referred to as super-particles or simply particles within the codes – are then overlaid with a grid onto which the electric and magnetic fields are cast. The evolution of the particles and the fields then proceed in a leap-frog manner. In one half time step, the force on each particle is calculated by interpolating the fields from the grid to the particle's position. This determines the acceleration and allows the particle's momentum to be updated. Then during the second half time step, each particle's position is updated based on its momentum. After the particles have been moved, the spatial current and charge distributions may be determined and used to calculate the fields at each grid point by solving Maxwell's equations. In this way, every pair of particles' interaction need not be considered, thereby greatly reducing the computation time. Even with this cost saving, PIC codes are much slower than hydro codes and are primarily suitable for two-dimensional spaces up to around a square millimeter over the span of tens of picoseconds, though spatially reduced three-dimensional simulations can be run as well.

This chapter reports on various numerical investigations which focus on the propagation of high intensity pulses of picosecond durations through plasmas relevant to the experiments described in Chapter 5 and inertial confinement fusion in general. Early into this work, it became clear that the hosing instability is one of the greatest challenges to controlling the channeling of these pulses. As a result, the remainder of this chapter will be divided as follows. First, some background information on the simulation parameters will be presented in Section 3.1. Then Section 3.2 will show early simulations which illustrated the need for a more comprehensive understanding of the hosing instability. Next, analytical work will be presented in Section 3.3 which models this instability and derives a new density dependence that was previously neglected in the literature. The relevance of this dependence will then be tested in Section 3.4. The implications of this dependence on proposed channeling schemes will be shown in Section 3.5. Preliminary simulations exploring the coupled effects of intensity and external perturbations on the pulse propagation follow in Section 3.6. Finally, additional observations on phenomena appearing throughout these simulations are discussed in Section 3.7. The chapter will then end with a validation of the simulation parameters used in Section 3.8.

Unless otherwise noted, all simulations performed for this research were run using OSIRIS, a two-dimensional, fully relativistic, massively parallel particle-in-cell code [42], on the ARCHER UK National Supercomputing Services [77]. Because this chapter features several PIC simulations, each subsection's fixed parameters will be summarized in tabular form for ease of referencing. Further, the simulations presented herein all utilize temperatures in excess of 1 keV. According to Equation 2.94, the mean free path of the particles will generally be on the scale of 100 µm which is generally larger than the interaction regions of interest, thus making it acceptable to assume a collisionless plasma.

3.1 Particle-in-Cell Methods

As stated in the introduction to this chapter, PIC simulations update the particle locations and momenta from field data stored on a grid. In turn, the electric and magnetic fields are then updated based on the new particle data by solving Maxwell's equations. How this is done has several consequences for the results of the simulations. This section therefore will focus on a discussion of the simulation parameters which do not directly relate to physical quantities but are still vital when designing a simulation. For simplicity, 1D Cartesian geometry will be assumed, following the arguments of Birdsall and Langdon [78].

Consider the process of updating the charge density on the grid. The simplest method is to iterate over every particle and add its charge to the nearest grid point, a process known as zero-order weighting. While this is a computationally efficient method, it leads to large amounts of noise. As soon as a particle moves closer to the next grid point, its entire charge will be cast to the new location. Thus a particle moving only a small fraction of a cell width will effectively have its charge moving the entire width, thereby resulting in large levels of noise.

A slightly more computationally intensive approach is to apply linear interpolation of a particle to its nearest neighbours. This in effect produces a triangularly shaped particle as opposed to the square-top particle found in zero-order weighting (see Figure 3.1). By smoothing the particle shape, the noise resulting from interpolation is reduced. Higher orders of weighting can be achieved by using splines to smooth the particle shape and reduce noise still further. Note that this particle shaping method is also applicable to field shapes when casting the forces back to the particles. All simulations presented in this thesis were run using first-order weighting.

In addition to which weighting method is used, the number of particles per cell (PPC) will also affect the noise levels present in a PIC simulation. As in this chapter's introduction, particles in PIC codes actually represent super-particles consisting of many physical particles. As the acceleration from the Lorentz force only depends upon the charge-to-mass ratio, many particles of the same species can be combined into a super-particle and it will still follow a realistic trajectory. However, these trajectories will clearly vary based on their initial positions. Thus, dividing the plasma into more super-particles will allow more of these paths to be simulated and smoother, more realistic results to be obtained, thus reducing the particle noise.

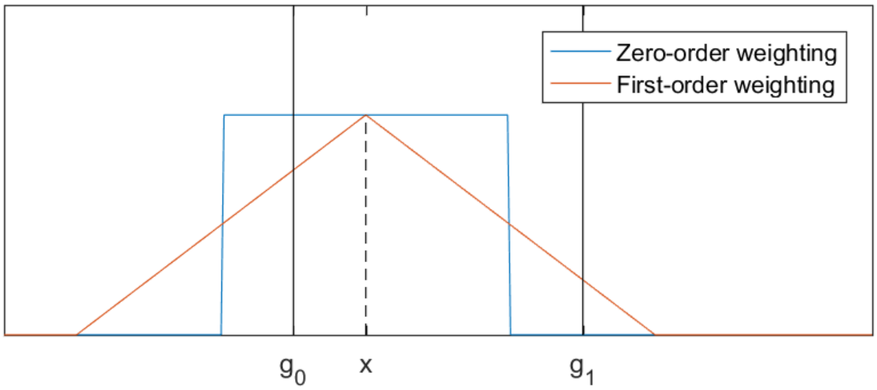

Figure 3.1: Particle shapes in particle-in-cell simulations. A particle is located at position x between grid points g_0 and g_1. Zero-order weighting (nearest neighbour) can be represented in a square top particle with width equal to the cell size. First-order weighting (linear interpolation) is represented by a triangular particle with width equal to twice the cell size. The magnitude of these curves at each grid point is equivalent to their respective interpolation methods.

In each simulation set's summary table, the PPC is represented as $N \times M$. This represents the manner in which the particles were created in two dimensions. For instance, 4×4 means that the individual particles in each cell were originally divided four times vertically and four times horizontally into sixteen super-particles per cell.

Another relevant simulation parameter is the cell size. Both of the above mentioned parameters, particle shapes and particle numbers, are dependent upon the distance between grid points. Typically, the cell size should resolve both the Debye length, $\lambda_D = v_{\text{th}}/\omega_p$ and the skin depth, $\delta > c/\omega_p$. Note that $\lambda_D < \delta$, so if λ_D is resolved, δ will be as well. As the grid holds all of the field information, if λ_D is not resolved, fields which should be shielded out through Debye shielding will continue to affect distant particles within the cell. As a result, energy will not be conserved, and the plasma will artificially heat until the plasma's Debye length matches the grid resolution.

When simulating dense plasmas, λ_D will be quite small. Even a 1 keV plasma at critical density for a pulse with a 1 µm wavelength has a Debye length of just 7 nm, thereby requiring over 140,000 grid points per millimeter. This quickly becomes computationally infeasible, especially in multi-dimensional simulations, and so plasmas are often simulated to be either hot, low density, or spatially small. In general, simulations presented in this thesis attempt to resolve the Debye length to within a few multiples of λ_D.

This high computation cost restricts the possible size of the simulation window. Since the window is often comparable in size to the interaction region being investigated, boundary conditions (BC) have important consequences. There are always two sets of boundary conditions for any PIC code: one for the fields and one for the particles. The field boundary conditions are typically either open, reflecting, or periodic, where "open" means particles and fields are only permitted to exit the window, and the name of the last two being self-descriptive. The boundary conditions for particles are similar, though there is the additional option of a thermal bath. In this case, when a particle exits the window, a new particle will be created and injected at the same position. The momentum of this new particle is calculated based on a pre-determined thermal distribution, and generally, its direction of propagation is chosen at random. Unless otherwise noted, open boundary conditions were used in all simulations presented here.

One final simulation parameter to consider is the time resolution. The evolution of fields and particle movement are calculated by solving a set of partial differential equations using the finite differences method. In order to maintain stability when time integrating, the Courant condition must be satisfied so that a wave may not propagate further than the grid size in one time step. This is given by [78]:

$$\frac{1}{(c\Delta t)^2} > \sum_{i=1}^{N} \frac{1}{\Delta x_i^2} \tag{3.1}$$

where Δt is the time resolution, N is the dimensionality of the simulation, and Δx_i is the spatial resolution in the i-th dimension. If the time resolution is too large and the Courant condition is violated, the electric and magnetic fields will grow exponentially. All simulations presented here therefore by necessity obey this condition.

Physically, the phenomena of interest in investigating channeling are generally on the order of the laser pulse's wavelength. For this thesis, that implies that a resolution of at least a tenth of that wavelength, 100 nm in space and 0.2 fs in time, is desirable in order to observe the various effects discussed in Section 2.7. Fortunately, by requiring the simulations to be resolved to roughly the Debye length ($\sim 10\,\text{nm}$) and the Courant-imposed time resolution ($\sim 0.02\,\text{fs}$), both of these conditions are easily met and no additional resolution refinement is required.

3.2 Motivating Simulations

As pulses propagate through a plasma, they will undergo several instabilities as described in Section 2.7. In particular, the filamentation and hosing instabilities will grow over time and cause the pulse to bifurcate and each filament to redirect respectively. These are two of the most detrimental instabilities to occur when attempting to form a controlled channel.

The hosing instability occurs when a pulse's centroid is offset from its original path due to a phase velocity gradient, often in the form of a density perturbation. While offset, the pulse will continue to expel electrons from its path. However, this process will increase the gradient and cause the pulse to veer even further off path, eventually leading to a fully redirected beam. The hosing equation in the long wavelength regime of a Gaussian beam of frequency ω_0 and dimensionless vector potential a_0 is given by [79]:

$$\frac{\partial^2 X_c}{\partial \tau^2} + \frac{1}{4}\frac{c^2\langle a_0^2\rangle}{\omega_0^2 W^2}\frac{\partial^2 X_c}{\partial \psi^2} = 0 \tag{3.2}$$

where X_c is the centroid's transverse position, $\tau = t$ and $\psi = t - z/c$ are the speed of light frame variables for a pulse traveling in the z direction, and W is the width of the pulse. This equation will be revisited in Section 3.3 where an extended derivation will be presented. For now, it is worth noting that when the centroid's path is at a local maximum, $\partial_\psi^2 X_c \leq 0$. Equation 3.2 then dictates $\partial_\tau^2 X_c \geq 0$, thereby increasing the displacement still further and leading to the pulse runaway. This section describes two series of simulations which were designed to investigate this instability further.

3.2.1 Shoveling Pulses: Intensity Ramp

In order to mitigate the effects of the hosing instability, an early set of large-scale simulations was designed to investigate the effects of a train of pulses of increasing intensity. In principle, each pulse channels until either the pulse is depleted or the relativistically adjusted critical density is reached. The next pulse then immediately follows with an increased intensity. This method has a few potential benefits. The lower intensity pulses require less energy than their high-intensity counterparts. According to the physical model presented in Section 2.7.6, they do not penetrate as deeply due to pulse depletion and reduced levels of relativistically induced transparency. Additionally, according to Equation 3.2, they do not hose as much since their a_0 values will be lower. Thus they can be utilized to form guiding channels through the low density plasma for the higher intensity pulses. These channels are of sufficiently low density as to minimally affect propagation, so the trailing pulses do not undergo as much filamentation according to Equation 2.113, thus allowing the overall channel to be more contained. Finally, because the intensities continue to increase, they are able to penetrate beyond the critical surface of the previous pulse due to relativistically induced transparency, in effect "shoveling" deeper into the plasma.

The parameters for these simulations are shown in Table 3.1. Note that OSIRIS is run using dimensionless variables, so a fundamental wavelength, λ_0, must be chosen in order to convert to physical units. $\lambda_0 = 1.053\,\mu\text{m}$ was chosen here to reflect a common wavelength found in Nd:glass-based laser facilities. The electron density profile had a 200 µm scale length up to a maximum of $12n_c$ which was matched by an ion species meant to simulate deuterium which therefore had a 1/3670 charge-to-mass ratio compared to the electron species. The resolution was $23.8\,\text{nm} \times 23.8\,\text{nm}$ with 4×4 PPC.

An initial simulation was run utilizing a train of five pulses with increasing intensities, each of 0.5 ps duration and with 1 ps peak-to-peak separation between them in order to allow the plasma to relax between pulses. This simulation will

Simulation Parameters

λ_0	1.053 µm
Window size	1000 µm × 150 µm
Grid	42,000 × 6300
PPC	4 × 4

Plasma Parameters

$n_{e0} = n_{i0}$	$12 \exp[(z - 1000\,\mu\mathrm{m})/200\,\mu\mathrm{m}]\ n_c$
$\lvert q_e/m_e \rvert$	$3670\ \lvert q_i/m_i \rvert$
$T_{e0} = T_{i0}$	2 keV

Pulse Parameters

t_{rise}	125 fs
t_{flat}	250 fs
t_{fall}	125 fs
Polarisation	s-polarised
Focal Position	73.4 µm
Focal Radius	5.3 µm

Table 3.1: Summary of parameters used in the intensity ramp simulations. t_{rise} and t_{fall} indicate the durations over which the pulses increased to and decreased from their maximum vacuum intensities using a half-Gaussian profile.

t_{start}	a_0 (Set 1)	a_0 (Set 2)	a_0 (Set 3)
0 ps	0.1	0.33	-
1 ps	0.33	0.33	0.33
2 ps	1	0.33	-
3 ps	3.33	3.33	3.33
4 ps	10	10	10

Table 3.2: Pulse timings and intensities used in the intensity ramp simulations.

be referenced as Set 1. A description of all pulse timings and intensities used in this section are shown in Table 3.2.

The electron density at various times is shown in Figure 3.2 for each simulation in this section. As can be seen from these images, the channel in Set 1 did not begin to noticeably form until the second pulse began its propagation. As the higher intensity pulses entered the window, the channel continued to expand, guided by the previously formed density perturbations. After exiting the pre-formed channel and upon reaching higher densities, the pulse began to experience strong hosing, redirecting the centroid's path away from the original propagation axis.

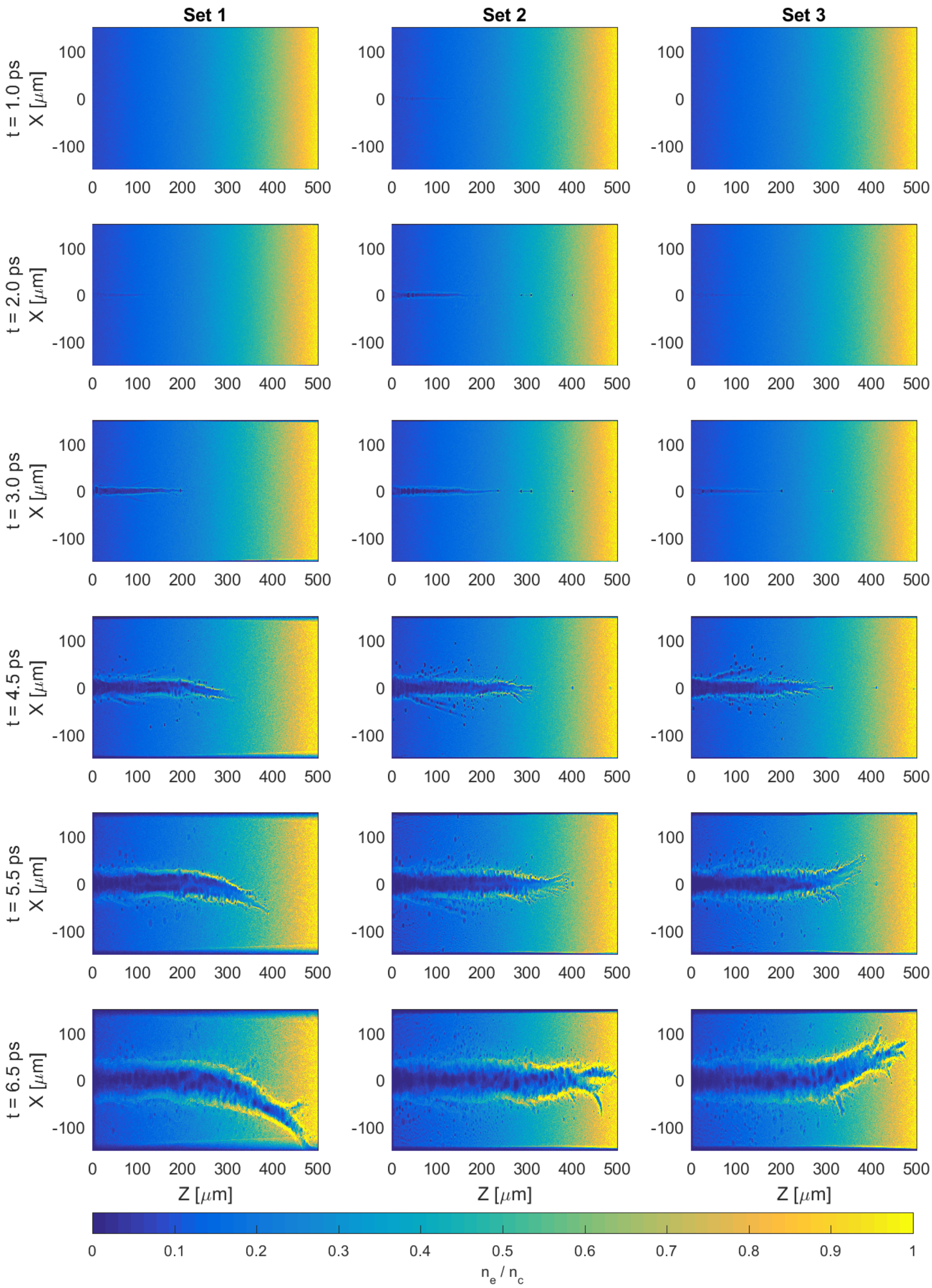

Figure 3.2: Electron density profiles of intensity ramp simulations. The electron density for each of the three simulations run in Section 3.2.1 are shown at select times. Pulses entered the window from the left and traveled in the z direction. Only the interaction region ($z < 500\,\mu\text{m}$) is shown.

Additionally, several bubble-like structures known as solitons can be seen in these simulations, as predicted in Section 2.7.3. These solitons are the results of laser pulse energy escaping the channel and propagating through the plasma. As these divergent beamlets continue interacting with the plasma, they adiabatically decrease in energy, leading to a redshift of the radiation which causes the walls around them to become over-critical and trapping the pulse energy inside to form a soliton [66, 68]. As the light couples with the electrons and ponderomotively keeps the electron density negligible within the soliton, a charge separation is formed between the electrons and ions. The ions then are accelerated out of this bubble region leading to what is known as a post-soliton [62, 80].

The first pulse's power, $P_1 \approx 9.7\,\mathrm{GW}$, was extremely low for a channeling beam. As a result, the ponderomotive force was too weak to displace the electrons a sufficient distance to set up a large enough charge separation to cause the ions to react on this timescale, the power threshold for which is given by $P_{\mathrm{ch}} \approx 17\,n_c/n_e\,\mathrm{GW}$ [81–83]. Set 2 therefore was designed to be identical to Set 1 but with the first three pulses' intensities all set equal to $a_0 = 0.33$. As all three leading pulses were able to expel ions and electrons, the channel for Set 2 was able to achieve a greater depth at $t = 3.0\,\mathrm{ps}$ than Set 1. Some slight hosing can be observed at this time, though not of any significant magnitude. This channel then guided the remaining two high-intensity pulses through the plasma. Again, hosing was evident at higher densities in various filaments, though the main pulse's centroid remained on path.

Finally, to investigate the extent to which the low-intensity pulses affected the propagation of the higher intensities, Set 3 used only a single $a_0 = 0.33$ pulse. The quality of the resulting channel was similar to that of Set 1 with strong hosing occurring at approximately the same point.

From these simulations, a few details are apparent. In order for the original idea behind this scheme to work, the pulses need to be of much greater duration so that they each are able to approach their relativistically adjusted critical densities. As it is, pulse depletion causes the channels to stop well short of even the non-relativistically adjusted critical density. Future investigations to examine these longer durations will require a significant amount of computational resources to ensure the Debye length is resolved. Otherwise numerical instabilities would risk invalidating the results of simulations with much longer run times.

One further observation is that the hosing of the pulses occurred both as the intensities increased and as the pulses propagated through higher densities. As a result, the low-intensity pulses apparently were capable of guiding the high-intensity pulses through the plasma to maintain control of the channel while still being able to increase the intensity, as expected. However, it is difficult to determine from these simulations alone whether the increased hosing was solely due to the increased intensities of the pulses, or if the greater densities played a role as well. Additional simulations are required to truly verify that the improved channeling of Set 2 is a physically systematic improvement rather than a result of the hosing instability's stochasticity.

3.2.2 Density and Frequency Exploration

Another set of simulations was performed, this time to explore the effects of density and frequency on the hosing instability. In order to accomplish this, five simulations were run, the parameters of which are given in Table 3.3.

A 2 ps pulse entered the left side of a 250 μm × 100 μm window into a plasma with an exponentially increasing density profile of scale length 41.67 μm. The five simulations were divided into two sets. Each set featured three simulations which varied the pulse frequency between 1ω, 2ω, and 3ω, corresponding to wavelengths of 1.053 μm, 0.527 μm, and 0.351 μm respectively, with the 3ω simulation being included in both sets. Every simulation held the total energy of the pulse constant. Given that $a_0 \propto \lambda$, this means that a_0 was reduced during the higher frequency simulations according to $a_0 = 9\omega_0/\omega$ where ω_0 is the fundamental frequency of the simulation which in this case matches the frequency of the 1ω pulse.

The first set, hereafter referred to as the "scaled" simulations, held the maximum density constant relative to each pulse's relativistically adjusted critical density at $n_{\max} = 1.2 n_{\gamma c}(\omega)$. Note that $n_{\gamma c} = \gamma n_c = (1 + a_0^2/2)^{1/2}(\omega/\omega_0)^2 n_{c0}$ where n_{c0}

Simulation Parameters

λ_0	1.053 µm
Window size	250 µm × 100 µm
Grid	38,400×8280
PPC	3 × 3
Transverse BC	Periodic

Plasma Parameters

$n_{e0} = n_{i0}$	$n_{\max} \exp[(z - 250\,\mu\text{m})/41.67\,\mu\text{m}]$
$\lvert q_e/m_e \rvert$	$3670\ \lvert q_i/m_i \rvert$
$T_{e0} = T_{i0}$	20 keV

Pulse Parameters

a_0	$9\omega_0/\omega$
t_{rise}	0.5 ps
t_{flat}	1.5 ps
t_{fall}	0.5 ps
Polarisation	p-polarised
Focal Position	57.6 µm
Focal Radius	5.3 µm

Table 3.3: Summary of parameters used in the frequency simulations.

Frequency	$n_{\max}$ (Scaled)	$n_{\max}$ (Fixed)
1ω	$7.73\ n_{c0}$	$25.3\ n_{c0}$
2ω	$16.0\ n_{c0}$	$25.3\ n_{c0}$
3ω	$25.3\ n_{c0}$	

Table 3.4: Summary of maximum densities used in the frequency simulations. n_{c0} is the critical density for the fundamental frequency of the simulation.

is the non-relativistically adjusted critical density for the fundamental frequency of the simulation. Meanwhile, the second set of "fixed" simulations held the maximum density absolutely constant using the 3ω simulation's profile. These values are summarized in Table 3.4.

The results of the scaled simulations are shown in Figure 3.3. The three simulations all experienced some degree of hosing. The 1ω simulation began to experience hosing before 1 ps had passed within the simulation, occurring around $z = 140\,\mu\text{m}$. Hosing in the other two was still present, though it began deeper into the channels at about $z = 170\,\mu\text{m}$ for both.

It is worth noting that the channeling velocities of the three pulses all were

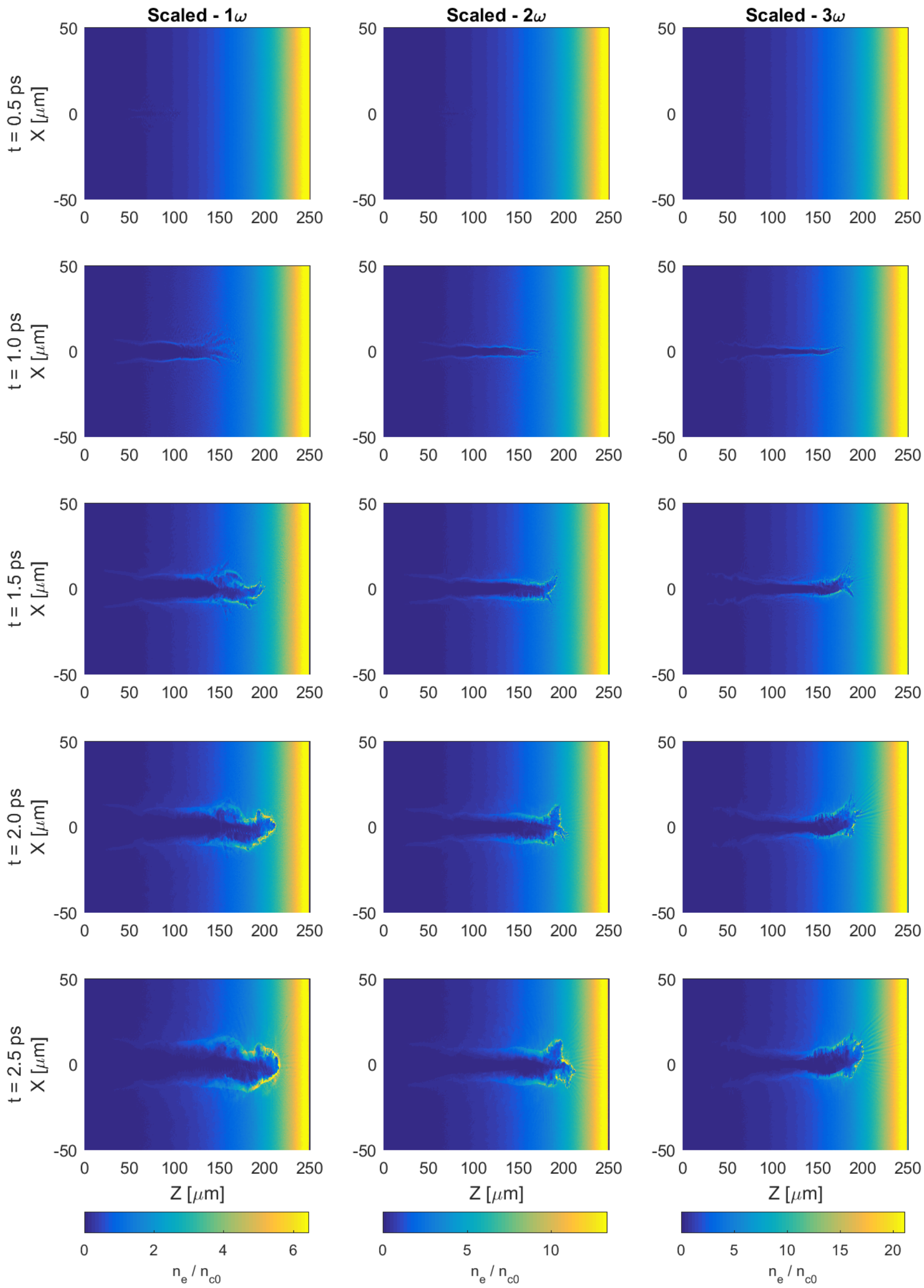

Figure 3.3: Electron density profiles of the scaled frequency simulations. Each column depicts a single simulation at various time steps as labeled. The colour scale is set to have a maximum value equal to the relativistically adjusted critical density for each simulation. The colour bars are labeled relative to the critical density for a 1ω pulse.

approximately constant despite their a_0 values and the absolute density levels varying. As a result, the position of hosing within the window can be used to determine the relative timing of the hosing instability's runaway growth.

To determine why the velocities remain roughly constant, recall that the channel depth derived in Section 2.7.6 for a linearly polarised pulse is given by

$$\begin{aligned} d_{\mathrm{ch}} &= \frac{n_c}{2\bar{n}_e}\frac{a_0^2}{\gamma - 1}\zeta c\tau \\ &= \frac{n_{\gamma c}}{\bar{n}_e}\frac{a_0^2}{a_0^2 - 2(1 + a_0^2/2)^{1/2} + 2}\zeta c\tau \\ &\approx \frac{n_{\gamma c}}{\bar{n}_e}\zeta c\tau \end{aligned} \tag{3.3}$$

where ζ is a constant measuring the percentage of laser energy confined within the channel. The last step assumes $a_0 \gg 1$. As can be seen from this equation, the channel depth varies only weakly with the pulse intensity other than the adjustment to the critical density, but it is directly proportional to $(n_e/n_{\gamma c})^{-1}$. In general then, it is this factor rather than the absolute density or intensities which determine the final depth for a highly relativistic pulse.

However, the simulations here do not have $a_0 \gg 1$, with the 3ω simulation at only $a_0 = 3$. Because of this, the 3ω simulation should reach approximately 23% deeper than the 1ω simulation. In actuality, the 1ω simulation penetrated deeper than the 3ω simulation. The reason for this is that the high density sheath which surrounds the channel has built up to overdense levels. This is the effect predicted in Section 2.7.6. Consequently, continued channel formation was the result of momentum transfer from the photons to the ions in the sheath, thus reducing the channeling velocity down to the hole-boring velocity, Equation 2.115, $v_{\mathrm{hb}} \propto (I/n_i)^{1/2}$. Thus, while the higher frequency pulses will channel deeper into the plasma initially due to their lower a_0 values, the 1ω will hole-bore with higher velocity since it is channeling through a lower absolute density plasma. This matches what is seen in the simulations where after 1 ps the 1ω pulse has only channeled 130 µm into the plasma while the 3ω has reached 162 µm, but the final channel depths are 215 µm and 196 µm respectively. These depths were calculated by finding the maximum depth to which the pulse has caused the density to fall below 50% of its initial value.

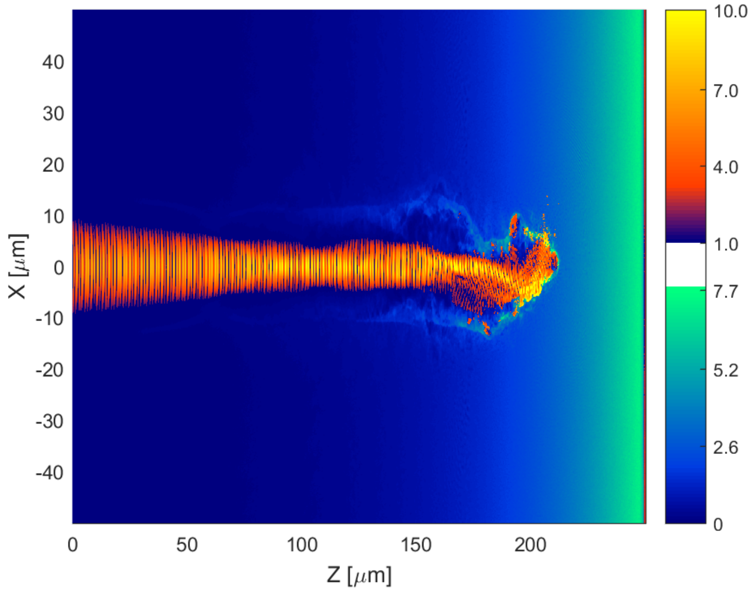

Figure 3.4: Pulse intensity and electron density overlay of the 1ω scaled frequency simulation after 2.0 ps. The pulse intensity is only shown for $a_0 > 1$. The density map is in units of the fundamental wavelength's critical density. Specular reflection occurs near the end of the channel, indicating that channel formation has become hole-boring.

The transition from channeling to hole-boring can be seen by looking at images of the channel overlaid with the pulse intensity. When the pulse ceases to propagate forward through the plasma and instead begins to specularly reflect off of the front channel wall, the pulse will have transitioned from the channeling regime to the hole-boring regime. An example of this is shown in Figure 3.4 for the 1ω simulation after 2.0 ps of simulation time. As can be seen in this image, no significant pulse energy has exited the head of the channel while strong reflection my be observed near the front of the pulse, thus indicating hole-boring.

The results of the fixed simulations, shown in Figure 3.5 were similar overall, though there are a few notable differences. Primarily, hosing seems to have begun at earlier times for both the 1ω and 2ω simulations. Perturbations began after 0.5 ps for the 1ω pulse and after 1.0 ps for the 2ω pulse. However, after a short amount of time, the pulses are able to ponderomotively self-correct their course and continue on the original path until hosing again. This self-correction will be revisited later in Section 3.7. Given that **k** is real, from Equation 3.2, the growth

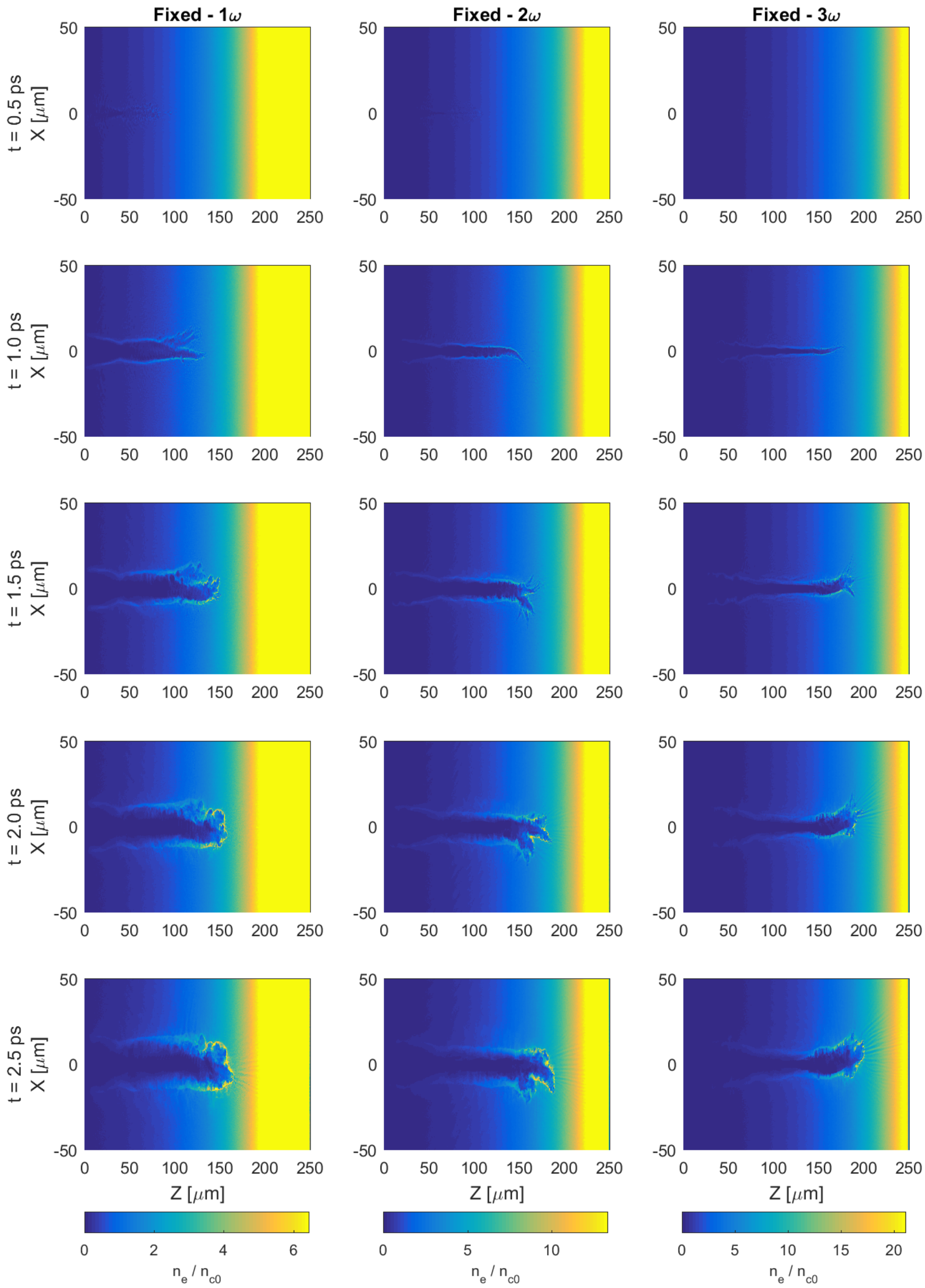

Figure 3.5: Electron density profiles of the fixed frequency simulations. As with Figure 3.3, each column depicts a single simulation at various time steps as labeled. The colour scale is set to have a maximum value equal to the relativistically adjusted critical density for each simulation, though here, the density profiles all matched the 3ω simulation. The colour bars are labeled relative to the critical density for a 1ω pulse.

rate of the hosing instability in the long wavelength regime is given as:

$$\begin{aligned} \gamma_h &= \frac{c}{2\alpha}\frac{a_0}{\omega_0 W} \\ &\propto \frac{I^{1/2}}{\omega_0^2 W} \end{aligned} \tag{3.4}$$

where $\alpha = 1$ for circular polarisation and $\alpha = 1/2$ for linear polarisation. This is only dependent upon the pulse parameters. However, this does not explain the increased hosing when the plasma density increased. Indeed, even in the scaled simulations, hosing occurred earlier in the 1ω simulation than the 2ω and 3ω simulations as predicted by Equation 3.4, but there was no noticeable difference between the 2ω and 3ω simulations. If this equation were a truly complete description, the 3ω simulation would have experienced significantly less hosing than any of the other simulations.

In deriving Equation 3.2, the density was assumed to be far below critical density. However, the hosing which is occurring in both the scaled and fixed simulations is doing so in regions comparable to critical. Thus it was necessary to return to the analytical work which derived Equation 3.2.

3.3 The Hosing Instability

It is important to understand the physical mechanism by which the hosing instability causes a channeling beam to change its direction. As a laser pulse propagates through a plasma, its path undergoes slight perturbations due to transverse asymmetries in the phase velocity about the pulse's centroid, often due to changes in the density profile. These asymmetries then lead to a tilting of the pulse's wavefront and thus its propagation direction. Once this path has been altered, the pulse continues to expel electrons via the ponderomotive force, and by doing so, it increases the phase velocity gradient, causing what would have been a small amount of refraction to lead to a large displacement of the centroid. Therefore, in order to derive these transverse asymmetries, it is important to first derive an equation for the phase velocity by considering the perturbations of the relevant parameters.

The derivation presented here is based on the physical picture given by Ren and Mori [79] but with the allowance of larger densities and ultra-intense ($a_0 \gg 1$) pulses.

To begin, assume an ideal case where a pulse with a table-top transverse profile is propagating through an underdense plasma. Then assuming the density, frequency, and intensity initially vary little in the region of interest, one can set $n_e = n_0 + n_1$, $\omega = \omega_0 + \omega_1$, and $a_0^2 = a_{00}^2 + a_{01}^2$ where subscripts 0 denote the fixed components and subscripts 1 denote the varying components. Because the maximum frequency shift of the pulse as it passes through the plasma is given as $\omega_1/\omega_0 \propto (\omega_p^2/\omega^2)n_1/n_0$ [84] and phenomena such as the filamentation instability only become appreciable with density modulations of the order $n_1/n_0 \sim 1 - e^{-\gamma_p} \to 1$ for high intensities where γ_p is the ratio of the ponderomotive pressure to the thermal pressure [85], confining the analysis to times such that $n_1 \ll n_0$ will inherently result in $\omega_1 \ll \omega_0$ and $a_{01}^2 \ll a_{00}^2$. Then using these values, substituting into the phase velocity equation, $v_\phi = c\eta^{-1}$, and linearizing shows:

$$
\begin{aligned}
\frac{v_\phi}{c} &= \left(1 - \frac{n}{\gamma n_c}\right)^{-1/2} \\
&= \left[1 - \frac{n_0}{n_{\gamma c0}}\left(1 + \frac{n_1}{n_0} - \frac{1}{2}\frac{a_{01}^2}{\gamma_0^2} - 2\frac{\omega_1}{\omega_0}\right)\right]^{-1/2} \\
&= \sqrt{\frac{n_{\gamma c0}}{n_{\gamma c0} - n_0}}\left[1 - \frac{n_0}{n_{\gamma c0} - n_0}\left(\frac{n_1}{n_0} - \frac{1}{2}\frac{a_{01}^2}{\gamma_0^2} - 2\frac{\omega_1}{\omega_0}\right)\right]^{-1/2}
\end{aligned}
\tag{3.5}
$$

where $\gamma_0 = (1 + a_{00}^2)^{1/2}$, $n_{c0} = m\epsilon_0\omega_0^2/e^2$, and $n_{\gamma c0} = \gamma_0 n_{c0}$.

In order to see how phase velocity asymmetries affect the propagation direction of a pulse, consider a pulse with a table-top transverse profile propagating through a plasma with a slight perturbation to the electron density such that there is a transverse density gradient as illustrated in Figure 3.6. Let $\Delta\theta$ be the angle between the pulse's current trajectory compared to its original trajectory and let $\hat{x}$ be the transverse direction. As can be seen from this figure, the change in propagation direction is given by $\tan(\Delta\theta) = (v_{\phi 0} - v_{\phi 1})\Delta t/(x_0 - x_1)$, or by letting Δt tend towards zero:

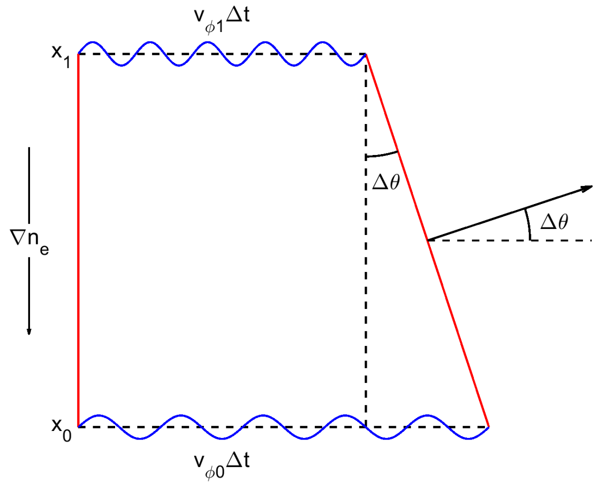

Figure 3.6: Schematic of phase velocity asymmetries affecting the propagation of a pulse in an underdense plasma.

$$\frac{\partial\theta}{\partial t} = -\frac{\partial v_\phi}{\partial x} \tag{3.6}$$

In general, the pulse frequency and intensity will be symmetric about the centroid of the pulse, and so they will have little effect on the hosing instability [79]. Therefore, when inserting Equation 3.5 into Equation 3.6, only the density term will remain:

$$\frac{\partial\theta}{\partial t} = -\frac{c}{2}\frac{n_0}{n_{\gamma c0}}\left(1 - \frac{n_0}{n_{\gamma c0}}\right)^{-3/2}\frac{\partial}{\partial x}\frac{n_1}{n_0} \tag{3.7}$$

Assuming θ is small, the rate of change of the displacement of the centroid is given as $\partial_t X_c = v_\phi \theta$ where X_c is the transverse location of the centroid. Taking the derivative with respect to time of this equation and noting that $\theta\partial_t v_\phi \ll v_\phi \partial_t \theta$ since n and therefore v_ϕ vary little in the region of interest and $\theta \ll 1$, it can be shown that:

$$\frac{\partial^2 X_c}{\partial t^2} = -\frac{c^2}{2}\frac{n_0}{n_{\gamma c0}}\left(1 - \frac{n_0}{n_{\gamma c0}}\right)^{-2}\frac{\partial}{\partial x}\frac{n_1}{n_0} \tag{3.8}$$

Note that in the limit $a_0 \ll 1$ and $n \ll n_c$, Equation 3.5 becomes $v_\phi/c = 1 + (n_0/2n_{c0})(1 + n_1/n_0 - \langle a_0^2\rangle/2 - 2\omega_1/\omega)$ by Taylor expanding the square root term, and Equation 3.8 becomes $\partial_t^2 X_c = -(1/2)(c^2 n_0/n_{c0})\partial_x(n_1/n_0)$ which both exactly match the equations found in Reference [79, 86].

Here already, the new density dependence of $(1 - n_0/n_{\gamma c0})^{-2}$ is given. At this point, all that is left to determine is the density response equation which accurately reflects the effects of the interacting laser pulse on the plasma's density profile. For short-pulses, the first-order response of the density profile due to the pulse is given by [86]:

$$\left[\frac{\partial^2}{\partial\psi^2} + \omega_p^2\right]\frac{n_1}{n_0} = \frac{\partial^2}{\partial\psi^2}\frac{\langle a_0^2\rangle}{2} \tag{3.9}$$

where $\psi = t - z/c$ is the speed-of-light frame longitudinal axis. This equation assumes that the ion motion due to direct acceleration by the laser pulse is negligible compared to the electrostatic force from the charge separation of the electron and ion species [87], thereby limiting the scope of the remainder of this section to pulses whose intensity is not sufficient to accelerate ions up to the relativistic regime ($I\lambda_\mu^2 < 10^{24}\,\mathrm{W\,cm^{-2}}$).

Then in the long wavelength regime ($\partial^2/\partial\psi^2 \ll \omega_p^2$), assuming near the centroid the intensity can be expressed as approximately $a_0^2 \rightarrow a_0^2[1 - (x - X_c)^2/2W^2]$, the density gradient caused by the pulse itself is given as:

$$\frac{\partial}{\partial x}\frac{n_1}{n_0} = \frac{\langle a_0^2\rangle}{2W^2(\omega_p^2/\gamma)}\frac{\partial^2 X_c}{\partial\psi^2} \tag{3.10}$$

where W is the spot size of the pulse. Inserting this into Equation 3.8 leads to:

$$\frac{\partial^2 X_c}{\partial t^2} = -\frac{1}{4}\frac{c^2\langle a_0^2\rangle}{\omega_0^2 W^2}\frac{1}{(1 - n_0/n_{\gamma c0})^2}\frac{\partial^2 X_c}{\partial\psi^2} \tag{3.11}$$

This equation matches Equation 3.2 but with the addition of a factor of $(1 - n_0/n_{\gamma c0})^{-2}$. This is an important distinction as many applications of hole-boring require channeling through moderate to near-critical densities. It shows that while pulses tend to hose more at higher densities, relativistic intensities are capable of mitigating this effect through the increase of the relativistic critical density. It is worth noting that this equation reduces to exactly the previously presented hosing equations when making the matching assumption of $n \ll n_c$.

Other density response equations and intensity profiles can be chosen to produce slightly different results from Equation 3.11, though Equation 3.8 will still need to be utilized in order to determine the acceleration of the centroid, thereby maintaining the density dependence. In weakly relativistic hole-boring for instance, an alternative description is obtained by setting the ponderomotive and wakefield potentials equal to each other, giving $n_1/n_{\gamma c0} \approx (c^2/\omega_0^2)\nabla^2 a^2/4$. Combined with a half-cycle cosine function for the intensity profile, to first order in X_c, this produces a harmonic oscillator equation with [88]:

$$\lambda_{\text{hosing}} \approx \frac{4\sqrt{2}\lambda_0^2}{a_0 W}\left(\frac{n_{\gamma c0}}{n_0}\right)^{3/2}\left(1 - \frac{n_0}{n_{\gamma c0}}\right) \tag{3.12}$$

This shows that at higher densities, the hosing wavelength will be shorter than previously predicted due to the increased transverse acceleration predicted in Equation 3.8, tending towards zero at the relativistically adjusted critical density. Further adjustments can be made to the density response equations, including the effects of ion motion on the electron density which has been shown to reduce hosing levels when using non-relativistic intensity laser pulses [89], though these effects are outside the scope of this thesis.

3.4 Verification of Density Dependence

In order to test the density dependence derived in the previous section, a pulse interacting with a plasma of constant density was simulated with the density varying between runs. All pulses used in this section have a rise and fall time of 0.5 ps and maintain their maximum intensity for 2.5 ps, giving a FWHM duration of 3.0 ps. An illustration of this temporal profile is shown in Figure 3.7. In each simulation, a single pulse is propagated from the right of the simulation window into a 100 µm × 100 µm plasma layer of constant density. This plasma layer has a 10 µm exponential density fall-off with 2 µm scale length on either side of it in order to avoid any unphysical effects from the absorbing boundaries. Additional simulation parameters are given in Table 3.5.

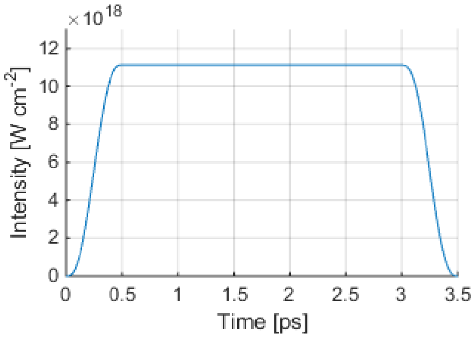

Figure 3.7: Temporal intensity profile for all pulses used in Section 3.4.

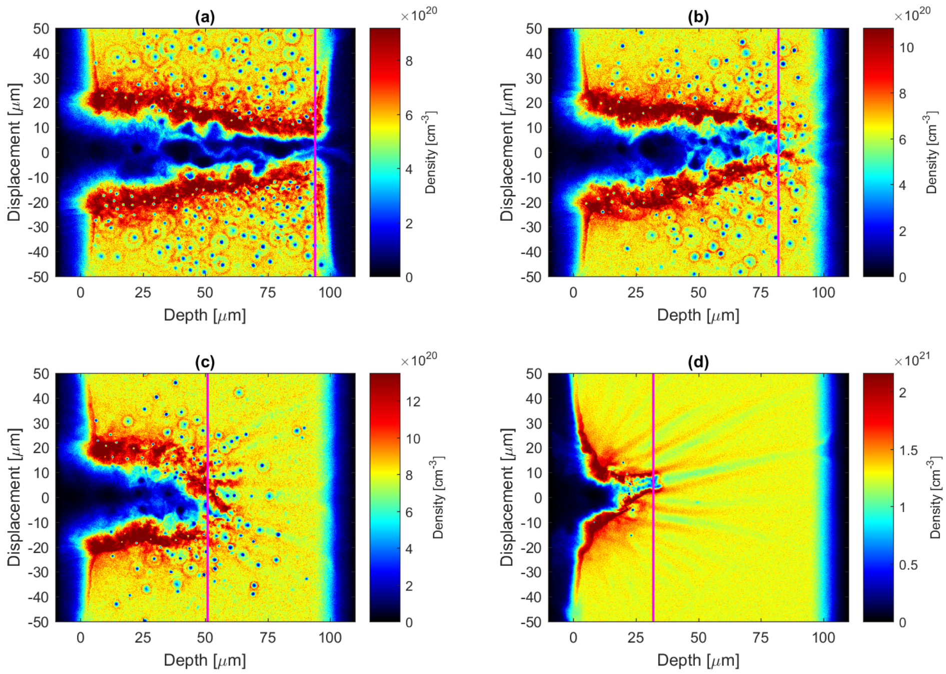

Figure 3.8: The electron density profiles for a 3 ps pulse propagating from the right boundary towards the left through a plasma of density (a) $0.17n_{\gamma c}$, (b) $0.20n_{\gamma c}$, (c) $0.25n_{\gamma c}$, and (d) $0.40n_{\gamma c}$. The magenta vertical lines superimposed on each image indicate the point where the displacement of the channel was measured for each simulation. Channels observed here were formed after 4 ps of simulation time.

Simulation Parameters

λ_0	1.053 µm
Window size	120 µm × 100 µm
PPC	3 × 3
Transverse BC	Periodic

Plasma Parameters

$n_{e0} = n_{i0}$	Constant with buffers
$\lvert q_e/m_e \rvert$	3670 $\lvert q_i/m_i \rvert$
$T_{e0} = T_{i0}$	10 keV

Pulse Parameters

a_0	3
t_{rise}	0.5 ps
t_{flat}	2.5 ps
t_{fall}	0.5 ps
Polarisation	Circular
Focal Position	115 µm
Focal Radius	5.3 µm

Table 3.5: Summary of parameters used in the hosing density dependence simulations.

Density	Grid Size
0.17 $n_{\gamma c}$	3750 × 3150
0.20 $n_{\gamma c}$	4050 × 3400
0.25 $n_{\gamma c}$	4550 × 3800
0.40 $n_{\gamma c}$	5750 × 4800

Table 3.6: Summary of grid sizes for the hosing density dependence simulations. Note that each grid was set so that the resolution matched the Debye length for each simulation.

The density of the plasma layer was varied, and simulations at $0.17n_{\gamma c}$, $0.20n_{\gamma c}$, $0.25n_{\gamma c}$, and $0.40n_{\gamma c}$ were run where $n_{\gamma c} = \gamma n_c$ is the relativistic critical density. The resolution for each simulation was set to match the Debye length of the plasma at 10 keV. See Table 3.6 for a summary of the grids. The results of these simulations are shown in Figure 3.8 after 4 ps of simulation time, giving the pulses enough time to complete their propagation through the plasma and the channels have neared stagnation. As this figure illustrates, the channels in these simulations decrease in depth as the density goes up as one would expect from Equation 2.120.

In order to determine the offset of the channels, transverse line-outs were taken at the points indicated by vertical magenta lines in Figure 3.8. Based on these

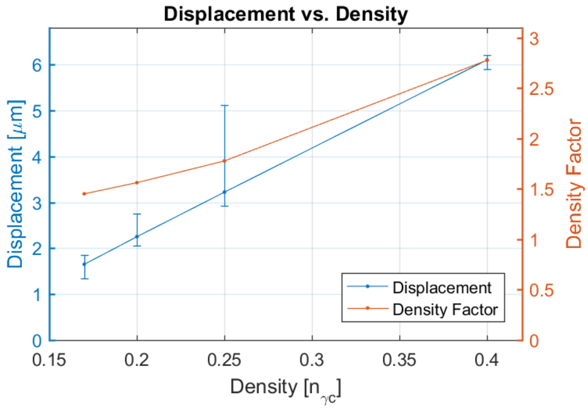

Figure 3.9: Channel displacement versus density. The final magnitude of the displacement of the channels in Figure 3.8 as a function of density is plotted in solid blue. The error measurements were determined by finding the minimum and maximum displacements in a radius of two microns about the lineout point. The orange line represents the density factor $(1 - n/n_{\gamma c})^{-2}$ derived in Equation 3.11. Note that the measurement for the $0.25\,n_{\gamma c}$ simulation has a large upper error bar due to escaped light and soliton formation near the head of the channel.

lineouts, the magnitude of the displacement from the original axis of propagation of the pulse was determined and the results are plotted in Figure 3.9 and compared to the additional density factor of $(1 - n/n_{\gamma c})^{-2}$ that was derived in Equation 3.11.

As can be seen, the displacement of the channels indeed increases as a function of density as predicted by Equation 3.11. However, this displacement increases much more rapidly than the density factor would indicate. This can be attributed to the difference between the phase velocity of the laser pulse and the slower channeling velocity. The transverse acceleration of the pulse is given in the speed of light frame independent from the channeling velocity. As the channeling velocity is lower in higher density plasmas, this will cause the channel to hose at an increased angle. Therefore, $\partial_\psi^2 X_c$ will be greater in higher density simulations and by Equation 3.8, the total displacement will be increased over lower density simulations beyond what the density factor suggests. Further, it is worth noting that the analytical section only predicts the initial behavior of a pulse. Other interactions such as reflection off of the high-density sheath may also affect the total displacement.

Simulation Parameters

λ_0	$1.053\,\mu\text{m}$
Window size	$200\,\mu\text{m} \times 150\,\mu\text{m}$
Grid	$10,000 \times 7500$
PPC	3×3
Transverse BC	Periodic

Plasma Parameters

$n_{e0} = n_{i0}$	$20 n_c \exp[-(\sqrt{x^2 + z^2} - 100\,\mu\text{m})/L]$
$\lvert q_e/m_e \rvert$	$3670\ \lvert q_i/m_i \rvert$
$T_{e0} = T_{i0}$	$10\,\text{keV}$

Pulse Parameters

a_0	20
Polarisation	s-polarised
Focal Position	$115\,\mu\text{m}$
Focal Radius	$5.3\,\mu\text{m}$

Table 3.7: Summary of parameters used in the number of pulses simulations. In the equation governing the initial densities, x is the transverse component, z the longitudinal component, and L the scale length.

3.5 Application - Pulse Number

Previous studies have shown that dividing a channeling pulse into multiple ultra-short subpulses has the potential to greatly improve channel quality [90,91]. However, these studies focused on pulses with durations less than 100 fs which are not easily obtainable on the majority of modern high-energy facilities, most of which rely on neodymium laser technology. In this section, two sets of simulations utilizing the simulation parameters listed in Table 3.7 are compared, one set using a single pulse and the other set using a train of multiple shorter pulses in order to determine if this multiple pulse scheme is applicable to the neodymium-based laser technology. The results will highlight the importance of increased hosing at higher densities shown in the previous sections.

As the physical model shows, the hosing instability increases over the duration of the pulse propagation time through the plasma. Therefore in order to be successful, the individual short pulses which constitute the multiple pulse scheme must have ceased propagation through the plasma before the hosing instability has had time

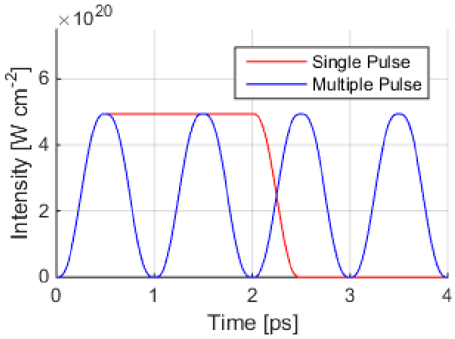

Figure 3.10: Temporal intensity profiles for the single pulse simulation (red) and the multiple pulse simulation (blue).

to significantly alter each pulse's trajectory. Further, in an effort to minimize the channel filamentation, the spot size of the pulse should be kept to a minimum [92], but because of this, relativistic intensities are required in order to remain above the channeling power threshold.

The simulations presented in this section all have pulses propagating from the right of the windows into a radial exponential density profile of scale length L. The simulation window is $200\,\mu\text{m} \times 150\,\mu\text{m}$ with $100\,\mu\text{m} \leq z \leq 300\,\mu\text{m}$ and $-75\,\mu\text{m} \leq x \leq 75\,\mu\text{m}$ where z is the longitudinal coordinate and x the transverse coordinate, so that the maximum initial density in the simulation window is $20n_c$ with a radial fall-off centred $100\,\mu\text{m}$ to the left of the window. The single pulse simulations utilize a pulse with a rise and fall time of 0.5 ps each with a flat peak time of 1.5 ps while, unless otherwise noted, the multiple pulse simulations use four pulses, each with 0.5 ps rise and fall time and a temporal separation between peak intensities of 1.0 ps. This maintains equal energy and peak intensity between simulations. An illustration of these intensity profiles is shown in Figure 3.10.

3.5.1 Proof of Principle

To begin the investigation, the scale length of the density profiles was set to $L = 50\,\mu\text{m}$ in order to allow the pulses to enter a sub-critical plasma. The evolution of a typical single pulse simulation is shown in Figure 3.11. As is evident from this figure, the pulse propagates through the plasma relatively unperturbed until approximately $z = 150\,\mu\text{m}$ where significant hosing begins to occur. However, the pulse then begins to self-correct itself around 1.5 ps into the simulation at which point it is able to continue propagation in its original direction. A more detailed discussion of this behavior is presented in Section 3.7.

In order to compare the differences between simulations, Figure 3.12 shows the overlay of the channel formation from the single pulse and the multiple pulse simulations after 1.5 ps. The data shown was calculated by thresholding the density profiles below 50% of the initial density. Both simulations experience similar levels of hosing, showing virtually no improvement in the multiple pulse simulation over the single pulse simulation. This is due to the multiple pulse scheme's pulses not having a short enough duration. As discussed at the beginning of this section, in order for the multiple pulse method to be effective, the leading pulse should cease channeling before hosing begins. If it does not, trailing pulses will follow the initial channel and begin channeling into the remaining plasma in the direction of the hosing of the first pulse. Looking at Figure 3.11b, it is clear that in order to meet this criterion, the pulse should have stopped channeling before approximately $z = 175\,\mu\text{m}$. Integrating the initial density profile from $z = 175\,\mu\text{m}$ to $300\,\mu\text{m}$ and $x = -15\,\mu\text{m}$ to $15\,\mu\text{m}$ and dividing by the corresponding volume, the average density originally in the channel is approximately $1.6n_c$. Since this is a short-pulse relativistically under-dense simulation similar to the scenario in Reference [74], this value is then substituted in as n along with $d_{\text{ch}} = 125\,\mu\text{m}$ into Equation 2.120. Solving for τ in this equation shows the maximum pulse duration for this initial density profile is approximately 0.37 ps in order to avoid hosing in the initial pulse.

Based on these calculations, an additional simulation was run using the same density profile, but this time employing a series of eight 0.25 ps FWHM Gaussian pulses with a separation between peak intensities of 0.6 ps. This pulse duration is below the capabilities of neodymium-based facilities, but it is interesting to verify the validity the principle behind the multiple pulse scheme nonetheless.

While minor levels of hosing are detectable throughout each pulse's propagation, the amplitude of the hosing never has enough time to significantly effect a redirection of the overall pulse propagation. The electron density for this simulation is shown

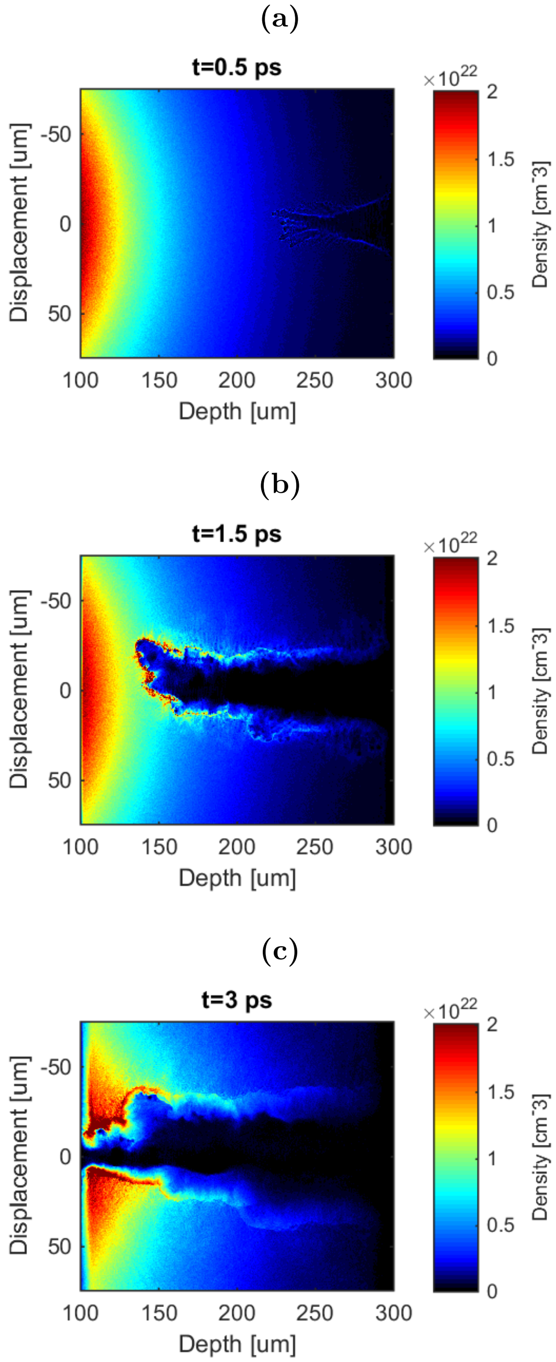

Figure 3.11: Electron density of the single pulse simulations at (a) 0.5 ps, (b) 1.5 ps, and (c) 3.0 ps. Case (b) shows significant hosing in the pulse's propagation. However, this has self-corrected by case (c) due to the high ponderomotive pressure of the incoming relativistic pulse.

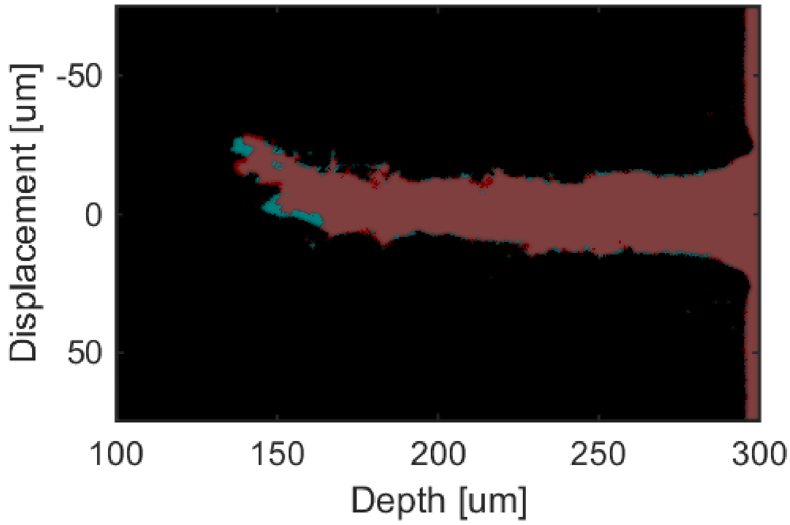

Figure 3.12: Overlay of the single pulse simulation (blue) and the multiple pulse simulation (red) thresholded below 50% of their initial density profiles. The two simulations experienced similar amounts of hosing at this point, thus showing virtually no improvement in the multiple pulse simulation over the single pulse simulation.

in Figure 3.13 after 1.5 ps of propagation time in order to match the timings in Figures 3.11 and 3.12. As can clearly be seen, the hosing present in the previous two simulations has been successfully eliminated through the use of multiple pulses. The channel formation continues in the original direction of propagation through the end of the window, thereby showing the validity of the multiple pulse scheme. However, the density scale length in an inertial confinement fusion implosion are typically on the order of hundreds of microns [1], indicating that additional simulations are required to scale this scheme to full-scale inertial confinement fusion applications.

3.5.2 Scale Lengths

In order to better determine the feasibility of the multiple pulse scheme in more realistic scenarios, four additional simulations were carried out using the single 2.0 ps pulse and four 0.5 ps pulses as discussed at the beginning of this section. Each of these pulse configurations was directed into plasmas with scale lengths of $L = 100\,\mu\text{m}$ and $200\,\mu\text{m}$. The increased scale lengths would cause the pulses to propagate through plasmas of higher density, thereby lowering their individual channel depths as predicted by Equations 2.119 and 2.120, thus making it easier for

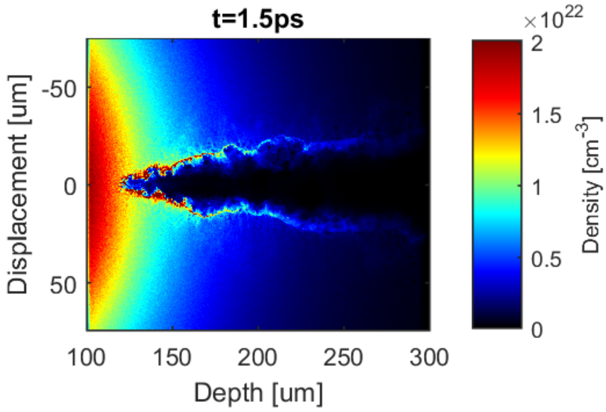

Figure 3.13: Electron density of the 0.25 ps pulse simulation at 1.5 ps into the simulation. The resulting channel is significantly straighter than the results presented in Figures 3.11 and 3.12.

them to deplete before hosing occurs. However, as shown in Sections 3.3 and 3.4, the levels of hosing should increase as well, thus introducing a competing effect.

In both of these density profiles, the performance of the multiple pulse scheme declined as the scale length increased. Figure 3.14 shows the resulting density profiles for the single pulse and multiple pulse configurations in the 200 µm scale length density profile at various times, approximately matching the hole-boring depths. As is shown qualitatively, the single pulse channel experiences small amounts of hosing at various times along its propagation but is able to quickly self-correct itself before any significant displacement is achieved. The multiple pulse scenario on the other hand does experience severe hosing around $z = 220\,\mu\text{m}$.

The poor performance of the multiple pulse scheme is due to the decreasing intensity at the tail of the pulse. The relativistically induced transparency is reduced as the pulse continues to lower in intensity, thus increasing $n/n_{\gamma c}$, and thereby greatly increasing the effects of hosing as predicted by Equation 3.8. Eventually this leads to the plasma being over-critical, preventing further propagation. This accounts for the sharp bend in the channel in Figure 3.14d. Indeed, each case of strong hosing in these multiple pulse simulations corresponded with the end of a short pulse. Therefore, while the multiple pulse scheme could be useful below critical density or with pulses with extremely short rise and fall times, it is not well-suited

(a) Single pulse, $d_{\mathrm{hb}} \approx 50\,\mu\mathrm{m}$

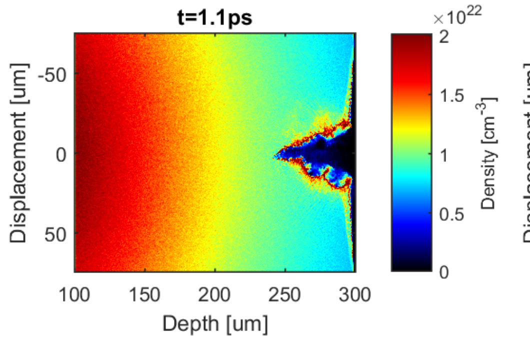

(b) Multiple pulse, $d_{\mathrm{hb}} \approx 50\,\mu\mathrm{m}$

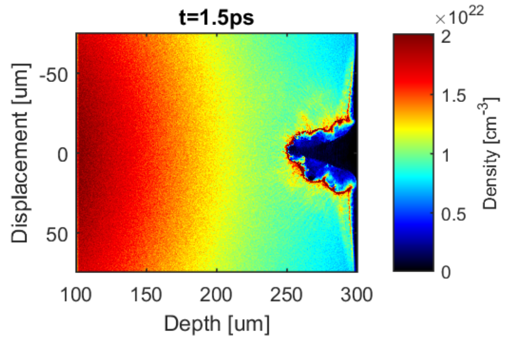

(c) Single pulse, $d_{\mathrm{hb}} \approx 100\,\mu\mathrm{m}$

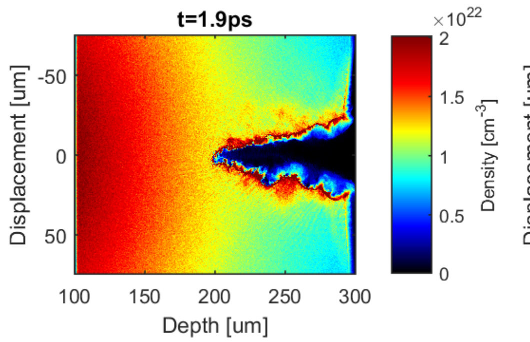

(d) Multiple pulse, $d_{\mathrm{hb}} \approx 100\,\mu\mathrm{m}$

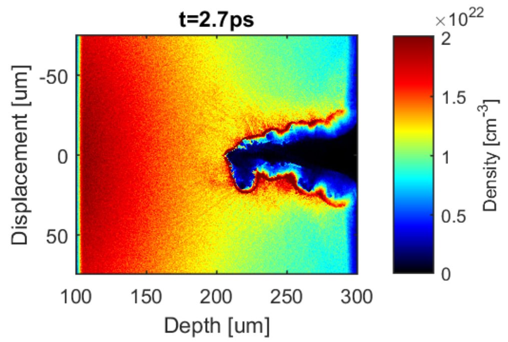

(e) Single pulse, final formation

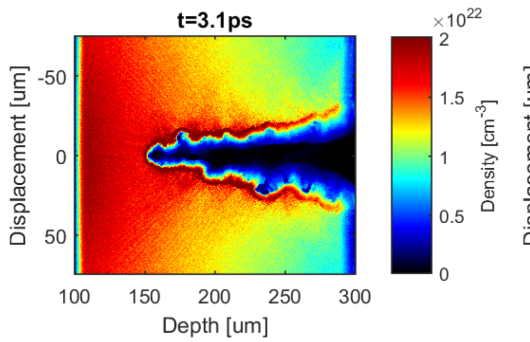

(f) Multiple pulse, final formation

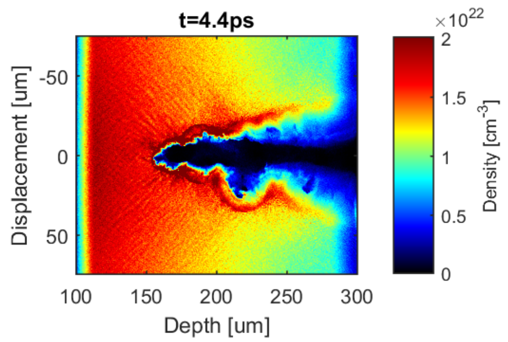

Figure 3.14: The electron density profiles for the single pulse (left) and multiple pulse (right) simulations using a density scale length of 200 µm. The various times and propagation distances are given in each subcaption.

for propagation in relativistically transparent plasmas due to the increased levels of hosing present at higher relativistically adjusted densities.

3.5.3 Geometry Dependence

As a final note on this set of simulations, in addition to investigating the number of subdivided pulses and plasma scale length, it is important to analyse the effects of the initial density profile on the hosing instability. One would expect a more planar density profile around the critical density in a larger-scale experiment as much more matter is ablated causing the critical density to be reached at a much greater radius from the target centre, while smaller-scale experiments would experience a much more radially dependent density profile. Therefore, an additional simulation was run in a planar exponential density profile which otherwise matches the parameters of the single pulse simulation with $L = 50\,\mu\text{m}$. The new density profile in this run is given as $n = 20n_c \exp(-z/L)$ where x is again the transverse component and z the longitudinal component. This density profile is identical to the profiles used above but without the transverse component dependence.

The temporal evolution of this simulation is shown in Figure 3.15. After 1.5 ps, it appears as though some hosing did occur around halfway through the simulation window. However, this is the result of the initial filamentation of the beam as it came into focus and is not a change in the main pulse's trajectory. A more detailed discussion of this focal filamentation is presented in Section 3.6. This is further exemplified as the density in that region is not near vacuum at this time. After propagating past this filamentation point, the pulse underwent self-focusing and propagated forward into the plasma. By the time the pulse reached the left edge of the simulation box, there is virtually no displacement of the centroid, showing that beyond the initial filamentation, there was no significant hosing apparent in this simulation.

An improvement over the radial density profile simulations matches expectations. Should a pulse be displaced slightly from its original vertical positioning in this planar exponential profile, it would still see an approximately symmetrical density profile

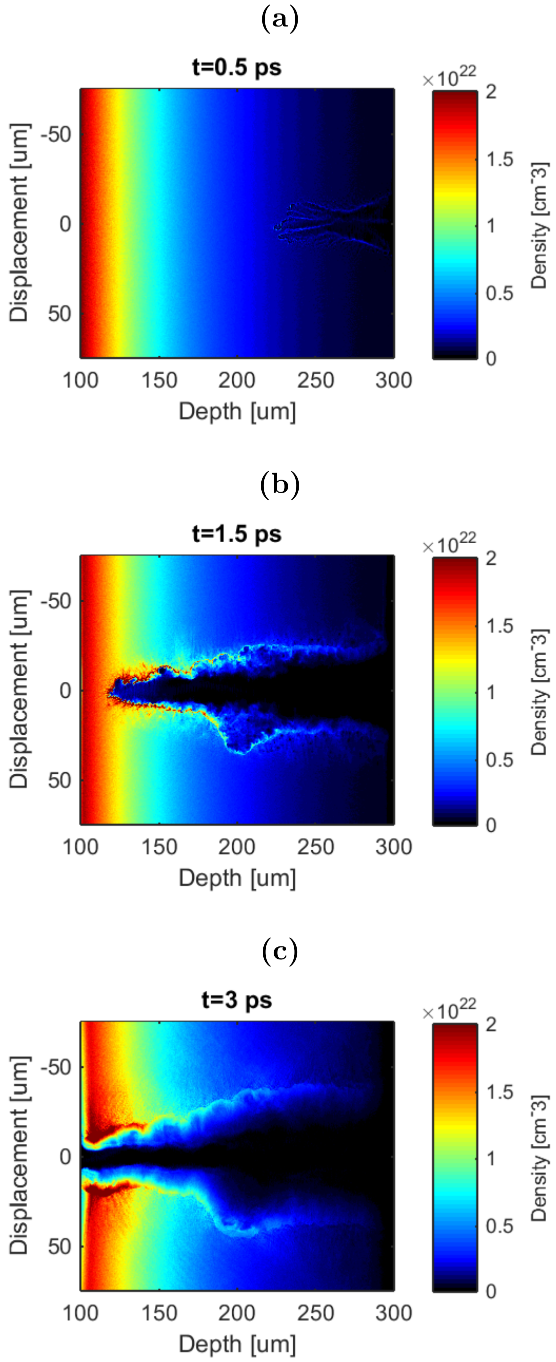

Figure 3.15: Electron density of the planar density profile simulation at (a) 0.5 ps, (b) 1.5 ps, and (c) 3.0 ps. There is virtually no hosing through the entire evolution of the simulation, thereby showing less hosing in planar density profiles than in radial density profiles.

about its centroid. However, the radial density gradient in previous subsections introduced a transverse density asymmetry to a pulse displaced from its original position. Should a pulse in the radial profile be displaced, the side closest to its original path would see a higher average density than the far side, resulting in a phase velocity gradient where the outer edge has a lower phase velocity than the inner edge, thereby leading to significant refraction and hosing away from the window centre. This implies that in experiments with lower driver energy, one could expect to see more hosing since the density profile will have much greater curvature than in higher energy experiments.

3.6 External Perturbations

Highly relativistic pulses are beneficial for a variety of reasons. Recent studies show that they allow a magnetic field to be seeded in front of the channel which can subsequently be used to collimate fast electron beams generated by trailing pulses [34]. Additionally, they are able to penetrate deeper into the plasma due to relativistically induced transparency. This increased transparency has an added potential to minimize the effects of external density perturbations in a turbulent plasma by reducing their effect on a pulse's phase velocity. Continuing the theme of this chapter, the increased intensity also leads to increased hosing, thereby introducing a competing effect. A set of simulations were run to examine these effects. It should be noted that the results presented in this thesis on this topic are preliminary in nature and the author is continuing his investigation with a wider range of simulations.

Table 3.8 summarizes the simulation parameters. A p-polarised pulse entered a $400\,\mu\text{m}\times150\,\mu\text{m}$ window into an exponentially increasing plasma with a $200\,\mu\text{m}$ scale length. The plasma's density in the centre of the window was half of the non-relativistically adjusted critical density. A Gaussian perturbation was introduced with a full width at half maximum of $41.6\,\mu\text{m}$ centred at $z = 200\,\mu\text{m}$, $x = 25\,\mu\text{m}$ where z and x are the typical longitudinal and transverse directions. The pulse

Simulation Parameters

λ_0	1 µm
Window size	400 µm × 150 µm
Grid	20,000 × 7500
PPC	3 × 3
Transverse BC	Periodic

Plasma Parameters

$n_{e0}/n_c = n_{i0}/n_c$	$0.5\exp(z/200\,\mu\text{m} - 1) +$ $0.25\exp(-[(z-200\,\mu\text{m})^2 + (x-25\,\mu\text{m})^2]/[25\,\mu\text{m}]^2)$
$\lvert q_e/m_e\rvert$	$4590\ \lvert q_i/m_i\rvert$
$T_{e0} = T_{i0}$	5 keV

Pulse Parameters

t_{rise}	0.25 ps
t_{flat}	Continuous
Polarisation	p-polarised
Focal Position	200 µm
Focal Radius	15 µm

Table 3.8: Summary of parameters used in the external perturbation simulations. After t_{rise}, the pulses remained at their maximum intensity throughout the duration of the simulation (5 ps).

had a 0.25 ps rise time, after which it remained at its maximum intensity. This intensity was varied between $a_0 = 1$, $a_0 = 3$, and $a_0 = 30$.

The results of these simulations are shown in Figure 3.16. Unfortunately, due to the short duration and limited number of simulations, it is difficult to make any conclusions comparing the performance of the various intensities. As is evident, the $a_0 = 30$ simulation did manage to largely ignore the presence of the external perturbation. Due to the strong ponderomotive forces, a high density sheath quickly formed about the channel. The densities of this sheath exceeded the maximum perturbation density. As a result, channel formation continued largely as if the perturbation were not present, explaining the filament branching upwards during interaction with the perturbation. Overall, there was only a slight total deflection with the pulse exiting at about $x = -18\,\mu\text{m}$ which corresponds to a deflection from the centre of the window of approximately 5°.

The lower intensity pulses did not have enough time to propagate throughout

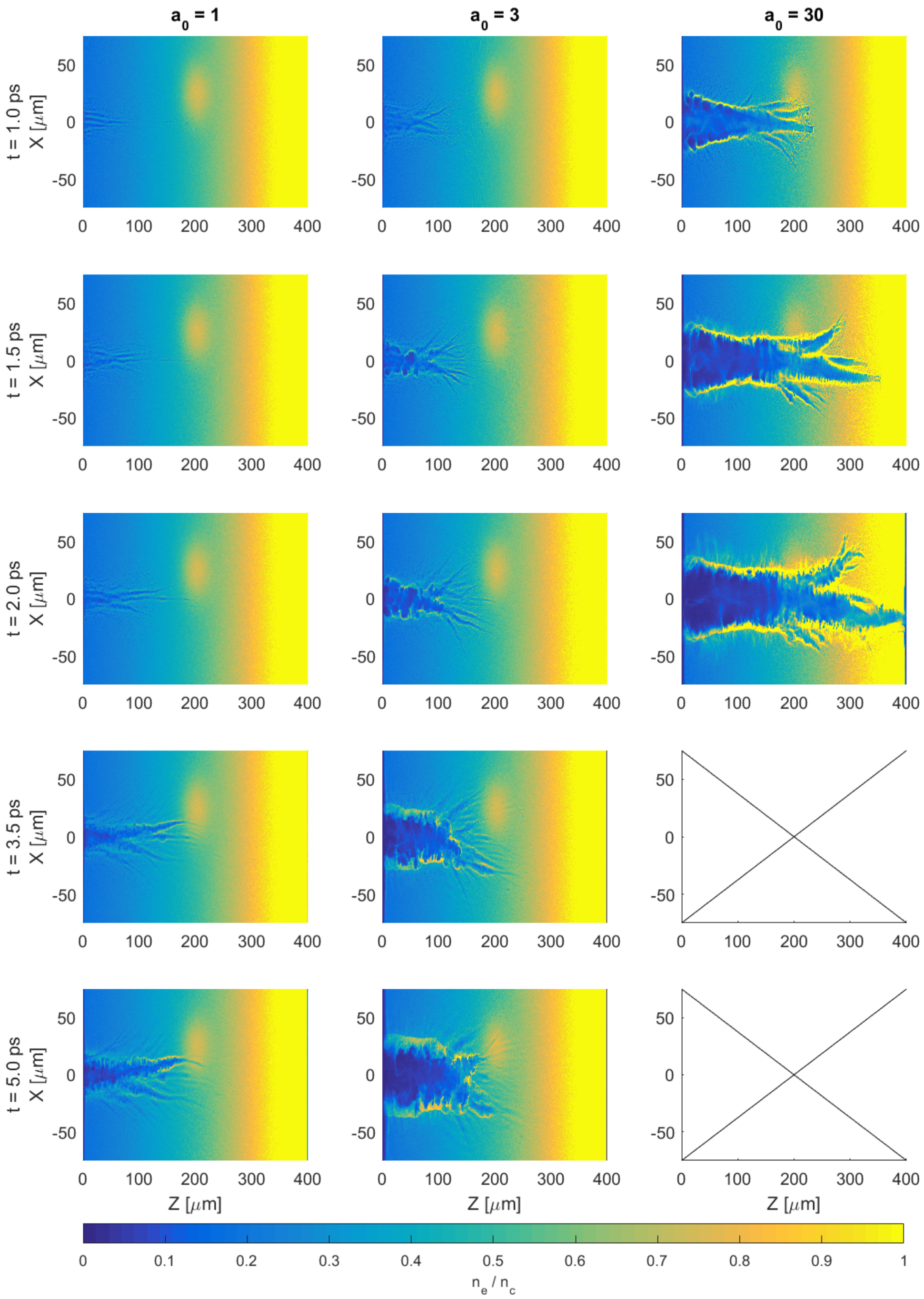

Figure 3.16: Electron density profiles of external perturbation simulations. Pulses entered the window from the left and traveled in the z direction. The columns and rows are labeled with their corresponding intensities and times respectively.

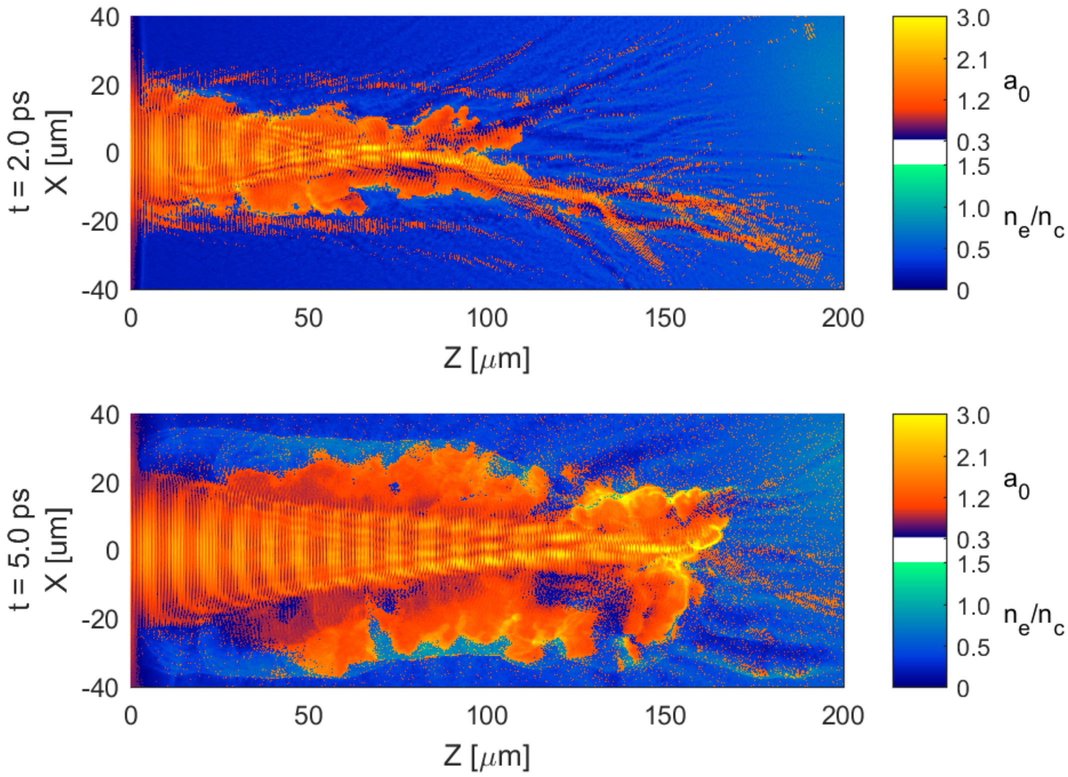

Figure 3.17: Pulse intensity and electron density overlay of the $a_0 = 3$ external perturbation simulation after 2 ps and 5 ps. Intensity modulations appear within the pulse intensity profile which leads to filamentation. Note that only the interaction region is shown.

the entire window, barely reaching the perturbation by the end of the simulations. Already though, strong filamentation is present in both. Along with the previously discussed causes of filamentation, another explanation reveals itself when analysing the total electromagnetic energy visualizations such as that shown in Figure 3.17. A planar pulse perfectly focused off of a parabolic mirror will not experience destructive interference with itself. However, strong intensity modulations are seen in the electromagnetic energy plots. Following the evolution of the channel along with the electromagnetic profile, these intensity modulations often branch into their own filaments following the standard physical picture described in Section 2.7.4. This is due to the self-focusing of the pulse. A parabolic mirror comes to a perfect focus because the path length of any ray is identical, thereby providing perfect constructive interference. When self-focusing occurs, this is no longer true. Further,

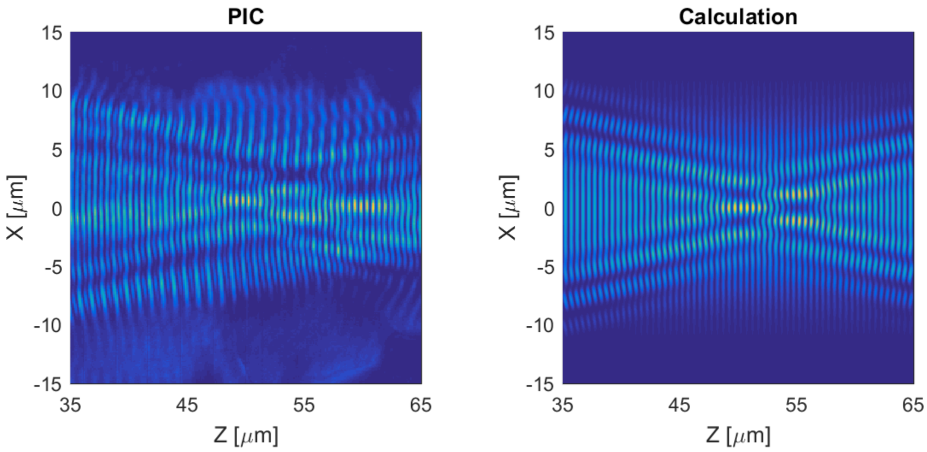

Figure 3.18: Modeling of the interference caused by self-focusing. A cropped image of the electromagnetic energy for the $a_0 = 3$ simulation after 2 ps is shown on the left. On the right is the calculation of three interacting Gaussian beams. The results are qualitatively similar and suggest self-focusing leads to filamentation.

it is evident that at later times when the plasma has been sufficiently expelled from the early channel, the pulse no longer self-focuses and the modulations only appear deeper into the channel where self-focusing is present.

To further illustrate that these modulations are the results of pulse interference rather than density modulations, the interaction of three Gaussian beams was calculated. The two outside beams had a standard deviation width of 2 µm and a third of the maximum field strength of the 6 µm wide central beam. They intersect the central beam at 25°. Figure 3.18 shows the result of this calculation compared to a subsection of the $a_0 = 3$ simulation after 2 ps. As can be seen, the field structure is qualitatively similar, lending additional support to the idea of self-focusing leading to filamentation.

Work is currently underway to form a more quantitative measurement of the effects of self-focusing including windowed Fourier analysis and analytical examination. As stated in the introduction to this subsection, additional simulation work is also planned to continue this investigation following these promising preliminary results. Most immediately, two additional simulations are planned for $a_0 = 10$ and $a_0 = 22$, though limited computational resources prevent the author from conducting this set of simulations immediately, and the lower intensity pulses are planned to be simulated for 10 ps rather than 5 ps. These simulations will reveal more about the competing nature between the hosing instability's and relativistically induced transparency's effects on external perturbations. Additionally, another series of simulations is planned to vary the structure of the perturbation.

3.7 Additional Observations

Throughout the simulations in this chapter, after a pulse initially underwent hosing, it was able to quickly correct itself. This is a result of the extremely high ponderomotive pressure of highly relativistic pulses which initially seeds a forward-facing channel by nearly immediately evacuating the electrons in front of it. An example of this is visible in Figures 3.11(b)-(c). If the channel wall in front of the pulse is overdense, as has been the case with several of the simulations found in this chapter, then this process is similar to the momentum flux transfer from photons to ions described in the derivation of the overdense hole-boring velocity, Equation 2.115, the only difference being the angle of reflection. After creating the initial "dent" in the channel wall, the rest of the pulse is able to focus further since once in this dent, the plasma density is locally symmetric and the pulse is able to proceed in its original propagation direction. As a result, by the time the pulse reaches the rear of the simulation in Figure 3.11c, it has fully self-corrected and the displacement is no longer discernible.

This behavior will be more evident at higher intensities even if the initial density profile as a function of $n/n_{\gamma c}$ is kept constant between scenarios. To see this, note from Equation 2.115 that the overdense hole-boring velocity which drives this process can be written $v_{\mathrm{hb}} \propto a_0/\sqrt{n/n_c} \propto \sqrt{a_0/(n/n_{\gamma c})}$ when $a_0 \gg 1$. Therefore, higher intensity pulses are expected to self-correct faster than their lower intensity counterparts, and by doing so, a smaller fraction of the total pulse energy will have gone into the creation of these branching filaments. Thus, high intensity pulses are able to give additional control of the channel, and the additional energy cost of using high intensity pulses [28] is partially mitigated by the speed of the self-correction.

In addition to ponderomotive self-correction, several simulations presented here displayed a common phenomenon which shall herein be referred to as the "pathfinder" pulse. As the pulses entered the simulation window, the front of the pulse separated from the bulk of the beam after approximately a plasma wavelength. This suggests that these separations likely occurred due to the self-phase modulation instability [86]. The index of refraction was modified as the pulse intensity increased and plasma waves formed, leading to photon acceleration [84, 93]. This change to the pulse frequency led to a modulation in the group velocity which then caused the energy to bunch longitudinally [86]. While the majority of the pulse continued forward between the hole-boring and channeling velocities, this pathfinder pulse propagated at the group velocity of the plasma while maintaining a structure similar to a wakefield [94, 95]. The intensity was sufficiently high to modulate the density, and in s-polarisation, it would occasionally form a soliton in front of the channel.

Especially clear examples of this are seen in the intensity ramp simulations, most notably Set 2, shown in Figure 3.2 for times $t \leq 3.0\,\mathrm{ps}$. As shown here, soliton-like bubbles form in front of the channel. By tracking the electromagnetic energy, it is clear that these come from the pathfinder pulse. Density modulations can also be seen in p-polarisation, such as in the external perturbations simulations for $a_0 = 1$ and $t \leq 1.5\,\mathrm{ps}$, shown in Figure 3.16.

Figure 3.19 shows cropped images of the electromagnetic energy from the $a_0 = 3$ external perturbations simulations as the pathfinder pulse separates from the bulk of the pulse. In every time step, the window advances at the group velocity of the plasma at the centre of the window. The left column shows the raw data while the right column shows the data with a $1\,\mu\mathrm{m}$ Gaussian blur in order to remove the high-frequency signal and to allow the envelope of the pulse to be examined. Superimposed on the right column are dotted magenta lines. These lines are separated by the plasma wavelength at the centre of the window. As can be seen, the pulse separates from the bulk of the beam and continues to evolve, focusing and separating into multiple spots which are approximately the size of the plasma wavelength. This occurred again primarily through relativistic self-phase modulation.

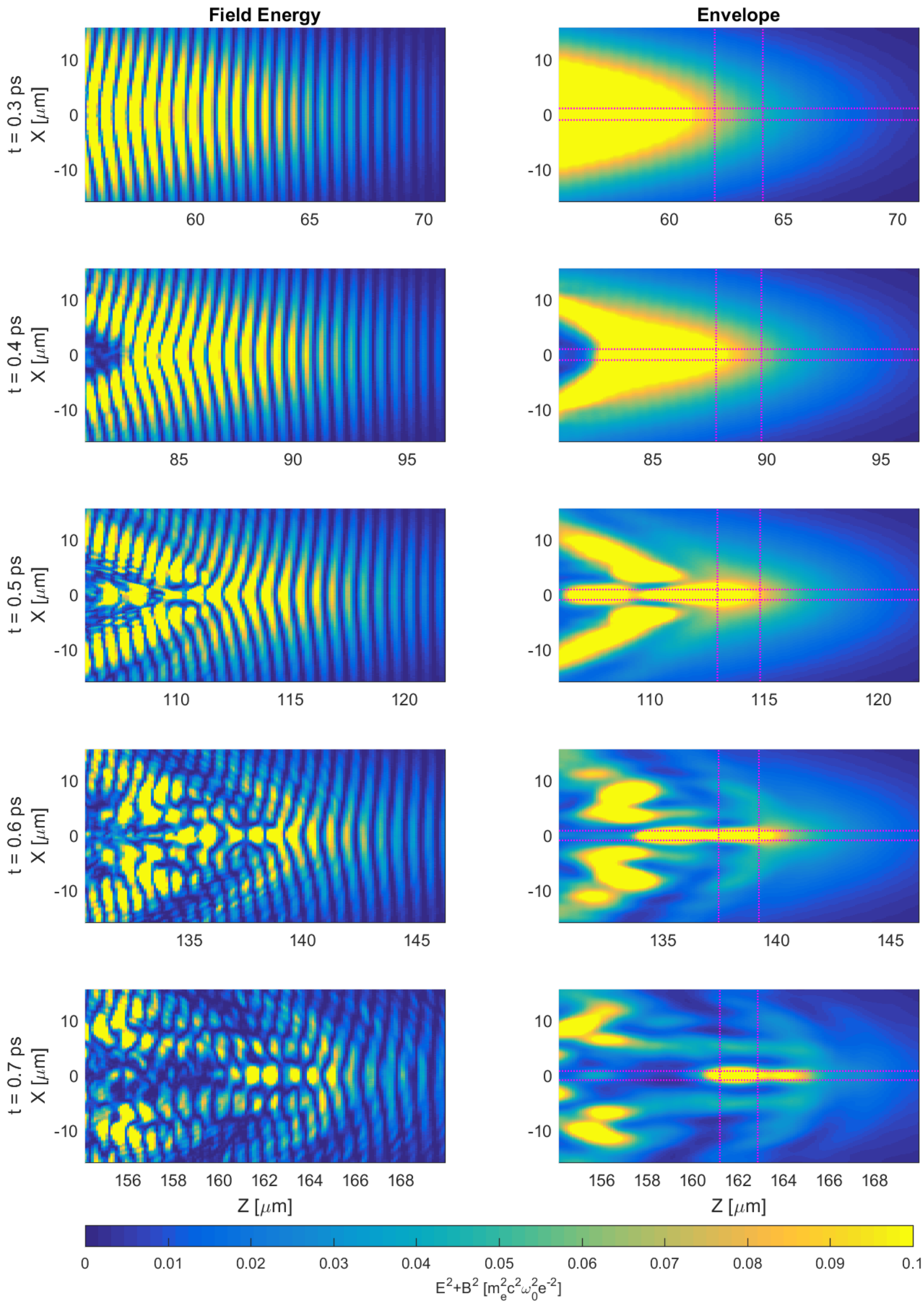

Figure 3.19: Evolution of the pathfinder pulse. Plotted is the electromagnetic energy from the $a_0 = 3$ external perturbation simulations at various time steps. The left column shows the raw data while the right column shows the pulse's envelope by applying a 1 µm Gaussian blur. The dotted magenta lines in the right column form a box and are separated in each direction by the plasma wavelength at the centre of the window.

The increased intensity and density compared to laser wakefields allows the pathfinder pulse to begin channeling, though it never fully expels the plasma from its path outside of soliton formation. This implies that these pulses could be useful to guide a more intense channeling beam by creating a relatively unperturbed, reduced density path. Indeed, in Set 2 of the intensity ramp simulations, the use of three low-intensity beams, each of which had its own pathfinder pulse, did appear to guide the high-intensity beams quite well, though it is difficult to state with certainty due to the limited number of simulations in that investigation. However, the pathfinder pulses still refract which, if significant in magnitude, leads to their breakup. This can be observed in the external perturbation simulations after the pulse passes $z = 200\,\mu\text{m}$. Refraction occurred with varying magnitudes depending on the transverse position of an energy bunch in the pathfinder beam due to the shape of the perturbation. This quickly caused the beamlets to diverge.

Additional work is required to investigate these pathfinder pulses further. An interesting application would be to combine a Ti:sapphire laser, capable of delivering high-intensity, femtosecond pulses, with a neodymium based laser system, providing the bulk of the total energy over picosecond durations. Both of these systems are discussed in greater detail in Chapter 4. The Ti:sapphire laser would generate a train of $\sim 10\,\text{fs}$ pulses to act as the pathfinder beams. They would then swiftly be followed by the main channeling beam from the neodymium-based system. Thus the simulations will focus on a train of ultrashort pulses with wavelengths of 800 nm followed by a channeling beam of wavelength 1053 nm.

3.8 Simulation Validation

The simulations in Section 3.5 utilized cell sizes of approximately three times the Debye length and density profiles that increased towards the absorbing walls of the simulation window. As a result, it is necessary to check for any unphysical effects that could be caused by artificial heating or edge effects. To accomplish this, additional simulations were run using identical profiles to the radial density profiles in Section 3.5.

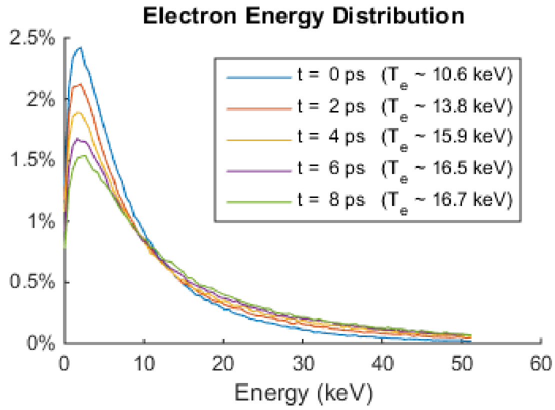

Figure 3.20: The energy spectrum of the plasmas used in Section 3.5 with no lasers incident. Significant artificial heating can be seen over the length of the simulation.

To check for artificial heating, a simulation was run matching the radial density profile simulations in Section 3.5 but with no laser pulses incident on the plasma. The energy of the particles was binned and the tail of the energy spectrum was fit by the Boltzmann distribution in order to determine the heating of the plasma. The results are shown in Figure 3.20. As can be seen, significant heating of the plasma was observed in the absense of a laser pulse, and so a convergence test was run.

The spatial grid of the single pulse simulation in Section 3.5 was set to $20,000 \times 15,000$ cells in order to halve the cell size and check for any effects from the observed artificial heating. The results of this simulation are shown in Figure 3.21. While the results of these two simulations do not exactly match, similar features are seen in both, particularly the initial hosing of the pulse away from the high-density region and the ponderomotive self-correction. Due to the stochastic nature of the hosing instability, a change in the absolute shape of the channel is to be expected. Therefore it was determined that the simulations used in previous section were sufficient to illustrate the effects of pulse number and geometry on the hosing instability.

Additionally, as part of the original investigation, simulations were also run at intensities corresponding $a_0 = 3$ with the simulation window starting from $z = 192.2$ in order to reach the same relativistic critical maximum as the $a_0 = 20$ cases. The ponderomotive self-correction was still present at this intensity, though a greater percentage of the pulse's energy was diverted into the hosing channel. Since this

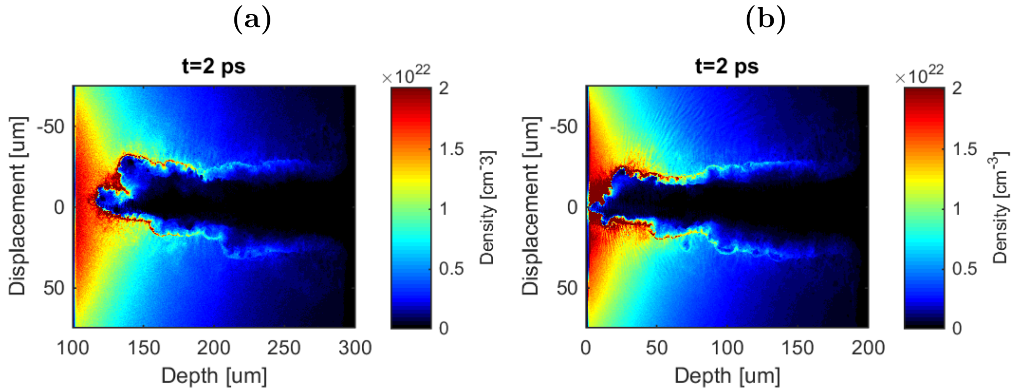

Figure 3.21: Convergence test of the single pulse simulation in Section 3.5. The electron density profile is shown after 2 ps of simulation time in (a) the original simulation presented in Section 3.5 and (b) the identical simulation run with double resolution.

simulation still exhibited the same features discussed in Section 3.5, the artificial heating will have no strong impact on the analysis presented above.

In order to test for these artificial effects, an additional $a_0 = 3$ simulation was run with an added 10 µm, 2 µm scale length exponential decrease in density added behind the previous absorbing edge. The resulting electron density profiles of these simulations is shown in Figure 3.22. Here again, while the absolute shapes of the channels differ, this is to be expected, and the major features of hosing away from high-density regions and ponderomotive self-correction are still present.

Therefore, since both artificial heating and edge effects do not greatly alter the simulations presented above, the results of these simulations are valid. This is determined qualitatively as there is no exact measurement of channel quality. However, various methods may be invented to this end. For instance, the channel depths may be determined simply by taking the maximal location of density suppression below a thresholding value (i.e. the deepest point where the electron density fell below 0.1 n_c).

Determining the extent of filamentation and general channel quality is a far more complex task. Since a straight channel without filamentation would have minimal surface area, one could imagine a measurement of the channel's surface area would be an adequate approach. The density profile of a channel could again be thresholded below a certain value, thus setting the region defined as a channel

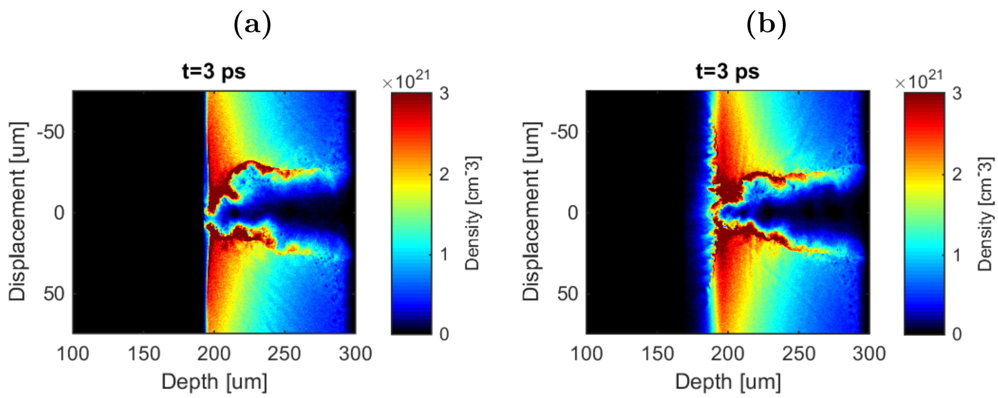

Figure 3.22: Edge effects test of the $a_0 = 3$ single pulse simulations. The electron density profiles are shown (a) with an absorbing edge at $z = 192.2$ and (b) with an exponential downramp starting at $z = 192.2$.

to one and elsewhere to zero. To find the channel walls, one would simply need to run a two-dimensional gradient operator on the thresholded image and take the absolute value of the results to create a wall detection image. Summing the pixel values of this image would then give a measurement of the channel's surface area. However, this method would require blurring of the original image in order to reduce noise and would be highly dependent upon the random variations from simulation to simulation. As such, a large set of data would be required in order to produce statistically meaningful results, and because of this, such an analysis has not been performed here.

One final factor which could affect the outcomes of simulations is the random number generator's seed. Random number generators are only pseudo-random, which means that they can not be reasonably predicted and appear random, yet they are still deterministic. If given the same seed value, the random number generator in OSIRIS will produce the same sequence of pseudo-random numbers, thus allowing simulations to be rerun with identical results. Changing this seed value will change the string of random numbers used in initialising and processing the simulations, thereby showing the effects of random fluctuations. The previous simulations in this chapter all used the default value in OSIRIS of 0.

As seen in the other examinations in this section, hosing and filamentation are stochastic processes which will vary depending on the initial distribution of

Simulation Parameters

λ_0	1 µm
Window size	800 µm × 300 µm
Grid	20,000 × 7500
PPC	3 × 3
Transverse BC	Periodic

Plasma Parameters

$n_{e0} = n_{i0}$	$0.1 \exp(z/430\,\mu\text{m})\ n_c$
$\lvert q_e/m_e \rvert$	$4590\ \lvert q_i/m_i \rvert$
$T_{e0} = T_{i0}$	5 keV

Pulse Parameters

a_0	2.7017
t_{rise}	80 fs
t_{flat}	Continuous
Polarisation	p-polarised
Focal Position	200 µm
Focal Radius	16 µm

Table 3.9: Summary of parameters used in the random seed simulations.

the plasma. Thus, varying the seed of the random number generator may have an effect on the channel's development. Three large-scale simulations were run in OSIRIS version r555m of a 10^{19} W cm^{-2} pulse entering an inhomogeneous plasma with a 430 µm scale length. The simulations were identical with the exception of the random seed which was set equal to 1, 10, and 100. The rest of the simulation parameters are summarized in Table 3.9 and the results are shown in Figure 3.23.

As can be seen in this figure, seeds 1 and 10 produced qualitatively similar results. Self-focusing led to filamentation at focus which in turn led to the large bifurcation and approximately the same point along z. Each filament was offset from the initial path, causing large amounts of refraction which led to additional filaments forming at $z > 250$ µm. However, the seed 100 simulation did not have this focal filamentation, and as a result, the channel largely avoided bifurcation of any kind. Thus, measuring the levels of filamentation in simulations requires multiple runs to ensure that actual physical mechanisms are responsible for any improvement of the channel as opposed to blind luck. Because two of the pulses

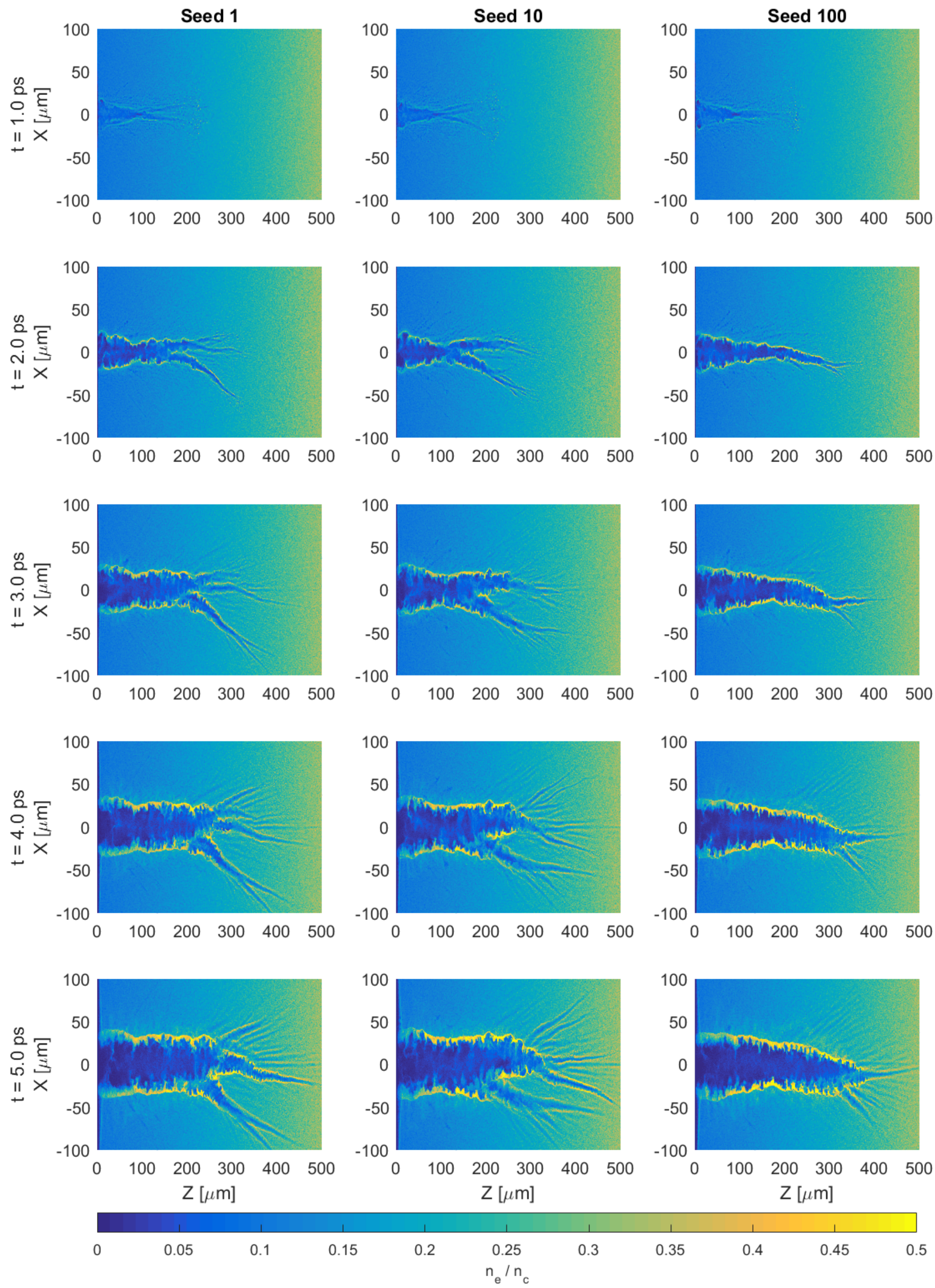

Figure 3.23: Electron density profiles of the random seed simulations.

experienced filamentation, it is not possible to get a quantitative comparison of the hosing of the pulses as initially intended. Nevertheless, the vast majority of the trends identified in this chapter – the density and intensity dependence of the hosing instability, the validity of the multiple pulse scheme, the ponderomotive self-correction – were all consistent across a range of simulations and thus are stated with confidence to be valid.

4
Laser Facilities and Diagnostics

Before proceeding on to the design and results of various channeling experiments, it is worth understanding the basic principles behind laser technology and the accompanying diagnostics used during these experiments. Knowing the capabilities and limitations of each system is crucial in experimental design, and of course, no technology should be used as a black box without a basic understanding of the underlying mechanisms. Thus, this chapter will focus on a brief overview of the laser amplification methods, facility capabilities, and diagnostics used throughout the remainder of this thesis.

4.1 Principles of Lasers

The word "laser" is itself an acronym for "light amplification by stimulated emission of radiation", a rather self-descriptive term. As photons pass through matter, there are three fundamental interactions between the radiation and the atoms: absorption, spontaneous emission, and stimulated emission. Collisional excitation and de-excitation may be added for completeness, though they are not necessary to understand the basic workings of a laser system. It is the balancing of these terms which leads to optical gain and beam production. Thus the basics of any such system may be thought of in three steps. First, the seed photons must be created via the laser oscillator. Then these photons must pass through an optical gain material, amplifying the intensity of the beam. Finally, the pulse is transmitted to a target area where it will be focused down onto a target. This section will explore the generation processes and the underlying physics in each based on the arguments presented by Hooker and Webb [96].

4.1.1 Amplification

As stated above, there are three fundamental interactions between photons and atoms. Consider a basic system where only two energy levels are accessible by the electrons in an atom, the lower state, denoted with subscripts 1, and the upper state, denoted with subscripts 2. The absorption of a photon with energy matching the difference in these levels, $E_{21} \equiv \hbar\omega_{21}$, allows an electron to go from the lower state to the upper state. Eventually this electron will decay back to its lower state by emitting a photon of the matching energy. Alternatively, stimulated emission may occur where another photon will cause the electron to return to the lower state, releasing a matching photon in the same direction in the process.

Given the number densities, N_1 and N_2, of these states and the photon energy density, $\varrho(\omega_{21})$, one may make assumptions about the rates at which these interactions occur. Spontaneous emission occurs regardless of the presence of photons and should thus only depend on the number of particles in the upper state. Absorption and spontaneous emission both require the presence of photons of the correct energy, and thus will be proportional to the photon energy density at the corresponding frequency and the number densities of the lower and upper states respectively. Let A_{21} represent the constant of proportionality for spontaneous emission, B_{21} for stimulated emission, and B_{12} for absorption. Assuming the system is in thermodynamic equilibrium, the radiation rate losses must be matched by the radiation rate gains. This is known as the Principle of Detailed Balance. Mathematically, this may be written as [96]:

$$B_{12}N_1\varrho(\omega_{21}) = A_{21}N_2 + B_{21}N_2\varrho(\omega_{21}) \tag{4.1}$$

The energy density of radiation in thermal equilibrium is known as blackbody radiation and is given by:

$$\varrho_B(\omega) = \frac{\hbar\omega^3}{\pi^2 c^3} \frac{1}{e^{\hbar\omega/k_B T} - 1} \tag{4.2}$$

This equation may be derived by multiplying the density of radiation modes by the number of photons per mode and again by the energy of each photon in that mode, though the details of this have been omitted for brevity.

Finally, given that the system is in thermodynamic equilibrium, the ratio of the number densities follows the Boltzmann law:

$$\frac{N_2}{N_1} = \frac{g_2}{g_1} e^{-\hbar\omega_{21}/k_B T} \tag{4.3}$$

where g_1 and g_2 are the degeneracies of the lower and upper states respectively. This now forms a system of three equations with three unknowns. Solving for the constants of proportionality yields the Einstein relations:

$$\begin{aligned} A_{21} &= \frac{\hbar\omega_{21}^3}{\pi^2 c^3} B_{21} \\ g_1 B_{12} &= g_2 B_{21} \end{aligned} \tag{4.4}$$

These constants of proportionality are postulated to hold under all conditions. Therefore, even though these equations were derived assuming thermodynamic equilibrium, they should hold regardless of the distribution of states and for any radiation field.

In order for optical gain to occur, the rate of stimulated emission must exceed the rate of absorption. From Equation 4.4, this requires:

$$\frac{N_2}{g_2} > \frac{N_1}{g_1} \tag{4.5}$$

Thus, a population inversion must occur where more electrons per degenerate mode are in the upper state than the lower state. This is generally accomplished through the use of flash lamps which briefly excite the lasing medium into a population inversion before the main seed pulse passes through. The net effect is a transfer of energy from the undirected lamps into the directed beam. Often, the lasing material is cylindrical, so the flash lamp and the laser rod will be placed at the foci of an elliptical reflecting chamber in order to maximize the energy sent from the flash lamp to the rod. Other configurations exist which rely on similar principles. A disadvantage of flash lamps is their wide frequency range. In order to increase the efficiency of the system, diode lasers tuned to the appropriate frequency may be used to pump the lasing material instead.

In this analysis, the energy levels were assumed to be sharp. In reality, absorption may occur at a range of photon energies due to a variety of broadening mechanisms which will affect the rate constants. The details of these broadening mechanisms have little bearing on the content of this thesis, though they include phenomena such as natural, collisional, and Doppler broadening. It should be noted that the maximum transition rate still occurs at the central frequency. As a result, as a seed pulse propagates through a lasing medium, the central frequency is amplified more than the surrounding frequencies and the bandwidth will be reduced. This process is known as gain narrowing.

One final process that should be understood in light amplification is gain saturation. As amplification continues, the intensity of the seed pulse will grow exponentially. However, this growth clearly cannot be sustained indefinitely without violating the conservation of energy. As the intensity of the pulse increases, so too do the number of photons which cause electron transitions to occur. Eventually, these transitions will affect the population inversion ratio, N_2/N_1 by causing a significant portion of the upper level electrons to transition down to the lower state, thereby weakening the amplification potential of the medium.

4.1.2 Pulse Generation

The previous subsection described the amplification of a seed beam as it passes through a lasing medium. It did not, however, go into the generation of the seed beam itself. Consider a long cylinder of lasing material. Spontaneous emission will occur throughout the material, emitting radiation in all directions. For emissions at one end of the cylinder, only a small fraction, $\Omega/4\pi$ where Ω is the solid angle subtended by the far end of the cylinder, will actually experience any significant gain. This type of laser is known as an amplified spontaneous emission (ASE) laser [96].

To combat these losses, the lasing material may be surrounded by reflecting walls so that light which would have otherwise escaped will instead remain within the material to continue amplification. Thus, in order for light to be amplified, the only requirement is that the gain from the material must exceed the losses from the imperfect reflection. These so-called optical cavities may then be chosen to allow only a few modes of light to exist. Concave mirrors are often chosen for this purpose and are generally only placed on one axis with the remaining four sides of the box left open. There will still be losses to the sides, but light at small angles to the laser axis will remain trapped with few transverse modes. Further, the use of concave lenses may reverse the effects of diffraction as the light continues to oscillate through the material.

The design of these laser cavities varies depending on their usage. The focal spots of the mirrors may be positioned differently to achieve various types of output. For instance, placing the focal spots well outside of the cavity produces a near-planar arrangement. This is not very useful for continuous wave lasers as the number of reflections would require extremely precise alignment. However, short pulse lasers often utilize this configuration as fewer round trips of the cavity are required. Alternatively, a near-hemispherical alignment can be used where the focal spot of one mirror is placed just beyond a planar mirror. This is a highly tunable configuration which may have a theoretically arbitrarily-sized focal spot by adjusting the separation of the mirrors while allowing simple alignment through the translation of the curved mirror. Several other configurations are possible but are unnecessary for understanding the basic workings of a laser facility.

Finally, dynamic effects must be considered in order to determine how to release a pulse from an optical cavity. To allow the state inversion to build, one of the mirrors will be blocked, thereby disrupting the cavity's amplifying effects and preventing amplified spontaneous emission from occurring. When a proper amount of inversion has been achieved, the mirror will be unblocked, thus allowing optical gain to take place. Today this is done largely with the use of Pockels cells and polarisers. A Pockels cell is essentially a waveplate whose birefringence varies based on the strength of an applied electric field. For instance, a Pockels cell may be placed in front of a mirror and oriented with an axis at 45° to a polariser placed in front of the cell. Light will pass through the polariser and become linearly polarised in a known plane. Without loss of generality, it is safe to assume that this polarisation is in the vertical direction. While the voltage is on, the Pockels cell will act as a quarter-wave plate (see Section 4.3.2) and converts linear light into circular light. After reflection, the light will pass again through the Pockels cell and be converted into horizontal linear polarised light which will then be fully blocked by the polariser. When the voltage to the Pockels cell is shut off, the birefringence is removed, and the light is able to reflect back through the system with low loss.

4.1.3 Lasing Materials

There is a wide range of materials which may be used to amplify a pulse. Choosing two energy levels within the atoms to use as an amplification material relies on a variety of factors. For instance, Nd^{3+} ions are well suited to lasing due to the low intensities required to reach their operational thresholds and the decoupling of their excited modes and phonon frequencies. One common configuration is Nd:YAG. Nd:YAG crystals are formed by doping a YAG crystal ($Y_3Al_5O_{12}$) with neodymium so that the Nd^{3+} ion replaces the Y^{3+} ion. The increased size of the Nd^{3+} ion compared to the Y^{3+} ion places a maximum doping concentration in order to avoid altering the crystal structure. The most common transition used within this material produces a wavelength of approximately 1064 nm. However, this is not the only application of Nd^{3+} ions for lasing, and the surrounding material may greatly alter its behavior. They may also be used as dopants in glass made of a range of materials which will alter the transition wavelength between 1054 nm and 1062 nm. The gain cross-section of Nd:glass is much lower than that of Nd:YAG. Because of this, it is often chosen for large energy laser facilities as large population inversions may be achieved without much self emission amplification occurring, thus allowing better contrast levels than Nd:YAG. However, because the glass has low thermal conductivity, shot rates are greatly reduced.

Finally, the laser with the largest bandwidth is the Ti:sapphire laser. This is a crystal of Al_2O_3 with titanium ions substituting aluminium ions. Because the titanium ion has only a single d-shell electron, it has a very simple energy-level structure. This structure yields a wide bandwidth with wavelengths tunable from 660 nm to 1180 nm. Despite the wide bandwidth, the optical gain cross-section is still comparable to that of Nd:YAG. These crystals are not typically able to achieve high energy pulses, but are able to have very high repetition rates and short pulse durations. To do so requires a technique known as Kerr modelocking. Modelocking is the process of fixing the phases of each longitudinal mode within the laser cavity, though the details of this process will not be elucidated here. This technique restricts the tuning range to 780–820 nm, but it is able to produce pulses with durations as short as 35 fs.

The amount of energy a system is capable of generating in a pulse is dependent upon the amplification material's damage threshold. As a result, neodymium-based systems are able to generate much more energetic pulses than a Ti:sapphire laser. There has been great effort in exploring how to mitigate these limits in order to deliver more intense beams. The current state-of-the-art technology to this end is chirped-pulse amplification [97]. In this scheme, a short pulse is reflected off of a diffraction grating which will spread the pulse out spectrally due to its bandwidth. This results in the pulse being separated in time by having the low-frequency components travel a shorter distance than the high-frequency components. While in this stretched form, the pulse's intensity is greatly reduced, thus allowing it to be amplified to a greater extent than would be possible without this stretching technique. Diffraction gratings may then be used again to recompress the pulse back to its original duration. Nearly all of the greatest power laser facilities in the world use this technology today.

4.2 Laser Facilities

Several experiments were conducted throughout the course of research for this thesis at a variety of laser facilities throughout the world. However, only those at OMEGA and OMEGA EP are presented in the following chapter in order to form a cohesive narrative for this thesis. As such, the capabilities for only these two facilities are outlined here.

4.2.1 OMEGA - Laboratory for Laser Energetics

The OMEGA laser system is part of the Laboratory for Laser Energetics (LLE), a branch of the University of Rochester located in Rochester, NY in the United States of America. This system is comprised of 60 Nd:glass beams which may be focused onto a single target. As such, it was specifically designed to investigate direct-drive inertial confinement fusion. Each of the 60 beams are able to deliver 500 J of energy in a 1 ns square pulse at 351 nm wavelengths, thus delivering a total of up to 30 kJ to a single target.

4.2.2 OMEGA EP - Laboratory for Laser Energetics

OMEGA EP (extended performance) is, as its name would suggest, an extension to the OMEGA system at LLE. It provides short-pulse capabilities to experiments at this facility, either by sending these petawatt beams to an independent target area or by running joint shots with the OMEGA 60 system. This allows various high-intensity subjects to be investigated, including fast ignition, x-ray radiography and proton radiography. The OMEGA EP system consists of four beamlines. Two of these are able to operate with pulse durations between 1 and 100 ps at 1053 nm. However, maximum energy of 2.6 kJ may only be achieved for pulses with durations at least 10 ps. Below this, the maximum energy lowers down to 1 kJ. This may be focused within a 10 µm spot radius, defined as the radius which contains 80% of the pulse energy, yielding averaged intensities on the order of $2 \times 10^{20}\,\mathrm{W\,cm^{-2}}$. It should be noted that speckling of the laser pulse, will cause some regions to contain much greater intensities than this value while others remain significantly lower. All four beamlines are also capable of long-pulses with durations in the 1 to 10 ns range. Because these pulses are generated using the same techniques as the OMEGA system, they also have a wavelength of 351 nm. The energy of these beams ranges from 2.5 kJ over 1 ns to 6.5 kJ over 10 ns.

4.3 Diagnostics

A basic summary of several diagnostics used in the remainder of thesis is presented in this section. This description is only focused on describing the most basic physics behind each diagnostic with a more complete analysis being provided later in this thesis with experimental data.

4.3.1 Shadowgraphy

Perhaps the simplest diagnostic using a probe beam is shadowgraphy [98]. This technique involves propagating a low intensity beam through a plasma which will then undergo refraction from phase velocity perturbations. The beam must be of low intensity in order to avoid altering the plasma's profile significantly. After the interaction, this beam may then be magnified and captured on a CCD camera. The resulting image will be bright where the beam did not undergo significant levels of refraction and dark where refraction did occur. Generally, these perturbations will be caused by density fluctuations, thus creating "shadows" where the density profile is rapidly changing transversely to the probe. In the main experiment of the following chapter, shadowgraphy was used to qualitatively observe the shape of a channel generated by a short pulse propagating through an inhomogeneous plasma. These shadows then appeared at the walls of the channels where the density gradient was steepest.

4.3.2 Polarisation Dependent Materials

It is possible for a material's refractive index to vary depending upon the polarisation of light passing through it. Often, this is due to the crystal structure of a material. One simple example of this is a polariser which may allow only one polarisation of light to pass through. A slightly more complicated example is a birefringent crystal which has a different index of refraction for ordinary and extraordinary polarisations. This property lends itself to several applications in experiments, ranging from controlling a pulse's polarisation to diagnosing magnetic fields.

Waveplates are a natural use of birefringent materials. Similar to the Cotton-Mouton effect described in Section 2.4.4, the polarisation dependence of the refractive index will lead to a change in the ellipticity of a pulse. As the pulses continue to propagate, a relative phase difference, $\Delta\delta$, will arise between the polarisations.

Suppose a pulse with wavelength λ_0 enters a birefringent material of length L and difference in refractive indexes of $\Delta\eta$. Phase velocity is given as $v_\phi = c/\eta$, so the total relative phase imparted upon the beam is given as

$$\Delta\delta = 2\pi \frac{L}{\lambda_0} \Delta\eta \tag{4.6}$$

Thus the length of the material may be varied to adjust the relative phase. In a quarter-wave plate, $\Delta\delta = \pi/2$, and the pulse will go from linear polarisation to circular and vice versa. Similarly, half-wave plates set $\Delta\delta = \pi$ so that linear light with polarisation at an angle of θ to the plate's axis will be rotated by 2θ and elliptical light's handedness will be inverted.

One final birefringent optic that is worth commenting on is a Wollaston prism. This is formed by combining two birefringent crystals with their axes perpendicular to one another. Without loss of generality, let the index of refraction for s-polarised light in the first crystal be given by η_1 and in the p-plane by η_2 with $\eta_1 > \eta_2$. Then s-polarised light will go across a surface at 45° from η_1 to η_2 while p-polarised light will cross from η_2 to η_1. This leads to a splitting of the light to separate the s- from the p-polarisations.

4.3.3 Polarimetry

One common use for a Wollaston prism is polarimetry. Assume that a linearly polarised probe beam is aligned with a Wollaston prism so that its polarisation is at a $\theta_0 = 45°$ angle to the prism's axis. This light may be described as an equal combination of s- and p-polarised light. As a result, it would then split evenly after passing through the Wollaston prism in vacuum. The output then would be collected by a lens and sent to a CCD camera to measure the results.

However, if the beam passes through a plasma containing persistent magnetic fields parallel to the probe's propagation direction, those fields will induce Faraday rotation as described in Section 2.4.3. By using the index of refraction given in Equation 2.48 and integrating the infinitesimal version of Equation 4.6, the total rotation is found to be

$$\Delta\theta = \frac{e}{2m_e c}\int_{-\infty}^{\infty} \frac{n_e}{n_c}\mathbf{B}\cdot \mathrm{d}\mathbf{l} \tag{4.7}$$

where d**l** is the infinitesimal path of the pulse. The pulse will now be polarised at an angle $\theta = \theta_0 + \Delta\theta$ to the prism's axis, and thus it will not split evenly. One image will have intensity $P = I_0 \sin^2\theta$ while the other has intensity $S = I_0\cos^2\theta$ where I_0 is the total intensity. Then

$$\begin{aligned} \frac{P-S}{P+S} &= \sin^2\theta - \cos^2\theta \\ &= -\cos(\pi/2 + 2\Delta\theta) \\ &= \sin(2\Delta\theta) \end{aligned} \tag{4.8}$$

Thus a useful measure of the magnetic field in a plasma given its intensity profile may be found by subtraction and normalization of the images. As discussed in Chapter 2, strong left-hand azimuthal magnetic fields form in a channel. When a pulse filaments into multiple channels, each of these channels should then display similar azimuthal magnetic fields. With this in mind, polarimetry was utilized in the following chapter to attempt to image the filaments of the channeling pulse.

4.3.4 Angular Filter Refractometry

Angular filter refractometry is a diagnostic for determining a plasma's density profile which was recently developed by Haberberger *et al.* for the OMEGA and OMEGA EP laser systems [45]. While other techniques such as interferometry, schlieren imaging, and shadowgraphy can be used to such an end [98], they either do not

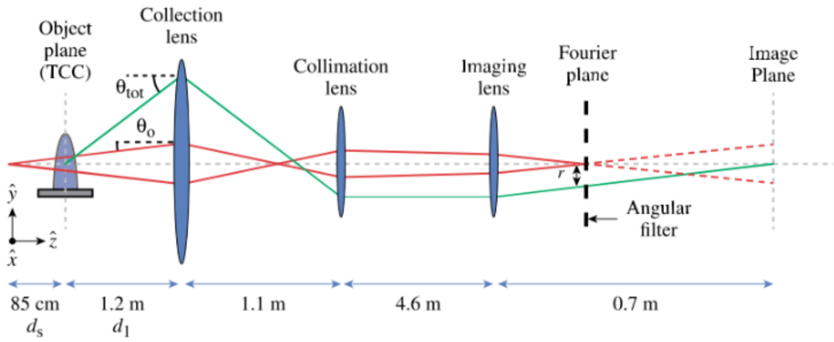

Figure 4.1: Schematic of an AFR diagnostic. Rays from the unrefracted probe are shown in red. A refracted ray is shown in green. The lens system is designed to focus the probe beam to the centre of the angular filter placed in the Fourier plane. However, refraction causes a translation in this focal plane, thereby linking the edges of the shadows from the filter to known refraction angles. These are observed using a CCD camera in the image plane. Image taken from Haberberger *et al.* [45].

produce reliable quantitative results or are limited to low density plasmas due to diagnostic resolutions and are not well-suited for densities in excess of $10^{20}\,\mathrm{cm}^{-3}$ [45].

Angular filter refractometry (AFR) overcomes these limitations by applying contour lines for fixed refraction angles to a probe beam. These lines then allow the user to spatially determine the phase of the probe, and by doing so, determine the overall density profile. To achieve this, a probe beam passes through the interaction region to be analysed which has generally been formed through the ablation of a planar target. It is then collected and refocused. An angular filter, that is, a series of concentric circles alternating between transparent and opaque, is placed in the focal plane. As illustrated in Figure 4.1, refraction from the interaction region will cause a ray to be translated a distance r in the focal plane, thus coupling the edges of the filter's rings to known levels of refraction. This results in shadows in the image plane which are observed using a CCD camera.

The AFR diagnostic is calibrated so that the refraction angles corresponding to each opaque ring edge is known. Analysis of the output images then involves four steps which are illustrated in Figure 4.2. First, the shadows' edges are identified in the images through a manual trace. The refraction angles are then mapped onto these positions and interpolated between the edges. These angles may then be converted to the spatially resolved total phase accumulation of the probe beam. Finally, this

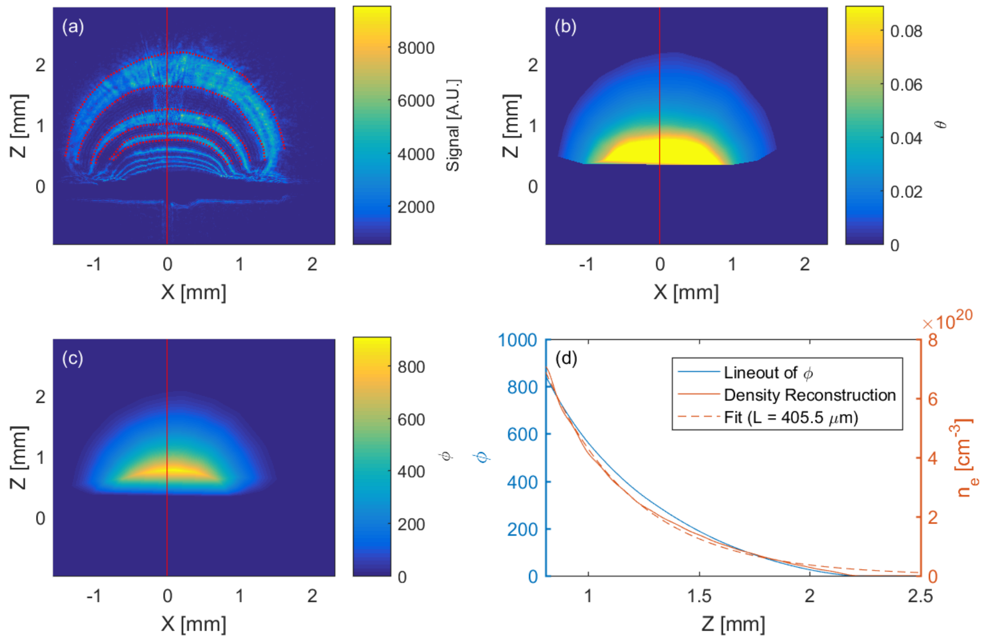

Figure 4.2: Example AFR reconstruction. The initial image was taken from the experiment discussed in Chapter 5. The raw image retrieved from the AFR diagnostic is shown in (a) and overlaid with the traced edge locations in dotted red. Note that the perturbations in the centre of the image were caused by a separate channeling beam and have been ignored in this trace. The refraction angles are then interpolated (b) and the total phase accumulation is calculated (c). Finally, the Abel inversion of the lineout indicated by the solid vertical lines in (a)-(c) is shown in (d) along with an exponential fit.

.

phase accumulation can be related to the density by assuming that the density profile is symmetric about the axis normal to the target and performing an Abel inversion.

Note that the phase of the pulse rays may be determined by observing that the phase is related to the refraction angle according to $\nabla\phi = k_p\theta$ where ϕ is the phase, k_p is the wavenumber of the probe, and θ is the refraction angle at any given point. Assuming that no phase is accumulated at the window boundaries, this forms a mathematical problem known as the Eikonal equation which is solvable using an algorithm known as the multi-stencil fast marching method. Applying this algorithm will then provide the desired results.

This method of reconstruction has been tested and proven to be quite robust, producing approximately 15% error throughout. However, only a finite number of rings are visible and refraction is only measurable to the outermost rings. Thus,

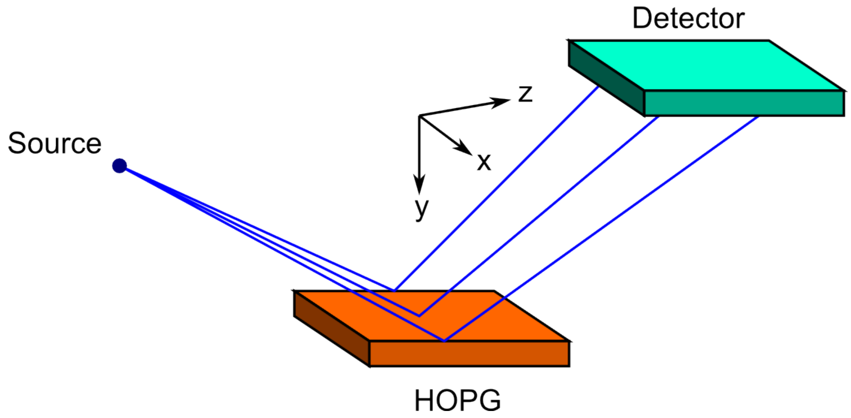

Figure 4.3: Schematic of a HOPG spectrometer. Light from a source Bragg reflects off of a HOPG crystal and is captured by a detector such as an image plate.

the density beyond the outermost ring may not be determined. As a result, an absolute error equal to the reconstructed density at this point is added.

In the next chapter, the main experiment's plasma was generated by ablating a flat target using an energetic ns-scale pulse. While this was modeled using FLASH simulations, and the formation may be roughly predicted using the equations in Section 2.6, it was necessary to directly observe the resulting inhomogeneous profile. This was done utilizing the AFR diagnostic.

4.3.5 HOPG and von Hamos Spectrometers

Consider a beam of fast electrons propagating through a layer of solid copper. As these electrons pass through the copper, they will eject inner-shell electrons from the copper atoms. Electrons from higher shells will then transition down to these vacancies and emit a photon of the corresponding transition energy. The most prevalent transition is from $n = 2$ to $n = 1$ where n (in this section only) is the principal quantum number. This radiation is known as K_α. Other transitions will appear as well, such as $n = 3$ to $n = 1$, otherwise known as K_β emissions, though they will generally not appear as brightly. The emission spectra of copper have been well-studied [99–102] with K_α peaks occurring at approximately 8.05 keV and K_β at around 8.90 eV.

Since the photon energy of these transitions are well-known, a spectrometer may be designed which relies on Bragg reflection. Highly oriented pyrolytic graphite

(HOPG) is a synthetic crystal often used for this purpose. It is made of micron-scale crystallites which have only very slight variance in their orientation. This dramatically increases the reflectivity of the HOPG compared to an ideal crystal, thus making it well suited to experiments [103]. The simplest such Bragg spectrometer consists of light from the source entering a slit and reflecting off of an angled HOPG. The crystal is angled so that wavelengths about the K_α emission line would be Bragg reflected. The reflected light is then collected by a detector such as an image plate.

Let $\hat{z}$ be the axis connecting the source to the detector, $\hat{x}$ the axis perpendicular to the plane formed by the source, crystal, and detector, and $\hat{y}$ the remaining orthonormal axis. A schematic of this is shown in Figure 4.3. Then the spectrum seen by the detector will be spread in the z-direction according to Bragg's law, and the centred energy is controlled by translating the HOPG in the y-direction. Further, if the source is spatially broad, in order to achieve adequate resolution, the light from the source must pass through a slit before reaching the HOPG which is narrow in the y-direction. However, this will greatly limit the light seen by the detector, so the slit must then be wide in the x-direction. As illustrated in this figure, the light reflecting off of the HOPG will be divergent, again decreasing the signal to the detector. In a von Hamos spectrometer, the HOPG is curved about the z-axis in order to focus the signal from the source, thereby greatly improving the signal-to-noise ratio compared to a planar HOPG spectrometer [104].

A von Hamos spectrometer was utilized in the next chapter's main experiment to observe K_α emission from a copper lining on the back of the main target. This K_α emission was largely generated by fast electrons collisionally expelling bound electrons from the copper atoms. Thus, it proved to be a useful diagnostic in characterising the fast electrons' characteristics as they passed through the copper region.

5
Experiments: Channel Optimization

Throughout the course of study for this thesis, the author participated in several experiments to examine a range of topics, including target-normal sheath acceleration of ions [105, 106], plasma wakefield acceleration of electrons [107–111], the implementation of 4ω polarimetry [112], and of course, channeling. This chapter presents an analysis of the experiment which is most relevant to this thesis.

A channeling experiment was performed at the OMEGA EP facility focused on establishing the optimum parameters for channeling in large scale length plasmas. Several factors had to be taken into account in choosing which parameters to explore. For instance, if a fast ignition experiment were to have a long coast phase, that is, a long time between the end of the drive pulses and stagnation, the plasma would cool significantly. However, this cooling would cause thermal filamentation to increase due to an increase in collisionality within the plasma as discussed in Section 2.7.4. Further, waiting gives the plasma more time to expand, creating a larger density scale length which could affect propagation. Thus the relative timing of the drive beam and the channeling beam was chosen to be the first parameter to be scanned.

Further, the whole-beam self-focusing (super-penetration) approach to channeling presents a method of achieving deeper channeling through relativistic transparency while minimizing filamentation [92, 113]. To do so, the laser pulse must be focused at low densities in order to allow relativistic self-focusing to reduce

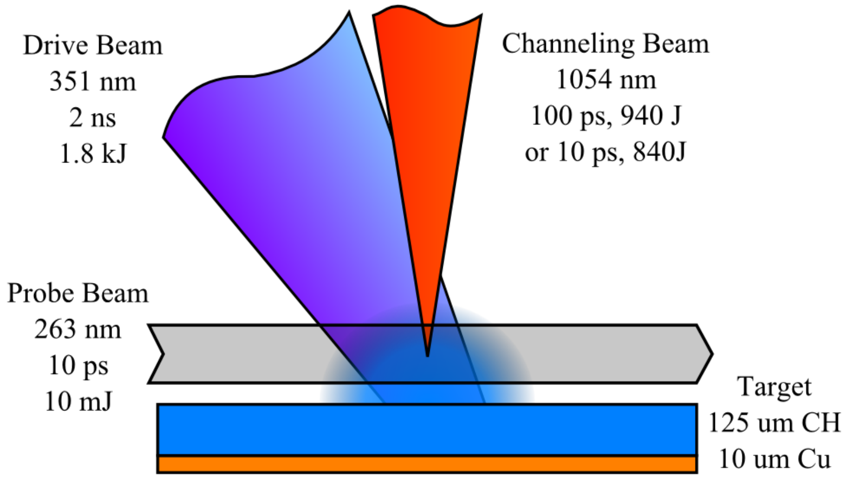

Figure 5.1: Schematic of experimental setup. A 3ω drive beam ablates the surface of a plastic target, generating a plasma plume. Upon completion of the driving phase, a 1ω channeling pulse begins propagation through the plasma normal to the target's surface. A 4ω probe pulse is used to observe the resulting channel formations.

the spot size before the pulse reaches the quarter critical density isosurface [90]. While the original papers on this process did contain experimental results and show great promise, those experiments were performed with a much smaller scale length than is obtainable at the OMEGA EP facility. Thus, in order to test the feasibility of the scheme on large scale length plasmas, this experiment's second varied parameter was the focal position of pulses.

Finally, while higher intensity pulses theoretically would be able to penetrate deeper into a plasma due to relativistically induced transparency [114], previous numerical work has illustrated that this is not an energy efficient process as excessive levels of kinetic energy are transferred to the electron species [28]. Thus the intensity of pulses with similar total energies needed to be explored and became the third and final parameter to be varied in this experiment.

5.1 Experimental Design

The experiment design was as follows and is illustrated in Figure 5.1. An ultraviolet (UV) square pulse drive beam of 1.8 kJ energy and 2 ns duration with wavelength $\lambda_{\mathrm{UV}} = 351\,\mathrm{nm}$ irradiated a copper-backed polystyrene target. The CH layer was 125 µm thick with 10 µm Cu backing for use as a diagnostic for hot electron generation via Cu K_α imaging. Upon completion of the drive pulse, a channeling beam was targeted at the resulting plasma plume along its density gradient using an f/2 off-axis parabola. This infrared (IR), $\lambda_{\mathrm{IR}} = 1.054\,\mu\mathrm{m}$, pulse had a Gaussian longitudinal profile and alternated energy and duration between approximately 940 J over 100 ps and 840 J over 10 ps. The vacuum focal spots for these shots were inferred and on average contained 80% of the laser energy in an 18 µm radius for the 100 ps shots and a 15 µm radius for the 10 ps shots. These equate to averaged intensities and corresponding dimensionless vector potentials of approximately $9.0 \times 10^{17}\,\mathrm{W\,cm^{-2}}$ ($a_0 \approx 0.85$) and $1.2 \times 10^{19}\,\mathrm{W\,cm^{-2}}$ ($a_0 \approx 3.1$) respectively. Thus the 100 ps pulse will be referred to as the low-intensity beam and the 10 ps pulse the high-intensity beam. Finally, the resulting channels were diagnosed primarily through the use of a 10 ps, 10 mJ, 4ω probe beam ($\lambda_{\mathrm{probe}} = 263\,\mathrm{nm}$) passing transversely through the channeling beam's propagation axis. The polarisation of the beams was determined by their compressors. As a result, the 10 ps beams were s-polarised and the 100 ps beams were p-polarised relative to the transverse probe.

Fixing time $t_0 = 0\,\mathrm{ps}$, the shot timings were as follows: The UV drive pulse began interacting with the target at either time $t_{\mathrm{hot}} = -2.0\,\mathrm{ns}$, herein known as the 'hot' shots, or at time $t_{\mathrm{cold}} = -3.5\,\mathrm{ns}$, the 'cold' shots. The low-intensity pulse was injected into the plasma so that its peak was delivered at $t_{\mathrm{low}} = 0\,\mathrm{ps}$ while the high-intensity pulse's peak was injected at time $t_{\mathrm{high}} = 40\,\mathrm{ps}$. This was done so that both pulses would complete their propagation at approximately the same time. The probe peak timing was set to $t_{\mathrm{probe}} = 60\,\mathrm{ps}$ in order to align with the end of each channeling pulse's propagation.

Simulations were performed by a member of the research group, Shu Zhang of the University of California, San Diego, using the radiation-hydrodynamics code, FLASH, to give the predicted density and temperature profiles used to identify the focal positions of the IR pulse. The results of these simulations are shown for both the hot and cold scenarios in Figure 5.2 where $Z = 0$ is fixed at the original target surface. As can be seen, the temperature profile shows significant cooling

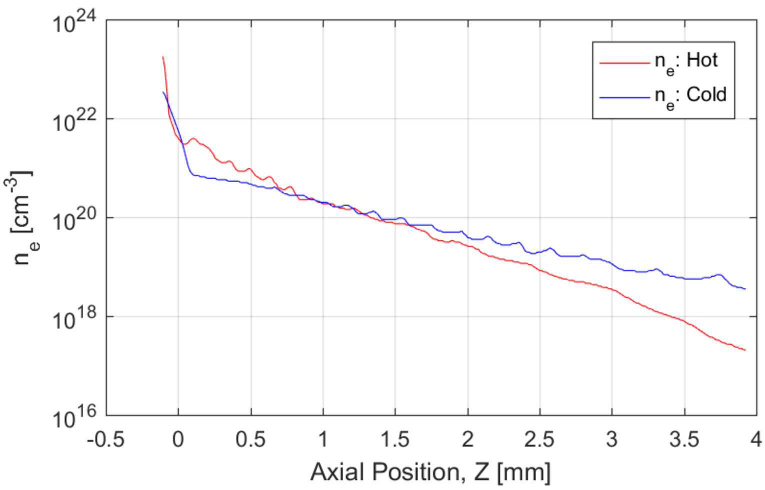

(a) Simulated density profiles

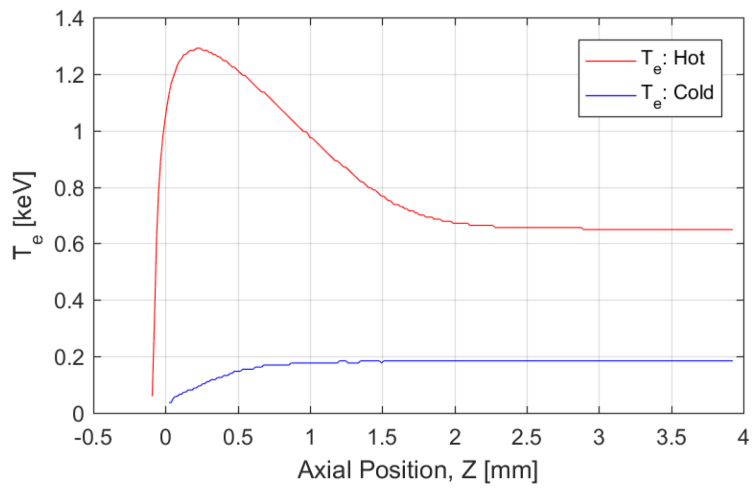

(b) Simulated temperature profiles

Figure 5.2: FLASH simulations for the channeling parameters experiment. As can be seen from these simulations, the expected density profile is expected to expand to a larger scale length 1.5 ns after the end of the drive pulse ('Cold' simulations) compared to 0 ns delay ('Hot' simulations). The electron temperature dramatically cools during this period as well.

of the plasma between the hot and cold plasmas, with the hot plasmas around 650 eV in the low-density regions, peaking at 1.3 keV near the ablation front while the cold plasmas remain a near constant 185 eV throughout the interaction region. At the same time, the density profile's scale length increases from 375 ± 8 µm in the hot simulation to 612 ± 6 µm in the cold simulation. Based on this, the focal position of the hot beam was varied between $Z = 1500$ µm, 900 µm, and 300 µm, corresponding to predicted density values at focus of approximately 0.08 n_c, 0.25 n_c, and 1.5 n_c where $n_c = 1.0 \times 10^{21}\,\mathrm{cm}^{-3}$ refers to the critical density for the IR pulse. In the cold plasma, the pulses were focused at about $Z = 1700$ µm, corresponding to a density of 0.08 n_c.

As stated above, the primary diagnostic used to observe the interaction of the channeling pulse with the plasma was the 4ω probe beam which passed transversely through the channel and was collected by several diagnostics including Faraday rotation polarimetry, shadowgraphy, and angular filter refractometry (AFR). These were then used to reconstruct the density profile of the plasma as well as observe both the channel depth and the filamentation of the channeling pulse. Secondary diagnostics were in place to measure the fast electron generation. These included various x-ray diagnostics, most notably a von Hamos spectrometer, and a multi-angle electron spectrometer fielded by Osaka University.

5.2 Density Reconstruction

In order to confirm the accuracy of the FLASH simulations used in designing the experiment, the density profiles were measured using the AFR diagnostic to infer the angular refraction due to density gradients in the images. As discussed in Section 4.3.4, these refractions give the phase of the image which, upon Abel inversion, reconstructs the density profile. The total error in this reconstruction is approximately ±15% [45]. However, this error increases at low densities due to the insensitivity of the diagnostic to global density shifts. This results in an error greater than the lowest density measured. Each reconstructed profile was well-fitted with a single exponential function with the coefficient of determination for these

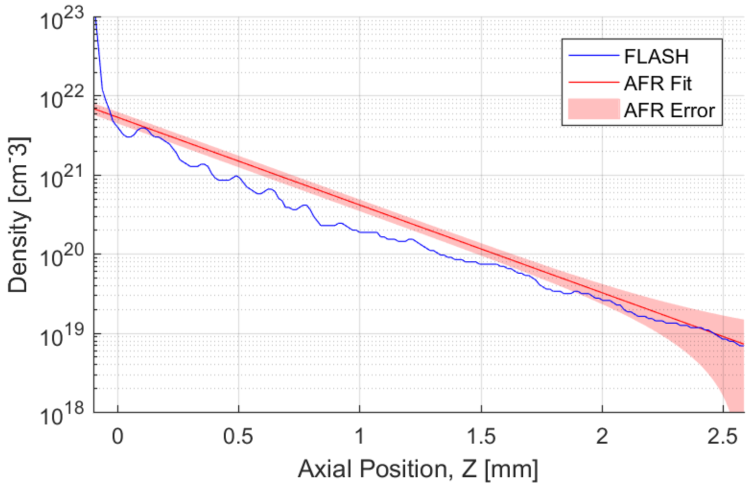

Figure 5.3: AFR density reconstruction for the channeling parameters experiment. Shown is a sample reconstructed density profile from a hot plasma in comparison to the corresponding FLASH simulations. While the scale lengths were comparable, the FLASH simulations were approximately half to a third of the AFR reconstruction for much of the interaction region.

fits given as $R^2 \geq 0.994$. The average profile had a $392 \pm 6\,\mu\text{m}$ scale length for the hot plasmas and $570 \pm 20\,\mu\text{m}$ for the cold plasmas. An example fit in a hot plasma is plotted against the corresponding FLASH density profile in Figure 5.3.

As can be seen, the reconstruction deviates slightly from the simulations, resulting in the pulses being focused instead at approximately $0.12 \pm 0.03\ n_c$, $0.53 \pm 0.08\ n_c$, and $2.5 \pm 0.4\ n_c$ in the hot plasma and at $0.11 \pm 0.03\ n_c$ in the cold plasma. While these do differ from the originally intended density values, the low-density focal position is still significantly below the quarter critical surface, while the mid- and high-density points are still focused at underdense and overdense points in the plasma. Thus they are still sufficient for the purposes of this experiment.

5.3 Channel Depths

The penetration depth for each pulse was determined by calculating the distance between the original target surface and the nearest point of bulk perturbation shown in the AFR images. The target's initial location was established from reference shots. Note that the AFR's data was used instead of the shadowgraphy results because several of the high-intensity shots produced a large enough electromagnetic

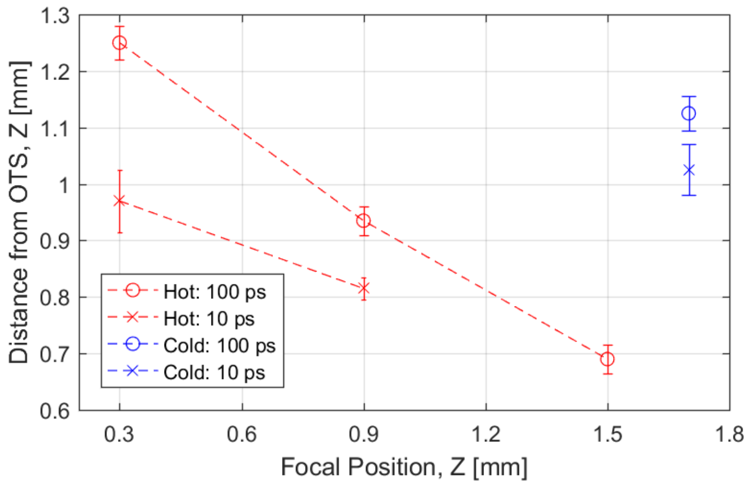

Figure 5.4: Channel penetration. The final distances from the original target surface (OTS) are plotted against the vacuum focal position for the 100 ps and 10 ps in both the hot and cold plasmas. Deeper penetration would therefore have a lower value. These measurements were made using the 4ω probe.

pulse to disable the shadowgraphy camera. However, as will be seen shortly, the features in each diagnostic extend to the same depth, and so the AFR was deemed an appropriate tool to determine these depths.

The depth calculation does not include the filament-like structures seen in front of the channels which will be discussed in more detail in Section 5.7. Figure 5.4 illustrates the results of this calculation for various applicable shots. The resolution of the AFR diagnostic was approximately 1.9 µm. However, uncertainty in the original target location and the clarity of the features being analysed introduced additional error. Note that there is no data for the lowest focal density 10 ps shot in a hot plasma as the probe pulse was delivered 5 ps before the channeling pulse due to jitter in the timings, thereby missing the full channel development. Several interesting trends can be taken from this data.

5.4 Timing Dependence

Due to the limited number of shots in this experiment, there were only two cold plasma shots - one high-intensity, one low-intensity, both focused 1.7 mm away from the original target surface at a density of $0.11 \pm 0.03\ n_c$. The comparable hot plasma

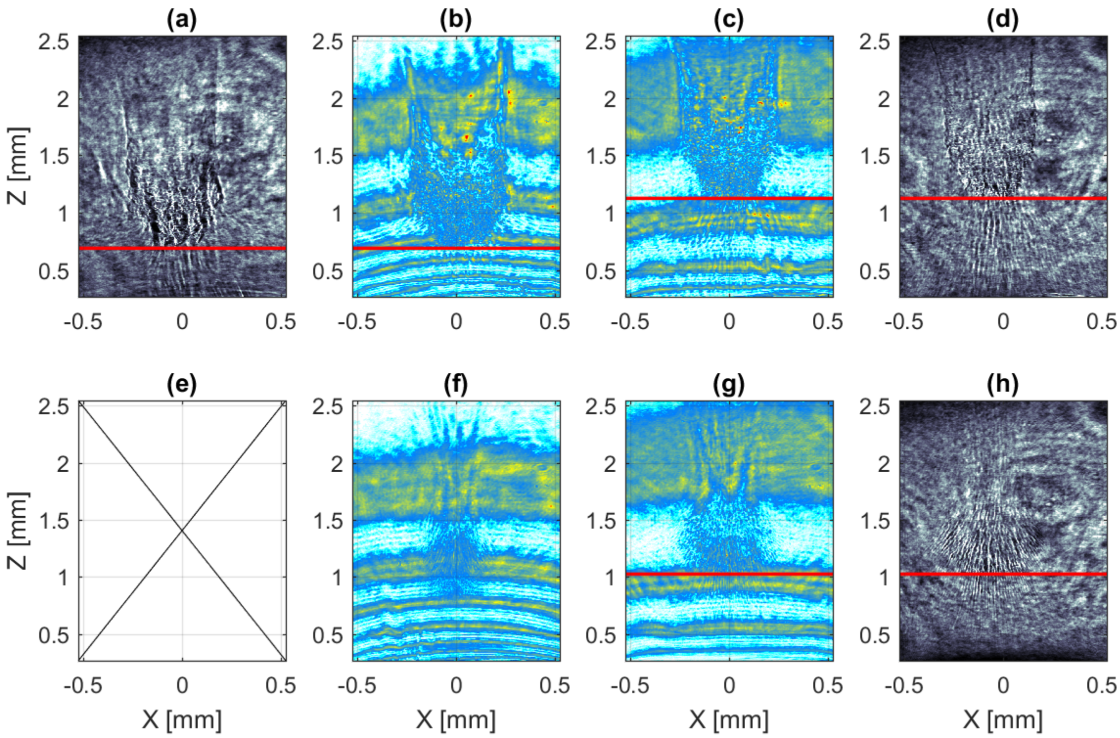

Figure 5.5: AFR and shadowgraphy images for the channel depth timing dependence. Shadowgraphs are shown in the outer columns and AFR images are shown in the inner columns, each having been cropped to show the region of interest. The top row shows the results of the 100 ps beam in a hot plasma, (a) and (b), compared to a cold plasma, (c) and (d). The bottom row does the same for the 10 ps beam with (f) showing the results of the hot plasma shot and (g) and (h) showing the cold plasma shot. Note that (e) is empty due to EMP disabling the shadowgraphy camera for this shot. The red lines are superimposed at the measured channel depth as plotted in Figure 5.4. Note that no red line is present in (f) as the probe arrived prior to the channeling beam, meaning that the observed channel here is incomplete.

shots were focused at $Z = 1.5\,\text{mm}$ with a corresponding density of $0.12 \pm 0.03\ n_c$. The AFR and shadowgraphy results are displayed in Figure 5.5.

Both shadowgraphs and AFR images were cropped and displayed here to illustrate the fact that both diagnostics show the same channel depth, thereby justifying Section 5.3's measurements. Horizontal red lines are superimposed onto these images at the depths measured in Figure 5.4.

Filamentation qualitatively appears to be worse in Figure 5.5(a) than Figure 5.5(d), which could initially suggest increased filamentation in a hot plasma counter to what was previously argued. However, using the AFR density reconstruction, the cold plasma shot only reached $0.30 \pm 0.05\ n_c$, just past the quarter-critical isosurface where filamentation has the greatest growth rate [92]. Thus, it is to be expected that less filamentation would be present in this case, and these results do not speak to the relationship between plasma temperature and filamentation.

While it is difficult to measure filamentation from these images, channel depth may readily be obtained. As can be seen, the channels clearly reached a greater depth when no delay was present between the drive and channeling beams. Even in the case of Figure 5.5(f) where only approximately half of the channel development is captured, the hot plasma shot had already passed the depth achieved in a cold plasma as shown in Figures 5.5(g)-(h).

This increased depth in the hot plasmas more likely has to do with the density profile rather than the temperature of the plasma. For the bulk of the interaction region, the density will be greater in the cold plasmas as the high pressure near the ablation front will have caused the high density region to expand outwards. The FLASH simulations predict that this will be true for $Z \gtrsim 1\,\mathrm{mm}$ as can be seen in Figure 5.2(a), though the AFR fits suggest that this may be closer to $Z \gtrsim 0.11\,\mathrm{mm}$ which would then cover the entire interaction region. As described in Section 2.7.6, in a significantly underdense plasma, the channel depth is determined by the number of particles with which the beam has interacted. Because the density is greater in the cold plasma, it is appropriate that the channel would not have penetrated as deeply.

5.5 Focal Position Dependence

The strong downward slope in Figure 5.4 illustrates that the pulses were clearly able to penetrate deeper into the plasma when they were focused further from the target surface. This lends support to the whole-beam self-focusing scheme referenced in the introduction to this section. The pulses focused at a high density had a larger spot size as they propagated through the plasma, and thus they were more susceptible to filamentation [92] while additionally interacting with more particles, leading to earlier pulse depletion as predicted in Section 2.7.6.

This deterioration of the channel's quality may be seen clearly by looking at the shadowgraphs and AFR results of the low-intensity channeling beam at various focal

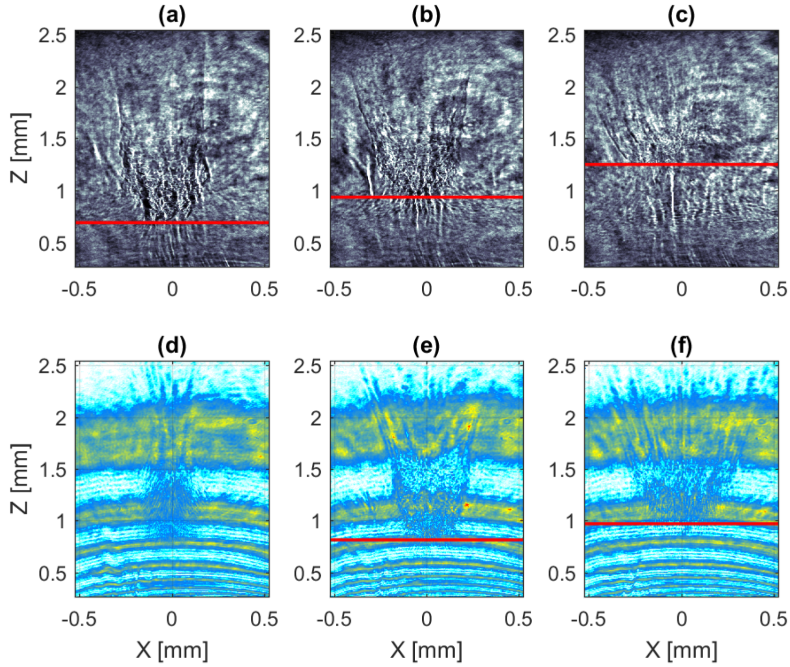

Figure 5.6: AFR and shadowgraphy images for the channel depth focal position dependence. Shadowgraphs for the 100 ps pulse in hot plasmas are shown for focal positions (a) 1.5 mm, (b) 0.9 mm, ad (c) 0.3 mm. Due to issues with the shadowgraphy camera on the high-power shots, AFR images are shown instead for the 10 ps pulse at focal positions (d) 1.5 mm, (e) 0.9 mm, and (f) 0.3 mm. Superimposed red lines indicate the measured channel depth. Note that (a) and (d) are reproduced from Figures 5.5(a) and 5.5(f) respectively for ease of viewing.

positions in hot plasmas as shown in Figure 5.6(a)-(c). It is worth noting that even though relativistic self-focusing is expected to have occurred, the channels themselves are quite wide. This may be attributed in part to filamentation. The shadowgraph of the low focal density pulse in Figure 5.6(a) illustrates this well with the finger-like structures seen near the head of the channel. Each of these filaments appears to be 10-25 µm in diameter as a rough approximation, though an exact measurement is impossible with the present diagnostics. Tomographical probing could be a viable method for gaining a more complete picture of the channel's structure. It is worth noting that these filaments appear more strongly at the head of the channel than earlier in its formation. This is due to the pulse continuing to erode the walls between the pulses as seen previously in PIC simulations [28] and experiments [115].

These filaments would be seemingly at odds with the predictions of the whole-beam self-focusing scheme. However, there are a number of explanations for why

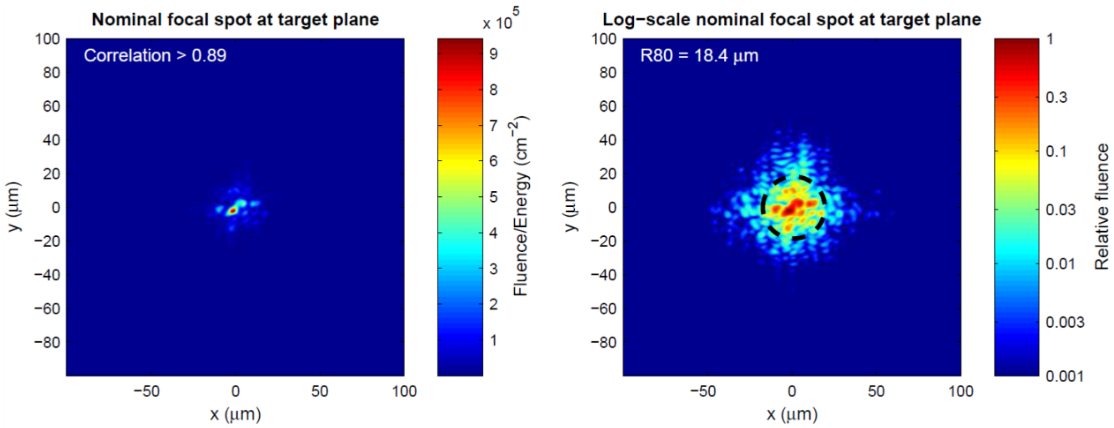

Figure 5.7: Channeling beam profile. Strong speckling of the channeling beam at focus may be observed. The right image shows the nominal fluence on a log-scale with 80% of the energy contained within an 18.4 µm radius as indicated by the black dotted line.

the pulse continued to filament. First, the pulse was not focused at a low enough density. According to the scheme, the pulse would have to be focused to a point which would allow self-focusing to shrink the spot size to approximately the plasma wavelength by the time it reached the quarter critical isosurface. If there was insufficient self-focusing, this would not be obtained. Additionally, whole-beam self-focusing assumes an ideal laser pulse with a smooth transverse profile while realistic pulses are often speckled. This means that realistic pulses have severe intensity modulations and are not perfectly shaped into the desired profile transversely due to deformations of the phase front. Figure 5.7 shows an example spot profile of the channeling beam used in this experiment – in this case, the 100 ps beam focused at $Z = 1.5$ mm in the hot plasma. As can be seen, strong speckling is present with several peaks separated by a few microns.

Speckling affects the pulse's ability to focus in vacuum, altering the Rayleigh length away from the theoretical value of $\pi w_0^2/\lambda$ which assumes a perfect Gaussian beam. An imperfect pulse focused off of an f/2 parabola to an 18 µm spot size can expect to have a Rayleigh range on the order of 10-50 µm. This is a full order of magnitude less than the variation in the focal positions, indicating that these variations were more than sufficient to cause significantly different beam profiles within the plasma. Additionally, as discussed in Section 2.7.4, these intensity modulations lead to ponderomotive filamentation as well.

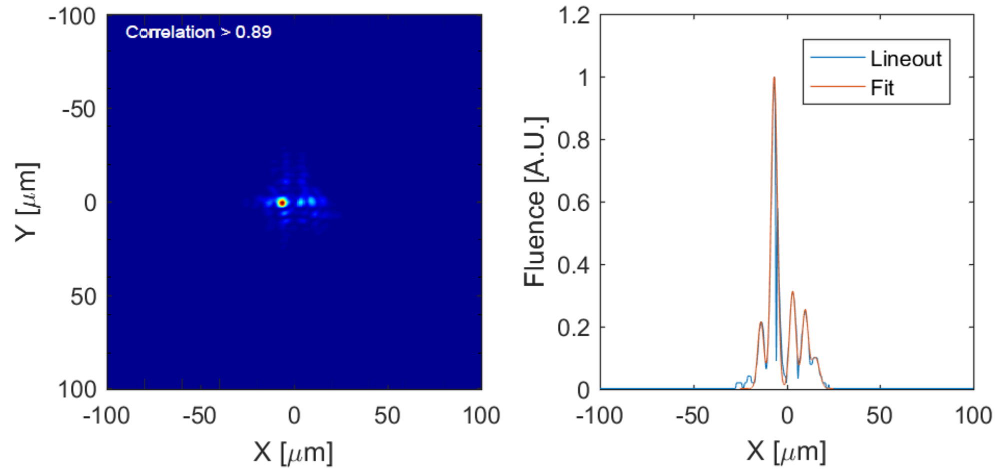

Figure 5.8: Simulated channeling beam profile. The left image shows the nominal fluence of the focal spot at the target plane. A horizontal lineout was taken at $Y = 0\,\mu\text{m}$ and fitted with five Gaussian functions. The results of this lineout and fit are shown in the bottom plot.

In order to test this effect, PIC simulations were run using the 2D OSIRIS code, details of which can be found in Chapter 3. A p-polarised 10 ps pulse (0.5 ps rise and fall times and 9.5 ps flat time) was focused 392 µm into an inhomogeneous deuterium plasma with a 392 µm scale length in a 784 µm × 150 µm window. This pulse's profile was either a perfect Gaussian pulse with 80% of its energy contained within a 15 µm radius and $a_0 = 3.1$, herein known as the 'perfect beam', or a combination of five Gaussian beams fitted to a previously obtained OMEGA pulse profile of comparable total energy, the 'imperfect' beam. The fit of this imperfect beam is shown in Figure 5.8. This profile was chosen rather than one present in this experiment as it lent itself well to a single line out. Note that the data shown here is fluence which is proportional to a_0^2. The intensity of this pulse was scaled so that it possessed the same total energy as the perfect beam. The plasma was made up of three fluids: electrons, fully ionized carbon ions, and hydrogen ions. The density at the centre of the window was 0.11 n_c, and the grid size was $15,680 \times 3000$ for a 50 nm resolution.

To ensure that the beam had been correctly simulated, the plasma was first omitted from the simulation to test the pulse profile in vacuum. Unfortunately, as shown in Figure 5.9, the fitted beam was not successfully recreated. This could

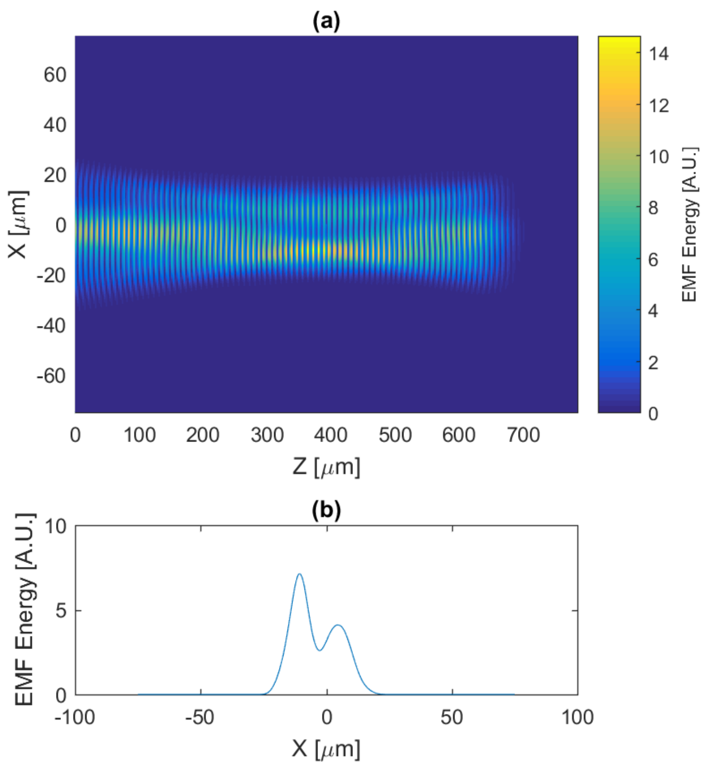

Figure 5.9: Simulated intensity profile of imperfect beam in vacuum. (a) The spatially resolved electromagnetic energy of the vacuum simulation is shown after 2.5 ps in (a). A lineout at $Z = 392\,\mu\text{m}$ was taken and is plotted in (b). As can be seen, the simulation did not successfully capture the fitted spot shown in Figure 5.8, but instead generated two broad peaks at focus.

have to do with the relative phase of individual speckles. As can be seen, the pulse only had two peaks at focus which were much broader than originally intended. Still, the pulse is not perfect and can give some indication of the effects of speckling, though this simulation will instead represent the minimal effects rather than the realistic intended results of speckling.

The results of the full simulations are shown in Figure 5.10. As expected, the imperfect beam simulation did experience more filamentation early in its propagation than the perfect beam, diverging into two primary filaments in line with the intensity distribution. However, after 3 ps, much of the ponderomotively-formed density perturbation had been eroded and the pulse was able to continue propagation mostly as a single beam. This was consistent with simulations which were performed in preparation for the experiment which utilized a much more

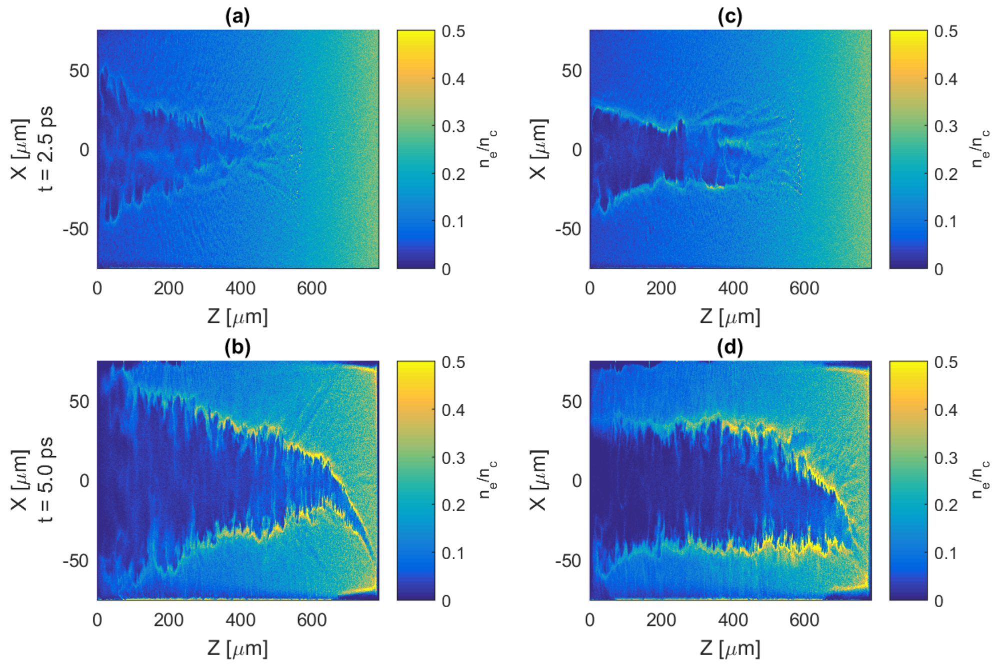

Figure 5.10: Simulated channel profiles for a perfect and a speckled beam. Shown are the electron density profiles after (a)(c) 3 ps and (b)(d) 5 ps for (a)(b) the perfect beam and (b)(d) the imperfect beam.

sharply speckled beam. Meanwhile, the perfect beam simulation still did experience low levels filamentation after undergoing self-focusing. This occurred through the intensity modulations induced by self-focusing as discussed in Section 3.6. At later times, both simulations' filaments reconnected to form a single channel. However, while the perfect beam did manage to self-focus to a tighter spot, the imperfect beam remained relatively wide.

The original filamentation along the lines of the electromagnetic energy distribution suggests that a successful run which properly simulates the speckling in Figure 5.8 would experience more extreme filamentation and therefore supports the hypothesised effects of beam speckling on pulse propagation. Therefore, filamentation in the experimental results can be attributed at least in part to beam speckle. While whole-beam self-focusing was not achieved in this experiment, the results show evidence supporting the scheme for the first time in large scale length plasmas by obtaining one of its major purposes – deeper penetration without increased energy requirements.

5.6 Intensity Dependence

Perhaps the most interesting result of this experiment comes from the performance of the high-power versus low-power pulses. Previous work has shown that the low-power pulses should require less energy to reach the critical surface than high-power pulses [28]. This result was derived from 2D3V PIC simulations featuring Gaussian pulses propagating through an exponentially increasing plasma with a scale length of 430 µm and various relativistic intensities (assuming a 1 µm scale length). Pulses with an intensity of 10^{18} W cm^{-2} were expected to reach approximately 0.6 n_c after 100 ps while 10^{19} W cm^{-2} pulses were predicted to reach approximately 0.4 n_c after 10 ps. This corresponds to an additional 170 µm channel depth for the low-intensity pulses. These parameters are all very similar to those found in this experiment.

An earlier experiment was conducted to confirm these PIC results [116]. The results showed the low-intensity pulses consistently reaching the critical surface while the high-intensity pulses failed to do so, and the channel velocity measurements roughly agreed with Li *et al.*'s predictions. However, that experiment had approximately double the energy in the low-intensity pulses compared to the high-intensity pulses. Thus it is not surprising that they would reach a greater overall depth given the physical picture of channeling and hole-boring presented in Section 2.7.

Here, where the energy is only 12% greater in the low-power case, a different trend emerges. In the hot plasmas, high-power shots actually outperformed the low-power shots both in terms of channel depth and quality. As can be seen in Figure 5.11, the channel itself appears to be narrower and more collimated compared to the low-power case in hot plasmas, though as discussed in Section 5.4, it had a worse profile in the cold plasma. This can largely be attributed to the duration of the pulses. Recall from Section 2.7 that the channel's transverse density profile may be approximated by:

$$\left(\frac{\partial^2}{\partial t^2} - c_s^2 \boldsymbol{\nabla}_\perp^2\right) \frac{n_{i1}}{n_{i0}} \approx \frac{Z m_e}{m_i} c^2 \boldsymbol{\nabla}_\perp^2 \left(1 + \frac{a^2}{2}\right)^{1/2} \tag{5.1}$$

where $c_s = (Zk_B T_e/m_i)^{1/2}$ is the sound speed, n_{i0} is the initial density profile, and n_{i1} is the perturbation to that initial profile. This equation may be integrated

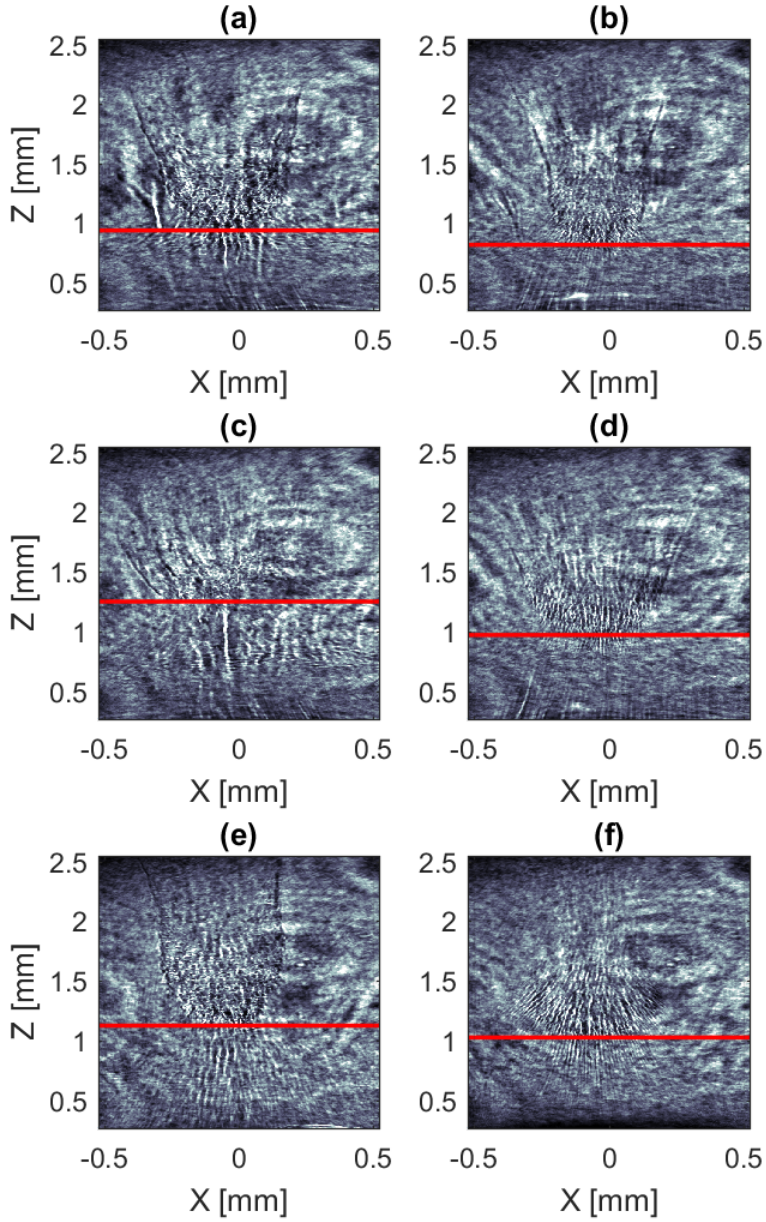

Figure 5.11: Shadowgraphy images for the channel depth intensity dependence. Shadowgraphs are shown for the three relevant intensity comparisons. The left column shows the channels formed by the 100 ps pulse while the right column corresponds to the 10 ps pulse. (a)-(b) are in a hot plasma with focal positions at $Z = 0.9$ mm, (c)-(d) are in a hot plasma with focal positions at $Z = 0.3$ mm, and (e)-(f) are in a hot plasma with focal positions at $Z = 1.5$ mm. Superimposed red lines indicate the measured channel depth. Note that several of these images are reproduced from Figures 5.6 and 5.5 for ease of comparison.

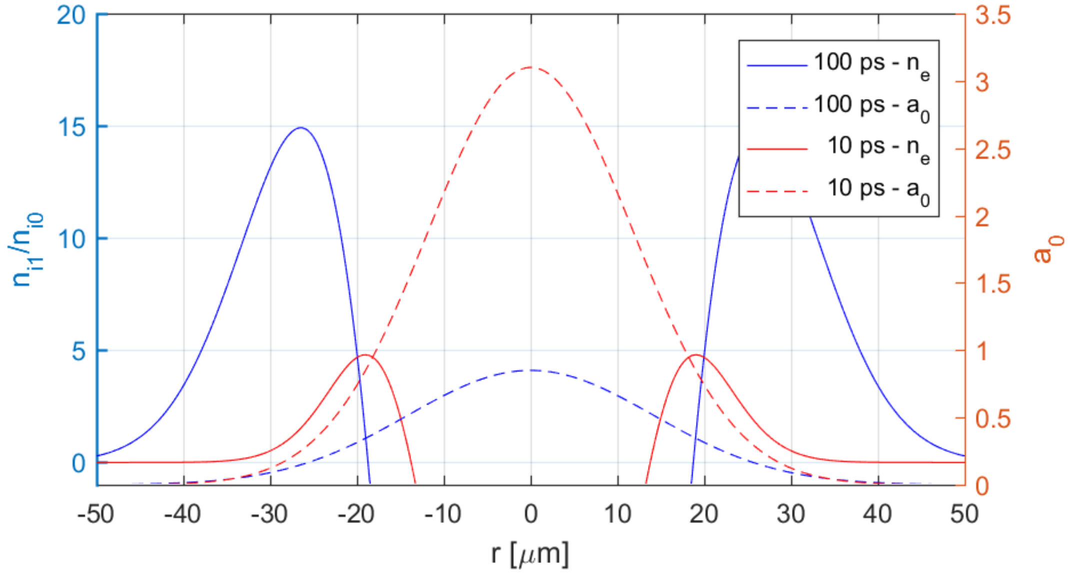

Figure 5.12: Integration of channeling profile equation for experiment's pulses. Equation 5.1 was integrated using the pulse parameters found in this experiment through the end of the pulses' durations.

assuming 3D cylindrical symmetry and using the two sets of parameters observed in this experiment. Specifically, this means the first integration was through 100 ps using $a_0 = 0.85$ and 80% of the three-dimensional energy contained in $r = 18\,\mu\text{m}$, and the second was through 10 ps with $a_0 = 3.1$ and $r = 15\,\mu\text{m}$, both using Gaussian longitudinal profiles. The results are shown in Figure 5.12. As can be seen here, the channel walls of the 100 ps pulse are much greater than those of the 10 ps pulse and the channel itself is much wider. This matches what is seen in the shadowgraphs as the 100 ps channels are much wider with more distinct walls, corresponding to a greater density gradient.

More importantly and contrary to the above referenced numerical investigations, in both the hot and cold shots, the high-intensity pulse actually achieved deeper penetration than its low-intensity counterpart despite having less total energy. While more work is required to explain this discrepancy with certainty, evidence suggests that it arises from three-dimensional effects. A follow-up study for the original PIC simulations was performed which featured a single 3D3V PIC simulation [117]. In it, Li *et al.* found that the channel penetrated through the plasma at a much greater velocity and with far fewer chaotic features. The explanation for this is

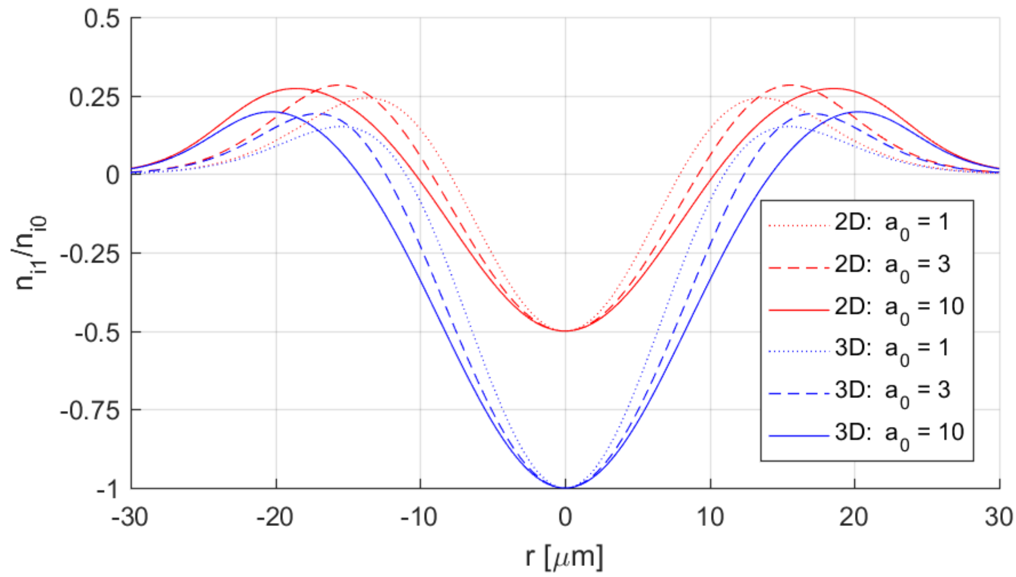

Figure 5.13: Integration of channeling profile equation at various intensities. Equation 5.1 was integrated until the 3D density profile was fully evacuated at various intensities. Red lines indicate the integration was performed in 2D while blue lines indicate 3D. Dotted lines correspond to $a_0 = 1$ at $t = 3.758\,\text{ps}$, dashed lines to $a_0 = 3$ at $t = 1.732\,\text{ps}$, and solid lines to $a_0 = 10$ at $t = 0.907\,\text{ps}$.

given both by the ease of channel formation in 3D and the focusing of the laser pulse. Each of these points will be analysed here.

As discussed by Li *et al.* [117], Equation 5.1 may be integrated using the exact same parameters in both 2D and 3D yet yield lower densities, and thus faster channel formation, in 3D compared to 2D. Mathematically, this is because of the form $\nabla_\perp^2$ takes in each dimension, with $\nabla_{\text{2D}}^2 = \partial_r^2$ and $\nabla_{\text{3D}}^2 = r^{-1}\partial_r(r\partial_r)$ where cylindrical symmetry has been assumed [117]. Figure 5.13 shows the result of integrating Equation 5.1 at various intensities until the 3D channel is fully evacuated on axis. This corresponds to times $t_1 = 3.758\,\text{ps}$, $t_3 = 1.732\,\text{ps}$, and $t_{10} = 0.907\,\text{ps}$ for $a_0 = 1$, $a_0 = 3$, and $a_0 = 10$ respectively. While the channel profile does vary, the density on axis was the same in 2D at the presented times regardless of intensity. Thus, while dimensionality does affect the channeling speed of pulses, it does so independently of intensity and therefore would not affect the relative performance of the pulses in this experiment.

One important phenomenon missing from Equation 5.1 and the subsequent

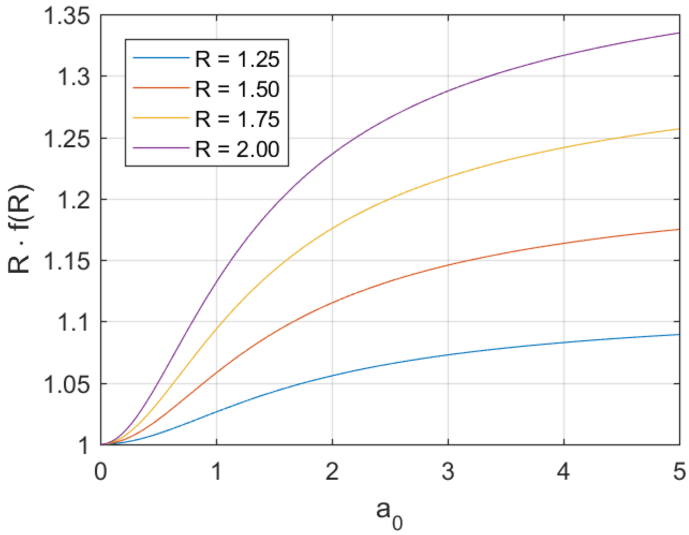

Figure 5.14: Channeling velocity dependence on intensity and self-focusing ratio. Plotted is the ratio of channeling velocity when a pulse experiences a self-focusing ratio of R. As can be seen, this has little effect at lower intensities, but increases until plateauing at $R^{1/2}$.

analysis is self-focusing. As a pulse continues to propagate through the plasma, it will ponderomotively and relativistically self-focus. Assuming the laser energy largely stays within the channel, power conservation requires $a^2w = a_0^2w_0$ in 2D and $a^2w^2 = a_0^2w_0^2$ in 3D where w is the channel width and 0 subscripts indicate vacuum values [117]. Thus, the intensity will increase by a factor of $R \equiv w_0/w > 1$ in 3D compared to 2D. According to the physical models of Section 2.7.6, the hole-boring depth is proportional to a_0 while the channeling depth is proportional to $a_0^2/(\gamma-1)$ where γ is the Lorentz factor. Thus, comparing 3D to 2D, self-focusing will increase the depth achieved in the hole-boring regime by a factor of $R^{1/2}$ while the channeling depth will be increased by $R \cdot f(R)$ where $f(R) \equiv (\gamma(R)-1)/(\gamma(R^2)-1)$ and $\gamma(\xi) = (1+\xi \cdot a_0^2/2)^{1/2}$ for a linear pulse. The increase to the channeling depth therefore approaches $R^{1/2}$ as a_0 increases, but it has a strong intensity dependence for smaller values of a_0.

Figure 5.14 plots $R \cdot f(R)$ as a function of a_0 to illustrate this intensity dependence. As can be seen here, the channeling depth experiences little effect from self-focusing for low intensities. This is in line with expectations as the low-intensity approximation of the channeling depth is independent of intensity. However, this function begins to increase rapidly with a_0 until plateauing at $R^{1/2}$. As a result, the high-intensity pulses in this experiment would have experienced greater penetration while still in the channeling regime than the low-intensity pulses. This could then alter the relative channel depths seen within the experiment.

In order to properly verify these effects, several three dimensional PIC simulations would be required to recreate the original simulations performed by Li *et al.* [28]. Unfortunately, this is currently computationally infeasible. Instead, a series of 2D cylindrical simulations have been designed to approximate the three-dimensional behavior of a pulse. OSIRIS currently only has limited support for such simulations, though this is expected to be rectified in the future.

5.7 Leading Filaments

As stated earlier, the minor filament-like structures in front of the channel were not included in the calculation of the channel depths. Examples of these filaments are shown in Figure 5.15. As this figure illustrates, these filaments took various forms but were nonetheless present in some manner in each shot. Figure 5.15(a) shows faint, straight perturbations, while Figure 5.15(b)'s front filaments are much more pronounced. Figure 5.15(c) appears to be some form of a combination between the two. All of these features are extremely narrow, between 3-5 µm wide, and often extend beyond the critical surface, suggesting that they are formed by fast electrons rather than the channeling pulse directly. More specifically, the faint filaments are caused by the bunching of fast electrons as they propagate through the plasma, consistent in structure with previous experiments and simulations [118–120]. The more intensely focused filaments are caused by electron beams which have been pinched together by the strong magnetic fields within the channels – a phenomenon first observed by Pukhov and Meyer-ter-Vehn in 1996 using PIC simulations [50].

While separately these structures are interesting for the study of electron transport, they were not included in the channel depth calculations for a variety of reasons. Their formation was not predictable within this experiment, and thus they are not reliable quantifiers when determining the depth a channeling pulse may

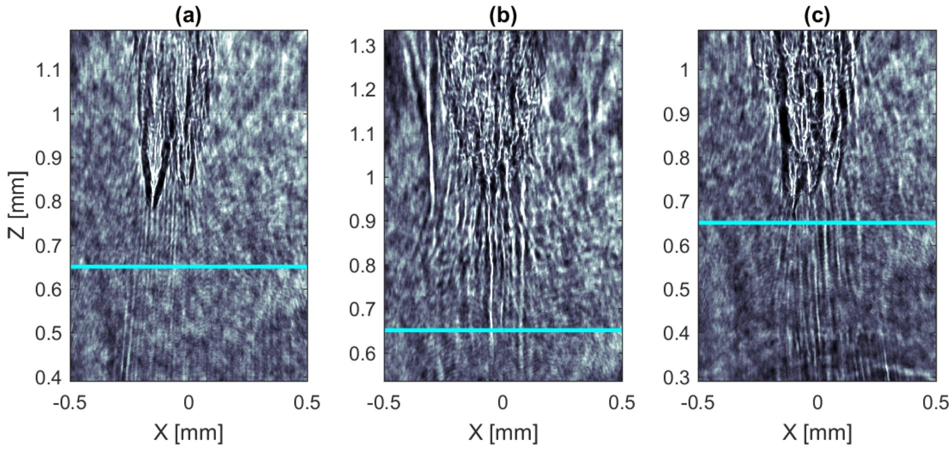

Figure 5.15: Examples of leading filaments. Cropped shadowgraphs are shown for (a) 10 ps pulse at half energy, focused at $Z = 1.5$ mm, (b) 100 ps pulse focused at $Z = 0.9$ mm, and (c) 100 ps pulse focused at $Z = 1.5$ mm. Superimposed cyan lines indicate the critical surface based upon the AFR reconstruction.

achieve. Further, Section 5.6 compares the channel depths to those predicted by [28]. That paper defined the channel depth as the location where the averaged density fell below 10% of the critical density. This averaging was reportedly done over the plasma within a 7.5 µm radius of the propagation axis. As such, these structures would have been too narrow to have affected the calculation in this previously published work, and including them here would make for an inappropriate comparison.

5.8 Secondary Diagnostics

The secondary diagnostics showed strong agreement with the trends discussed above. Fast electrons will be generated through the channeling process, and these will generally diverge at angles up to 55° [24, 34, 35]. Thus, the deeper the channel, the more concentrated these fast electrons will be as they reach the rear of the copper-backed target. This in turn will raise the number of electrons collisionally ejected from lower shells in the copper atoms, and the K_α signal seen in the von Hamos spectrometer will increase. Further, the cross-section of K_α florescence varies slowly with electron energy [100–102]. Therefore, while this diagnostic is not suitable for comparing high-intensity to low-intensity shots, it does adequately capture the relative fast electron flux when varying the focal position for each intensity.

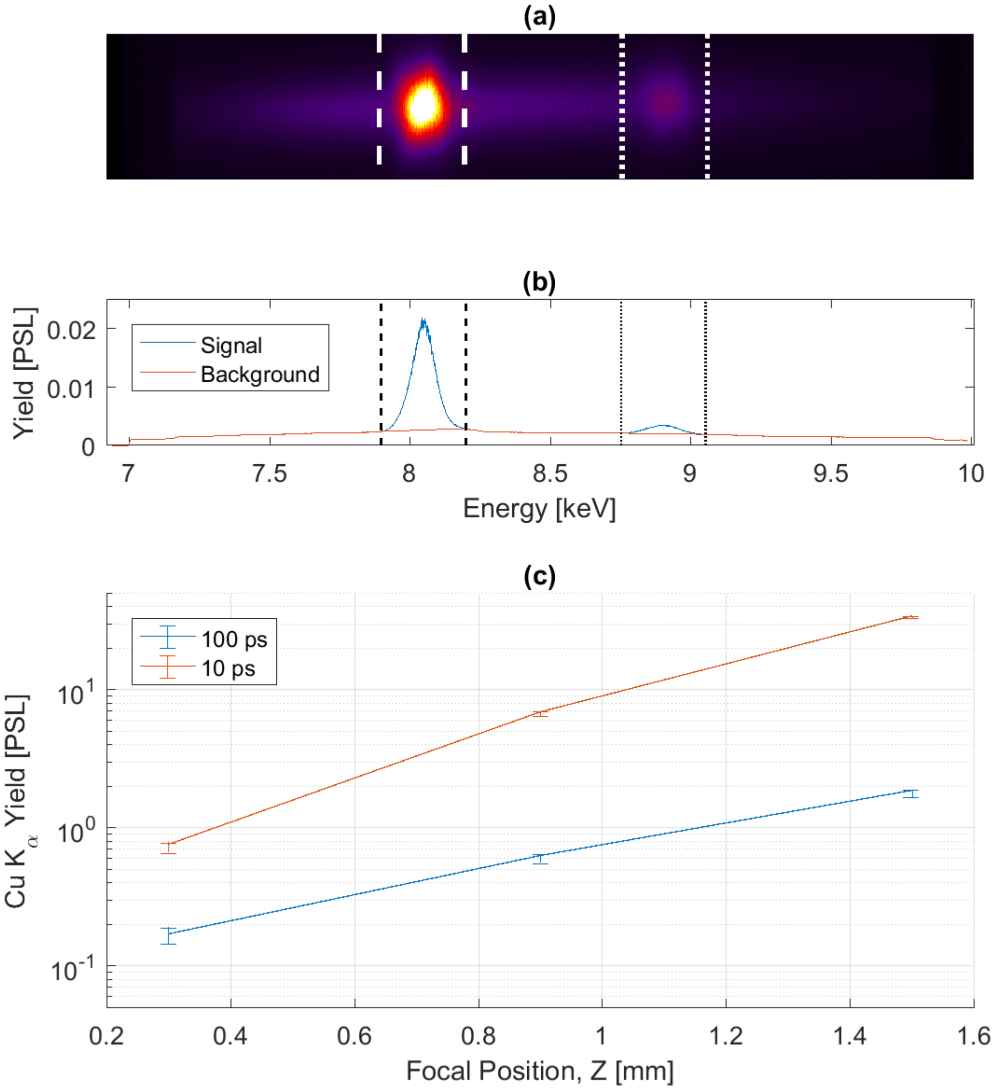

Figure 5.16: Von Hamos spectrometer output and Cu K_α yield. An example von Hamos spectrometer signal is shown in (a) with white dashed lines indicating the Cu K_α region and dotted lines indicating the Cu K_β region. An integrated lineout is shown in (b) along with the background profile. The K_α region was then integrated within a 0.15 keV range of its peak to calculate the total Cu K_α yield plotted in (c) for each hot plasma shot.

Figure 5.16(a) shows an example image plate scan from the von Hamos spectrometer. The signal has two peaks with the larger in amplitude corresponding to Cu K_α and the lower to Cu K_β. Each image was integrated vertically to give a total spectrum and is plotted as a function of energy in Figure 5.16(b). The total Cu K_α yield was found by integrating the signal within 150 eV of the 8048 eV peak, indicated by dashed lines superimposed on the first two images of this figure. This integration was performed twice more with a radius 25% larger and 25% smaller about the K_α peak to provide error measurements of this calculation. The background was calculated through linear interpolation between these endpoints. The resulting yield is plotted as a function of focal density in Figure 5.16(c). Notice that this yield closely follows the trends in channel depth shown in Figure 5.4. The shots which produced the deepest channels also had the brightest K_α yields. This is as expected and provides support to the depth measurements as a function of focal position.

The results of the von Hamos diagnostic are dependent upon the total fast electron production. However, the number of fast electrons produced remained relatively constant for each intensity level. This can be seen by analysing the Osaka University multi-angle spectrometer. This diagnostic was comprised of five separate spectrometers, each angled at 5° relative to one another for a total capture angle of 20°. The centre channel was placed directly along the channeling beam's alignment axis on the opposite side of the target in order to observe the fast electrons produced by the channeling interaction. The data was calibrated and extracted by Hideaki Habara of Osaka University.

The fast electron production per steradian for each shot was found by integrating the spectra with respect to energy, $dN/d\Omega = \int_{E_{\min}}^{\infty}(d^2N/dEd\Omega)dE$ where $dN/d\Omega$ is the number of electron per steradian and E is the energy of the electrons. To see only the fast electron production, the minimum energy, $E_{\min}$, was set to 1 MeV. The 100 ps pulses did not produce a significant number of electrons in excess of this energy, and so this analysis was restricted to the 10 ps pulses. The results of this integration showed the fast electron production remained relatively constant, varying on-axis by a factor of 4.4 and off-axis in the 10° spectrometers by a factor of

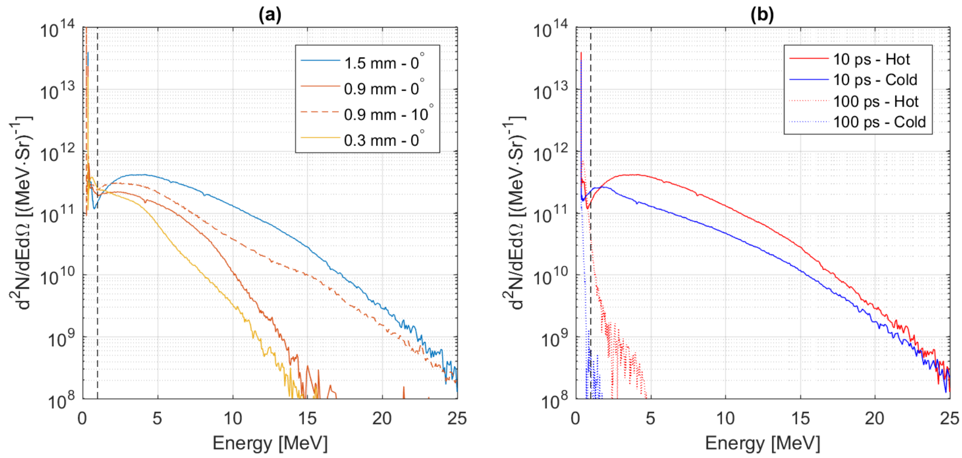

Figure 5.17: Fast electron distribution from Osaka University's multi-angle electron spectrometer. The fast electron production of the 10 ps beam at various focal positions in a hot plasma is plotted in (a). The angles in the legend indicate which component of the diagnostic is being plotted. (b) shows the on-axis (0°) fast electron production for both the 10 ps and the 100 ps pulses when focused at low density in both hot and cold plasmas. The vertical dashed lines indicate the minimum energy when determining the total number of fast electrons produced.

2.2. Allowing all electron energies detectable by the spectrometer ($E_{\text{min}} = 0\,\text{MeV}$) changed these values to 3.3 on-axis and 2.3 off-axis. Thus, the total fast electron production would have little effect on the output of the von Hamos spectrometer, supporting the trends observed in Figure 5.16.

In the majority of the shots, the central channel had the greatest production of high-energy electrons as would generally be expected. However, this was not so for the 10 ps pulse focused at $Z = 0.9\,\text{mm}$, thus justifying its inclusion in Figure 5.17(a). As is evident from this image, more fast electrons were produced at this angle to the channel's original propagation axis. On its own, this would suggest hosing was present for at least some of the pulse's filaments during late-time propagation. While this is not seen in the shadowgraphy results, the probe beam would have passed tangentially to the hosing plane detectable by the spectrometer, making its presence less pronounced. Still, its absence from the shadowgraphs does raise suspicion and thus makes it difficult to form definitive conclusions. Instead, it is discussed here as a point of interest which has not yet been resolved and to provide additional arguments for the need for tomographical probing capabilities

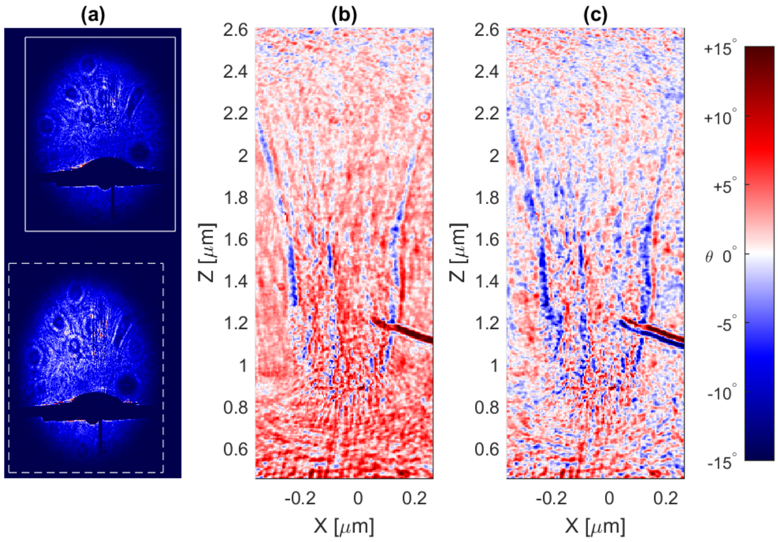

Figure 5.18: Polarimetry of the channels. The raw signal for the 10 ps pulse focused at $Z = 0.9$ mm is shown in (a). Superimposed white boxes indicate the S (solid lines) and P (dashed lines) images as defined in Section 4.3.3. (b) shows the cropped calculation of the beam rotation angle, θ without any normalizations. (c) shows the same calculation after normalizing the S and P images using the plasma-free shot's images. The axes on (b) and (c) are not exact due to the image transformations involved in aligning the two raw images, but are well matched to the shadowgraphy results and therefore provide a reasonable estimate.

in experiments focused on channel formation.

Another interesting trend can be seen by comparing the fast electron production of the 10 ps and 100 ps pulses when focused at low density in hot and cold plasmas. This is shown in Figure 5.17(b). Both spectra were reduced in the case of a cold plasma, though this reduction was much more dramatic for the 100 ps pulse. This suggests an increase of filamentation within the channel, reducing the intensity of any single beamlet and thus reducing the fast electron production.

One final diagnostic worth discussing in this experiment is polarimetry using the 4ω probe. A script was written to identify the two images within the detector's output using a k-means clustering algorithm. These images were then aligned using Matlab's built-in image registration scripts, and the polarisation rotation angle was calculated as described in Section 4.3.3. There was difficulty with the polarimetry beam's transport, likely due to misalignment of the Wollaston prism and lens imprinting. As a result, the detectors were not evenly illuminated even with no plasma present, and the signals experienced bubble-like distortions. These distortions may be seen in Figure 5.18(a). It is also clear from this figure that the P image, boxed in dashed lines, was significantly brighter than the S image, boxed in solid lines. As a result, when calculating the probe's polarisation rotation angle, there was an offset towards positive values as is evident in Figure 5.18(b). In order to compensate for the illumination differences, the signal images were normalized using data from the shots without any plasma. The results, shown in Figure 5.18(c) had poor signal-to-noise ratios, and thus the magnetic fields were not able to be quantitatively measured. Note that the large specks in Figures 5.18(b)-(c) are due to dust on the detector.

Despite the implementation issues with this diagnostic, one interesting trend is discernible. As discussed in Section 2.4.2 and seen in the simulations throughout Chapter 3, each filament of a channel will create its own left-hand azimuthal magnetic fields. These fields are formed by the strong current generated as electrons are accelerated forward by the ponderomotive force along the channel's axis, and by the return currents along the channel's walls. These fields continue to persist beyond the end of the channeling pulse as electron vortices form [121–123]. As such, this diagnostic is well-suited for identifying filamentation within this experiment. While the noise was too large to quantitatively determine the magnetic fields, there are clear striations along the channel's path. These support the conclusion that filamentation was present and caused the channel to appear wider than the vacuum focal spots would have suggested.

5.9 Fully Integrated Fast Ignition at OMEGA

This parameter scan experiment was not a stand-alone exploration, but rather, a part of a larger overall campaign designed to investigate the feasibility of fast ignition in general. Two fully integrated fast ignition experiments were also run in joint shot days at OMEGA and OMEGA EP. These were the first full-scale fast ignition experiments to use hole-boring in the ignition phase. The author's role in these experiments was to advise on the channeling beam's parameters and provide

PIC simulations of the channeling process. As this thesis focuses on channeling, this section is not intended to provide a complete analysis of these experiments, but rather, it is here to give context to the parameter scan experiment and demonstrate its applicability to ICF-type plasmas.

Both experiments used the OMEGA facility's 20 kJ, 60-beam, 3ω drive to implode a plastic spherical shell target to high densities. This target was composed of a 17 µm outer CH layer with an inner 23 µm deuterated plastic layer. The inner layer was doped with copper (1% by atomic density) in order to provide K_α fluorescence imaging. These x-rays were captured with a spherical crystal imager (SCI) and directed to an image plate to obtain a time-integrated view of the emissions. After the drive beam ceased propagation, a 1 kJ, 100 ps channeling beam followed by a 1 kJ, 10 ps heating beam were injected into the plasma. The fast electrons generated by the heating beam in the 1-3 MeV range were directed towards the dense core and where they would collisionally deposit their energy. The Osaka University multi-angle electron spectrometer was placed on the opposite side of the target to capture the fast electron profile. Finally, a neutron time-of-flight detector measured the fusion neutron yield from the D-D reactions.

The temporal evolution of the implosions was simulated using the 1D radiation-hydrodynamics code, LILAC [124]. In the first experiment, peak areal density of $\rho R \approx 400\,\mathrm{mg\,cm^{-2}}$ was expected to be reached after 4.3 ns. As such, the channeling and heating pulses were injected at various times between the end of the drive pulses and peak compression.

Figure 5.19(a) shows the output of the SCI diagnostic with no channeling or heating beams. K_α emission occurred as keV electrons produced during the drive phase excited the copper doping of the inner layer, creating the thick outer rings. The target also emitted K_α radiation at peak compression, appearing in the diagnostic as the central peak. When the channeling and heating beams were injected shortly after the drive beams ceased in Figure 5.19(c), an additional arc appears as the MeV electrons passed through the copper doping. Finally, Figure 5.19(d) shows the SCI output when only the heating beam was injected at peak compression. The

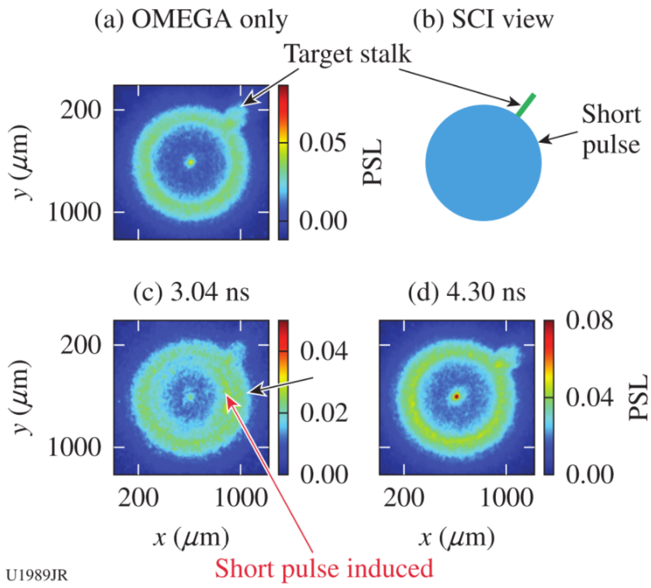

Figure 5.19: Spherical crystal imaging results for the first integrated fast ignition experiment. (a) shows an OMEGA only implosion with no channeling or heating beams. (b) illustrates the geometry of the target and the short pulse injection point. (c) shows the K_α emission when the short pulses were injected at 3.04 ns. (d) shows the results of utilizing only the 10 ps heating beam at peak compression. Image reproduced with permission from LLE Review, Volume 144, p. 244.

central emission greatly increased in this scenario, showing the deposition of energy from the fast electrons to the compressed core. The channeling beam was omitted in this last image for reasons which will now be made evident.

It is interesting to compare the fast electron spectra to the timing of the pulses. When the channeling pulse was injected into the plasma at early times (peak injection at 3.04 ns after the start of the drive pulse), the electron spectrometer detected a significant number of MeV electrons. However, as the injection time was delayed further towards peak compression, this signal decreased dramatically. To test the channel's effect on this decrease, the channeling beam was omitted and just the 10 ps heating beam was injected into the plasma. In this scenario, significant fast electron production was once again observed on a similar scale to the results from the 3.04 ns injection time. This implied that the channel must have degraded significantly at these later times, likely through a combination of filamentation and hosing.

The parameter scan experiment featured in this chapter was designed based on these results. As stated in the analysis of the previous sections, the optimum channeling parameters were found when the pulse was focused at a low density, was of high intensity, and was injected into a hot plasma. This is because, when focused at a low density, the pulses possessed a higher intensity as they propagated through the majority of the plasma. This allowed the self-corrective behaviours discussed in Section 3.7 to take hold. By now being able to image the channel formation, the parameter scan cemented the conclusion that channel quality degrades as the plasma cools and expands which could only be inferred from the first fast ignition experiment. Further, it showed that the fast electron production of the 10 ps beam was less affected by the delay than the 100 ps beam, explaining why the heating-only shot was still able to produce fast electrons towards the compressed core.

A second fully-integrated fast ignition experiment was then conducted one week after the parameter scan. The data from the parameter scan experiment at this point in time had not been fully analysed, and so the only adjustment to the channeling beam was its timing with the drive pulses. A new drive profile was designed which lowered the implosion velocity and, in doing so, decreased the time between the end of the drive pulse and peak compression. With this new profile, peak areal density was expected to be achieved after 4.5 ns. The channeling and heating pulses were then injected at five times leading up to this point.

The fast electron spectra in this experiment were far more robust, only being slightly reduced as injection time was delayed. The most interesting results came from the on-axis spectra plotted in Figure 5.20. As can be seen here, the spectra experienced some depletion in the 1-3 MeV range. This reduction was present in neither the $\pm 5°$ nor the $\pm 10°$ spectrometers, and thus it is likely a result of the fast electrons collisionally depositing their energy in the compressed core as designed.

It should be noted that the neutron time-of-flight detector showed little increase with the inclusion of the channeling and heating beams in either experiment. However, this is a problem of total energy rather than channel direction. The timing dependence of the parameter scan did provide strong improvements to the channel formation in a fully-integrated scenario. Including the other findings of the scan, especially the focal position dependence, will likely provide even stronger results.

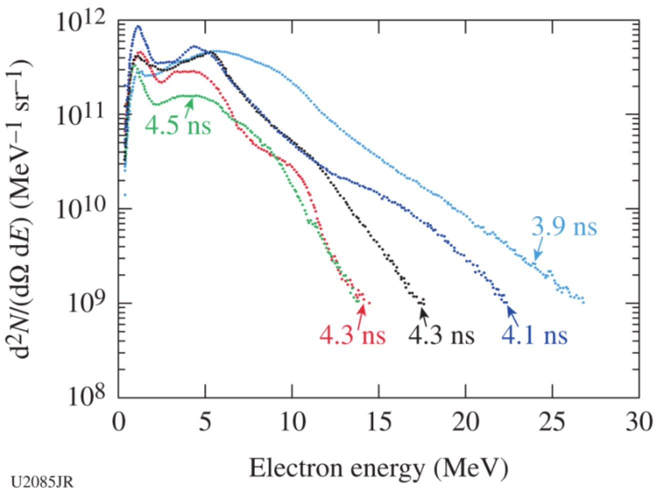

Figure 5.20: On-axis electron spectra for the second integrated fast ignition experiment. The spectra are plotted and are labeled with their corresponding channeling and heating beam injection times. Image reproduced with permission from LLE Review, Volume 148, p. 231.

Further, in central hot spot experiments, the mixing of any non-fuel elements into the compressed core greatly reduced the yield [125–127]. Thus, an experiment which uses an inner DT layer, rather than CD with Cu doping, will likely experience a more dramatic increase in fusion neutron yield, and the presence of the heating beam will have a larger effect. These experiments therefore lay out a promising foundation for continued fast ignition research.

6 Summary and Future Work

6.1 Summary of Results

This thesis has presented analytical, numerical, and experimental research focusing on high-intensity laser-plasma interactions and channeling.

Chapter 3 presented several simulations investigating various channeling schemes. Early simulations explored a new 'shoveling' pulse scheme and the effects of frequency on the hosing instability. The results pointed to a need to better understand the hosing instability at greater intensities and densities than has been previously examined in the literature. Consequently, an expanded physical model for relativistic laser channeling in plasmas was derived and verified against two-dimensional large-scale particle-in-cell simulations. The results show analytically for the first time that the effects of the hosing instability do indeed increase as a function of density. However, this is mitigated by the use of strongly relativistic laser pulses where enormous ponderomotive pressures are able to quickly self-correct the channel deviations.

This was illustrated throughout the channeling simulations of Section 3.5 which utilized highly relativistic ($a_0 = 20$) intensities. These simulations were initially designed to determine if the multiple pulse improvements found in References [90,91] can be realized on modern day facilities such as Vulcan Petawatt, OMEGA EP, and

NIF ARC. The results show that while the multiple pulse method is indeed effective with sufficiently short pulses, the duration and shape of the pulses required is not feasible with neodymium-based laser technology. In fact, using multiple pulses in this parameter regime can even worsen the levels of hosing due to the derived density dependence and the reduced levels of relativistically induced transparency that the rising and falling edges of the pulses experience.

Additionally, it has been shown that the ponderomotive force is great enough at these high intensities for the pulses to quickly self-correct, resulting in no appreciable displacement by the end of the simulation. This self-correction occurs faster at higher intensities, thereby reducing the energy losses to the hosed filaments. In this way, it differs from the refractive effects previously explored in the literature.

Further, the effects of the density profile on the hosing instability have been explored, showing that more curved profiles lead to additional hosing. This implies that larger-scale experiments which have more planar density profiles about the critical density should experience less hosing than their lower energy counterparts.

The coupled effects of intensity and external perturbations have been initially examined, though further work is required to obtain a more definitive explanation of these interactions. However, from these simulations, strong evidence has been found to suggest that filamentation, in addition to the causes discussed in Section 2.7.4, may be induced by the self-focusing of a pulse propagating through the plasma. This self-focusing leads to a beating of the pulse through self-interference which creates transverse intensity modulations. These modulations then ponderomotively create filaments within the density profile of the plasma.

Chapter 5 then presented the results of an OMEGA EP experiment designed to determine the optimum channeling parameters in an inhomogeneous plasma. The final density profile and channel formation was observed using a high-frequency transverse probe. The results showed that minimizing the delay between drive and channeling pulses is crucial for the formation of a controlled channel and maximizing its penetration into the plasma. Additionally, the channels deepened as pulses were focused at lower densities in the unperturbed plasma. Both of these results were consistent with previous experiments and the super-penetration (whole-beam self-focusing) schemes present in the literature.

The most surprising result of this experiment was the depth attained by high-intensity pulses. It was previously believed that high-intensity pulses would require more energy to penetrate through a plasma than their low-intensity energy-equivalents. However, the opposite trend was observed here. While it is difficult to say with certainty from this experiment, this was likely a result of three dimensional effects such as increased channel formation speed and ponderomotive pressures. More work, including full-scale three dimensional simulations, is required in order to confirm this as the root cause.

Interestingly as well, the first fully-integrated fast ignition experiment showed reduced fast electron production when the channeling and heating beams were targeted into the plasma at peak compression. However, when the channeling beam was removed, fast electron production rose to previous levels. This suggests that the low-intensity pulse was not able to successfully channel into the plasma and further supports the self-corrective behaviours observed in the channeling simulations by high-intensity pulses.

The results of the OMEGA EP experiment were partially implemented in a second fully-integrated fast ignition experiment which sought to improve the original experiment's channeling difficulties. By nearly eliminating the time between the end of the drive pulses and peak compression, the channeling beam was able to properly form through the plasma, and the heating beam sent fast electrons towards the compressed core where they collisionally deposited their energy. This is an important step forward in fast ignition research.

6.2 Future Work

As discussed in Section 3.6, additional work is planned to complete the exploration of the effects of external density modulations on pulses of varying intensities. Due to limited computational resources, the initial simulations had to be shortened in order to obtain useful results, though it was not possible to run every simulation. Once more resources become available, the initial simulations with a Gaussian perturbation will be completed. Those with interesting results – likely those at strongly relativistic intensities ($a_0 = 10 - 30$) – will be compared and possibly expanded by increasing the size and amplitude of the perturbation. Other perturbation profiles will also be investigated such as sinusoidal noise. This may also be explored experimentally by propagating a channeling beam through a turbulent plasma, possibly generated through two colliding plasma plumes.

Furthermore, a study of the "pathfinder" pulses seen throughout Chapter 3 will be conducted in order to better understand the physical mechanism behind this phenomenon. These pulses could be used to seed a guiding path for more intense pulses. However, due to the low energy and narrow profiles of the pathfinder seeds, high-intensity pulses would still be necessary in order to fully expel the plasma and generate a much wider channel. A full numerical investigation will be conducted to examine the feasibility and robustness of this scheme. Should the results be promising, this could then be extended experimentally through the use of low-energy, ultrashort (femtosecond-scale) Ti:sapphire beams as the pathfinder seeds while a high-energy neodymium-based beam could act as the primary channeler.

A large simulation campaign is additionally being designed to explore the channeling quality of orbital angular momentum pulses. These pulses have twisted wavefronts which gives them unique properties that could yield interesting results for channeling. Their polarisation profiles are axisymmetric which would theoretically reduce the levels of hosing seen during the pulse's propagation. By coupling to the high-density electron sheath, the electric field of a linear pulse causes density shifts at the head of the channel. This leads to the antisymmetric surface waves seen in p-polarisation simulations and short-wavelength hosing. These surface waves then create the initial centroid displacement required for runaway hosing as derived in Section 3.3. However, if the electric field were to be axisymmetric, this effect would be mitigated.

Perhaps a more obvious property of orbital angular momentum pulses is their torus-shaped transverse profile. The helical nature of the pulses' wavefronts necessitates zero intensity in their centre. Using these pulses to channel would then effectively form an *in situ* high-density wire within a plasma. It has been well-established that electrons may be collimated when propagating through similar structures [128–130]. By combining Faraday's law with Ohm's law, it may be shown that $\partial_t \mathbf{B} \propto n_e \boldsymbol{\nabla} \times \mathbf{v}_e + (\boldsymbol{\nabla} n_e) \times \mathbf{v}_e$. This second term shows that magnetic fields will be formed as electrons propagate across a strong density gradient such as that at the edge of a high-density wire. The orientation of these fields is appropriate to collimate the electrons. It is this mechanism which leads to the electron collimation seen in the literature which has been explored through the use of prefabricated targets. However, after an capsule has been imploded for fast ignition inertial confinement fusion, any preformed structure will have been destroyed. This requires elaborate setups with a second target in place which is used to form fast electrons. Having the capability to quickly generate these structures *in situ* would then ease the geometrical requirements of these experiments and increase the overall efficiency of the ignition stage. Therefore, research into orbital angular momentum pulses could yield important results for fast ignition. Unfortunately, these simulations by nature must be three dimensional and thus require tremendous amounts of computational power. Thus an incremental approach to this research must be taken if it is to be explored numerically, though experimental research could prove more fruitful in the near-term. Experimental proposals are already being written to explore these pulses' interaction with plasmas.

In conclusion, all of the research presented here is in line with the physical models discussed in this thesis and shows that increasing the laser intensity of the channeling pulse is a viable approach to channeling and hole-boring. Higher intensity pulses are seen in simulations to swiftly self-correct and are theoretically capable of overcoming external density asymmetries. The experiments showed them to be capable of forming more reliable, deeper channels. This is all in addition to previously published benefits such as their ability to seed magnetic fields which help collimate the fast electrons generated by heating beams. Thus, they form promising candidates for full-scale, fully-integrated fast ignition experiments and highlight the need for further development of this branch of relativistic high-energy-density physics research.

Appendices

A
Dimensionless Normalizations

At various points throughout this work, analysis is performed using dimensionless variables. For easy referencing, the below list summarizes the normalizations involved in this process.

$$
\begin{aligned}
\mathbf{A} &\rightarrow \frac{e\mathbf{A}}{mc} \\
\mathbf{B} &\rightarrow \frac{e\mathbf{B}}{m\omega} \\
\mathbf{E} &\rightarrow \frac{e\mathbf{E}}{mc\omega} \\
n &\rightarrow \frac{n}{n_c} \\
\mathbf{p} &\rightarrow \frac{\mathbf{p}}{mc} \\
t &\rightarrow \omega t \\
T &\rightarrow \frac{k_B T}{mc^2} \\
\mathbf{v} &\rightarrow \frac{\mathbf{v}}{c} \\
x &\rightarrow kx \\
\Phi &\rightarrow \frac{e\Phi}{mc^2}
\end{aligned}
$$

Bibliography

[1] S. Atzeni and J. Meyer-ter Vehn, *The Physics of Inertial Fusion*. Oxford University Press (2004).

[2] NIST, *Atomic Weights and Isotopic Compositions for All Elements. https://physics.nist.gov*.

[3] J. D. Lawson, *Some Criteria for a Power Producing Thermonuclear Reactor*. Proceedings of the Physical Society. Section B, **70(1)**, 6 (1957).

[4] H. Takabe, K. Mima, L. Montierth, and R. L. Morse, *Self-consistent growth rate of the Rayleigh–Taylor instability in an ablatively accelerating plasma*. Physics of Fluids, **28(12)**, 3676 (1985).

[5] S. P. Regan, D. K. Bradley, A. V. Chirokikh, R. S. Craxton, D. D. Meyerhofer, W. Seka, R. W. Short, A. Simon, R. P. J. Town, B. Yaakobi, J. J. Carroll, and R. P. Drake, *Laser-plasma interactions in long-scale-length plasmas under direct-drive National Ignition Facility conditions*. Physics of Plasmas, **6(5)**, 2072 (1999).

[6] I. V. Igumenshchev, A. B. Zylstra, C. K. Li, P. M. Nilson, V. N. Goncharov, and R. D. Petrasso, *Self-generated magnetic fields in direct-drive implosion experiments*. Physics of Plasmas, **21(6)**, 062707 (2014).

[7] R. L. McCrory, D. D. Meyerhofer, R. Betti, R. S. Craxton, J. A. Delettrez, D. H. Edgell, V. Y. Glebov, V. N. Goncharov, D. R. Harding, D. W. Jacobs-Perkins, J. P. Knauer, F. J. Marshall, P. W. McKenty, P. B. Radha, S. P. Regan, T. C. Sangster, W. Seka, R. W. Short, S. Skupsky, V. A. Smalyuk, J. M. Soures, C. Stoeckl, B. Yaakobi, D. Shvarts, J. A. Frenje, C. K. Li, R. D. Petrasso, and F. H. Seguin, *Progress in direct-drive inertial confinement fusion*. Physics of Plasmas, **15(5)**, 055503 (2008).

[8] R. S. Craxton, K. S. Anderson, T. R. Boehly, V. N. Goncharov, D. R. Harding, J. P. Knauer, R. L. McCrory, P. W. McKenty, D. D. Meyerhofer, J. F. Myatt, A. J. Schmitt, J. D. Sethian, R. W. Short, S. Skupsky, W. Theobald, W. L. Kruer, K. A. Tanaka, R. Betti, T. J. B. Collins, J. A. Delettrez, S. X. Hu, J. A. Marozas, A. V. Maximov, D. T. Michel, P. B. Radha, S. P. Regan, T. C. Sangster, W. Seka, A. A. Solodov, J. M. Soures, C. Stoeckl, and J. D. Zuegel, *Direct-drive inertial confinement fusion: A review*. Physics of Plasmas, **22(11)**, 110501 (2015).

[9] R. Betti and O. A. Hurricane, *Inertial-confinement fusion with lasers*. Nature Physics, **12**, 435 (2016).

[10] R. Kulsrud, E. Valeo, and S. Cowley, *Physics of spin-polarized plasmas*. Nuclear Fusion, **26(11)**, 1443 (1986).

[11] R. E. Brown, N. Jarmie, and R. A. Hardekopf, *Nuclear Reactions among the Hydrogen Isotopes at Low Energies.* IEEE Transactions on Nuclear Science, **30(2)**, 1164 (1983).

[12] O. A. Hurricane, D. A. Callahan, D. T. Casey, P. M. Celliers, C. J. Cerjan, E. L. Dewald, T. R. Dittrich, T. Döppner, D. E. Hinkel, L. F. B. Hopkins, J. L. Kline, S. Le Pape, T. Ma, A. G. MacPhee, J. L. Milovich, A. Pak, H.-S. Park, P. K. Patel, B. A. Remington, J. D. Salmonson, P. T. Springer, and R. Tommasini, *Fuel gain exceeding unity in an inertially confined fusion implosion.* Nature, **506(7488)**, 343 (2014).

[13] S. P. Regan, R. Epstein, B. A. Hammel, L. J. Suter, H. A. Scott, M. A. Barrios, D. K. Bradley, D. A. Callahan, C. Cerjan, G. W. Collins, S. N. Dixit, T. Döppner, M. J. Edwards, D. R. Farley, K. B. Fournier, S. Glenn, S. H. Glenzer, I. E. Golovkin, S. W. Haan, A. Hamza, D. G. Hicks, N. Izumi, O. S. Jones, J. D. Kilkenny, J. L. Kline, G. A. Kyrala, O. L. Landen, T. Ma, J. J. MacFarlane, A. J. MacKinnon, R. C. Mancini, R. L. McCrory, N. B. Meezan, D. D. Meyerhofer, A. Nikroo, H.-S. Park, J. Ralph, B. A. Remington, T. C. Sangster, V. A. Smalyuk, P. T. Springer, and R. P. J. Town, *Hot-Spot Mix in Ignition-Scale Inertial Confinement Fusion Targets.* Physical Review Letters, **111(4)**, 045001 (2013).

[14] D. Kang, S. Zhu, W. Pei, S. Zou, W. Zheng, J. Gu, and Z. Dai, *Improving hot-spot pressure for ignition in high-adiabat Inertial Confinement Fusion implosion.* arXiv, 1–5 (2017).

[15] T. Ma, P. K. Patel, N. Izumi, P. T. Springer, M. H. Key, L. J. Atherton, M. A. Barrios, L. R. Benedetti, R. Bionta, E. Bond, D. K. Bradley, J. Caggiano, D. A. Callahan, D. T. Casey, P. M. Celliers, C. J. Cerjan, J. A. Church, D. S. Clark, E. L. Dewald, T. R. Dittrich, S. N. Dixit, T. Döppner, R. Dylla-Spears, D. H. Edgell, R. Epstein, J. Field, D. N. Fittinghoff, J. A. Frenje, M. Gatu Johnson, S. Glenn, S. H. Glenzer, G. Grim, N. Guler, S. W. Haan, B. A. Hammel, R. Hatarik, H. W. Herrmann, D. Hicks, D. E. Hinkel, L. F. Berzak Hopkins, W. W. Hsing, O. A. Hurricane, O. S. Jones, R. Kauffman, S. F. Khan, J. D. Kilkenny, J. L. Kline, B. Kozioziemski, A. Kritcher, G. A. Kyrala, O. L. Landen, J. D. Lindl, S. Le Pape, B. J. MacGowan, A. J. Mackinnon, A. G. MacPhee, N. B. Meezan, F. E. Merrill, J. D. Moody, E. I. Moses, S. R. Nagel, A. Nikroo, A. Pak, T. Parham, H.-S. Park, J. E. Ralph, S. P. Regan, B. A. Remington, H. F. Robey, M. D. Rosen, J. R. Rygg, J. S. Ross, J. D. Salmonson, J. Sater, D. Sayre, M. B. Schneider, D. Shaughnessy, H. Sio, B. K. Spears, V. Smalyuk, L. J. Suter, R. Tommasini, R. P. J. Town, P. L. Volegov, A. Wan, S. V. Weber, K. Widmann, C. H. Wilde, C. Yeamans, and M. J. Edwards, *The role of hot spot mix in the low-foot and high-foot implosions on the NIF.* Physics of Plasmas, **24(5)**, 056311 (2017).

[16] T. Ma, P. K. Patel, N. Izumi, P. T. Springer, M. H. Key, L. J. Atherton, L. R. Benedetti, D. K. Bradley, D. A. Callahan, P. M. Celliers, C. J. Cerjan, D. S. Clark, E. L. Dewald, S. N. Dixit, T. Döppner, D. H. Edgell, R. Epstein, S. Glenn, G. P. Grim, S. W. Haan, B. A. Hammel, D. Hicks, W. W. Hsing, O. S. Jones, S. F. Khan, J. D. Kilkenny, J. L. Kline, G. A. Kyrala, O. L. Landen, S. Le Pape, B. J. MacGowan, A. J. Mackinnon, A. G. MacPhee, N. B. Meezan, J. D. Moody, A. Pak, T. Parham, H.-S. Park, J. E. Ralph, S. P. Regan, B. A. Remington, H. F. Robey, J. S. Ross, B. K. Spears, V. A. Smalyuk, L. J. Suter, R. Tommasini, R. P. Town, S. V. Weber, J. D. Lindl, M. J. Edwards, S. H. Glenzer, and E. I. Moses, *Onset of Hydrodynamic Mix in High-Velocity, Highly Compressed Inertial Confinement Fusion Implosions.* Physical Review Letters, **111(8)**, 085004 (2013).

[17] H.-S. Park, O. A. Hurricane, D. A. Callahan, D. T. Casey, E. L. Dewald, T. R. Dittrich, T. Döppner, D. E. Hinkel, L. F. Berzak Hopkins, S. Le Pape, T. Ma, P. K. Patel, B. A. Remington, H. F. Robey, J. D. Salmonson, and J. L. Kline, *High-Adiabat High-Foot Inertial Confinement Fusion Implosion Experiments on the National Ignition Facility.* Physical Review Letters, **112(5)**, 055001 (2014).

[18] M. Tabak, J. Hammer, M. E. Glinsky, W. L. Kruer, S. C. Wilks, J. Woodworth, E. M. Campbell, M. D. Perry, and R. J. Mason, *Ignition and high gain with ultrapowerful lasers.* Physics of Plasmas, **1(5)**, 1626 (1994).

[19] R. Betti, K. S. Anderson, J. P. Knauer, T. J. B. Collins, R. L. McCrory, P. W. McKenty, and S. Skupsky, *Theory of laser-induced adiabat shaping in inertial fusion implosions: The relaxation method.* Physics of Plasmas, **12(4)**, 042703 (2005).

[20] S. E. Bodner, A. J. Schmitt, and J. D. Sethian, *Laser requirements for a laser fusion energy power plant.* High Power Laser Science and Engineering, **1(01)**, 2 (2013).

[21] R. Betti and C. Zhou, *High-density and high-ρR fuel assembly for fast-ignition inertial confinement fusion.* Physics of Plasmas, **12(11)**, 110702 (2005).

[22] H.-B. Cai, S.-Z. Wu, J.-F. Wu, M. Chen, H. Zhang, M.-Q. He, L.-H. Cao, C.-T. Zhou, S.-P. Zhu, and X.-T. He, *Review of the current status of fast ignition research at the IAPCM.* High Power Laser Science and Engineering, **2**, e6 (2014).

[23] R. Kodama, P. A. Norreys, K. Mima, A. E. Dangor, R. G. Evans, H. Fujita, Y. Kitagawa, K. M. Krushelnick, T. Miyakoshi, N. Miyanaga, T. Norimatsu, S. J. Rose, T. Shozaki, K. Shigemori, A. Sunahara, M. Tampo, K. A. Tanaka, Y. Toyama, T. Yamanaka, and M. Zepf, *Fast heating of ultrahigh-density plasma as a step towards laser fusion ignition.* Nature, **412(6849)**, 798 (2001).

[24] A. J. Kemp, F. Fiuza, A. Debayle, T. Johzaki, W. B. Mori, P. K. Patel, Y. Sentoku, and L. O. Silva, *Laser–plasma interactions for fast ignition.* Nuclear Fusion, **54(5)**, 054002 (2014).

[25] X. Liu and D. Umstadter, *Competition between ponderomotive and thermal forces in short-scale-length laser plasmas.* Physical Review Letters, **69(13)**, 1935 (1992).

[26] A. B. Borisov, A. V. Borovskiy, V. Korobkin, A. M. Prokhorov, O. B. Shiryaev, X. M. Shi, T. S. Luk, A. McPherson, J. C. Solem, K. Boyer, and C. K. Rhodes, *Observation of relativistic and charge-displacement self-channeling of intense subpicosecond ultraviolet (248 nm) radiation in plasmas.* Physical Review Letters, **68(15)**, 2309 (1992).

[27] C. G. Durfee and H. M. Milchberg, *Light pipe for high intensity laser pulses.* Physical Review Letters, **71(15)**, 2409 (1993).

[28] G. Li, R. Yan, C. Ren, T.-L. Wang, J. Tonge, and W. B. Mori, *Laser Channeling in Millimeter-Scale Underdense Plasmas of Fast-Ignition Targets.* Physical Review Letters, **100(12)**, 125002 (2008).

[29] R. Kodama, H. Shiraga, K. Shigemori, Y. Toyama, S. Fujioka, H. Azechi, H. Fujita, H. Habara, T. Hall, Y. Izawa, T. Jitsuno, Y. Kitagawa, K. M. Krushelnick, K. L. Lancaster, K. Mima, K. Nagai, M. Nakai, H. Nishimura, T. Norimatsu, P. A. Norreys, S. Sakabe, K. A. Tanaka, A. Youssef, M. Zepf, and T. Yamanaka, *Nuclear fusion: Fast heating scalable to laser fusion ignition.* Nature, **418(6901)**, 933 (2002).

[30] N. Booth, R. J. Clarke, D. Doria, L. A. Gizzi, G. Gregori, P. Hakel, P. Koester, L. Labate, T. Levato, B. Li, M. Makita, R. Mancini, J. Pasley, P. Rajeev, D. Riley, A. P. L. Robinson, E. Wagenaars, J. Waugh, and N. C. Woolsey, *Measuring fast electron distribution functions at intensities up to 1021Wcm-2.* Nuclear Instruments and Methods in Physics Research Section A: Accelerators, Spectrometers, Detectors and Associated Equipment, **653(1)**, 137 (2011).

[31] J. S. Green, V. M. Ovchinnikov, R. G. Evans, K. U. Akli, H. Azechi, F. N. Beg, C. Bellei, R. R. Freeman, H. Habara, R. Heathcote, M. H. Key, J. A. King, K. L. Lancaster, N. Lopes, T. Ma, A. J. MacKinnon, K. Markey, A. McPhee, Z. Najmudin, P. M. Nilson, R. Onofrei, R. B. Stephens, K. Takeda, K. A. Tanaka, W. Theobald, T. Tanimoto, J. Waugh, L. D. Van Woerkom, N. C. Woolsey, M. Zepf, J. R. Davies, and P. A. Norreys, *Effect of Laser Intensity on Fast-Electron-Beam Divergence in Solid-Density Plasmas.* Physical Review Letters, **100(1)**, 015003 (2008).

[32] R. Kodama, Y. Sentoku, Z. L. Chen, G. R. Kumar, S. P. Hatchett, Y. Toyama, T. E. Cowan, R. R. Freeman, J. Fuchs, Y. Izawa, M. H. Key, Y. Kitagawa, K. Kondo, T. Matsuoka, H. Nakamura, M. Nakatsutsumi, P. A. Norreys, T. Norimatsu, R. A. Snavely, R. B. Stephens, M. Tampo, K. A. Tanaka, and T. Yabuuchi, *Plasma devices to guide and collimate a high density of MeV electrons.* Nature, **432(7020)**, 1005 (2004).

[33] L. Labate, E. Förster, A. Giulietti, D. Giulietti, S. Höfer, T. Kämpfer, P. Köster, M. Kozlova, T. Levato, R. Lötzsch, A. Lübcke, T. Mocek, J. Polan, B. Rus, I. Uschmann, F. Zamponi, and L. A. Gizzi, *Experimental investigation of fast electron transport in solid density matter: Recent results from a new technique of X-ray energy-encoded 2D imaging.* Laser and Particle Beams, **27(04)**, 643 (2009).

[34] R. H. H. Scott, F. Perez, J. J. Santos, C. P. Ridgers, J. R. Davies, K. L. Lancaster, S. D. Baton, P. Nicolai, R. M. G. M. Trines, A. R. Bell, S. Hulin, M. Tzoufras, S. J. Rose, and P. A. Norreys, *A study of fast electron energy transport in relativistically intense laser-plasma interactions with large density scalelengths.* Physics of Plasmas, **19(5)**, 053104 (2012).

[35] L. Volpe, J.-L. Feugeas, P. Nicolai, J. J. Santos, M. Touati, J. Breil, D. Batani, and V. T. Tikhonchuk, *Controlling the fast electron divergence in a solid target with multiple laser pulses.* Physical Review E, **90(6)**, 063108 (2014).

[36] P. E. Young, M. E. Foord, J. H. Hammer, W. L. Kruer, M. Tabak, and S. C. Wilks, *Time-Dependent Channel Formation in a Laser-Produced Plasma.* Physical Review Letters, **75(6)**, 1082 (1995).

[37] K. A. Tanaka, H. Hashimoto, R. Kodama, K. Mima, Y. Sentoku, and K. Takahashi, *Performance comparison of self-focusing with 1053- and 351-nm laser pulses.* Physical Review E, **60(3)**, 3283 (1999).

[38] M. Borghesi, A. J. MacKinnon, L. Barringer, R. Gaillard, L. A. Gizzi, C. Meyer, O. Willi, A. Pukhov, and J. Meyer-ter Vehn, *Relativistic Channeling of a Picosecond Laser Pulse in a Near-Critical Preformed Plasma.* Physical Review Letters, **78(5)**, 879 (1997).

[39] J. Fuchs, J. C. Adam, F. Amiranoff, S. D. Baton, P. Gallant, L. Gremillet, A. Héron, J. C. Kieffer, G. Laval, G. Malka, J. L. Miquel, P. Mora, H. Pépin, and C. Rousseaux, *Transmission through Highly Overdense Plasma Slabs with a Subpicosecond Relativistic Laser Pulse.* Physical Review Letters, **80(11)**, 2326 (1998).

[40] Z. Najmudin, K. M. Krushelnick, M. Tatarakis, E. L. Clark, C. N. Danson, V. Malka, D. Neely, M. I. K. Santala, and A. E. Dangor, *The effect of high intensity laser propagation instabilities on channel formation in underdense plasmas.* Physics of Plasmas, **10(2)**, 438 (2003).

[41] L. Ceurvorst, N. Ratan, M. C. Levy, M. F. Kasim, J. Sadler, R. H. H. Scott, R. M. G. M. Trines, T. W. Huang, M. Skramic, M. Vranic, L. O. Silva, and P. A. Norreys, *Mitigating the hosing instability in relativistic laser-plasma interactions.* New Journal of Physics, **18(5)**, 053023 (2016).

[42] R. A. Fonseca, L. O. Silva, F. S. Tsung, V. K. Decyk, W. Lu, C. Ren, W. B. Mori, S. Deng, and S. Lee, *OSIRIS: A three-dimensional, fully relativistic particle in cell code for modeling plasma based accelerators.* In *Computational Science-ICCS, Pt III, Proceedings, Lecture Notes in Computer Science*, volume 2331, 342–351, Springer, Berlin (2002).

[43] M. M. Marinak, G. D. Kerbel, N. A. Gentile, O. Jones, D. Munro, S. Pollaine, T. R. Dittrich, and S. W. Haan, *Three-dimensional HYDRA simulations of National Ignition Facility targets.* Physics of Plasmas, **8(5)**, 2275 (2001).

[44] B. Fryxell, K. Olson, P. Ricker, F. X. Timmes, M. Zingale, D. Q. Lamb, P. MacNeice, R. Rosner, J. W. Truran, and H. Tufo, *FLASH: An Adaptive Mesh Hydrodynamics Code for Modeling Astrophysical Thermonuclear Flashes.* The Astrophysical Journal Supplement Series, **131(1)**, 273 (2000).

[45] D. Haberberger, S. Ivancic, S. X. Hu, R. Boni, M. Barczys, R. S. Craxton, and D. H. Froula, *Measurements of electron density profiles using an angular filter refractometer.* Physics of Plasmas, **21(5)**, 056304 (2014).

[46] F. F. Chen, *Introduction to Plasma Physics and Controlled Fusion.* Springer US, Boston, MA, 2 edition (1984).

[47] P. Gibbon, *Short Pulse Laser Interactions with Matter.* Imperial College Press, London (2005).

[48] F. Cattani, A. Kim, D. Anderson, and M. Lisak, *Multifilament structures in relativistic self-focusing.* Physical Review E, **64(1)**, 016412 (2001).

[49] A. Kim, M. Tushentsov, F. Cattani, D. Anderson, and M. Lisak, *Axisymmetric relativistic self-channeling of laser light in plasmas.* Physical Review E, **65(3)**, 036416 (2002).

[50] A. Pukhov and J. Meyer-ter Vehn, *Relativistic Magnetic Self-Channeling of Light in Near-Critical Plasma: Three-Dimensional Particle-in-Cell Simulation.* Physical Review Letters, **76(21)**, 3975 (1996).

[51] F. Brunel, *Not-so-resonant, resonant absorption*. Physical Review Letters, **59(1)**, 52 (1987).

[52] D. Bauer and P. Mulser, *Vacuum heating versus skin layer absorption of intense femtosecond laser pulses*. Physics of Plasmas, **14(2)**, 023301 (2007).

[53] D. Bauer, P. Mulser, and W.-H. Steeb, *Relativistic Ponderomotive Force, Uphill Acceleration, and Transition to Chaos*. Physical Review Letter, **75(25)**, 4622 (1995).

[54] W. M. Manheimer, *A covariant derivation of the ponderomotive force*. Physics of Fluids, **28(5)**, 1569 (1985).

[55] J. Colvin and J. Larsen, *Extreme Physics*. Cambridge University Press, Cambridge (2014).

[56] L. V. Keldysh, *Ionization in the field of a strong electromagnetic wave*. Soviet Physics JETP, **20(5)**, 1307 (1965).

[57] W. L. Kruer, *The Physics of Laser Plasma Interactions*. Westview Press, Boulder, CO (2003).

[58] G. S. Sarkisov, V. Y. Bychenkov, V. N. Novikov, V. T. Tikhonchuk, A. Maksimchuk, S.-Y. Chen, R. Wagner, G. Mourou, and D. Umstadter, *Self-focusing, channel formation, and high-energy ion generation in interaction of an intense short laser pulse with a He jet*. Physical Review E, **59(6)**, 7042 (1999).

[59] K. Krushelnick, E. L. Clark, Z. Najmudin, M. Salvati, M. I. K. Santala, M. Tatarakis, a. E. Dangor, V. Malka, D. Neely, R. Allott, and C. Danson, *Multi-MeV Ion Production from High-Intensity Laser Interactions with Underdense Plasmas*. Physical Review Letters, **83(4)**, 737 (1999).

[60] K. M. Krushelnick, A. Ting, C. I. Moore, H. R. Burris, E. Esarey, P. Sprangle, and M. Baine, *Plasma Channel Formation and Guiding during High Intensity Short Pulse Laser Plasma Experiments*. Physical Review Letters, **78(21)**, 4047 (1997).

[61] N. M. Naumova, J. Koga, K. Nakajima, T. Tajima, T. Z. Esirkepov, S. V. Bulanov, and F. Pegoraro, *Polarization, hosing and long time evolution of relativistic laser pulses*. Physics of Plasmas, **8(9)**, 4149 (2001).

[62] S. V. Bulanov, I. N. Inovenkov, V. I. Kirsanov, N. M. Naumova, and A. S. Sakharov, *Nonlinear depletion of ultrashort and relativistically strong laser pulses in an underdense plasma*. Physics of Fluids B: Plasma Physics, **4(7)**, 1935 (1992).

[63] L. Willingale, A. G. R. Thomas, P. M. Nilson, H. Chen, J. Cobble, R. S. Craxton, A. Maksimchuk, P. A. Norreys, T. C. Sangster, R. H. H. Scott, C. Stoeckl, C. Zulick, and K. M. Krushelnick, *Surface waves and electron acceleration from high-power, kilojoule-class laser interactions with underdense plasma*. New Journal of Physics, **15(2)**, 025023 (2013).

[64] S. V. Bulanov, T. Z. Esirkepov, N. M. Naumova, F. Pegoraro, and V. A. Vshivkov, *Solitonlike Electromagnetic Waves behind a Superintense Laser Pulse in a Plasma*. Physical Review Letters, **82(17)**, 3440 (1999).

[65] D. Farina and S. V. Bulanov, *Slow electromagnetic solitons in electron-ion plasmas*. Plasma Physics Reports, **27(8)**, 641 (2001).

[66] T. Esirkepov, K. Nishihara, S. V. Bulanov, and F. Pegoraro, *Three-Dimensional Relativistic Electromagnetic Subcycle Solitons*. Physical Review Letters, **89(27)**, 275002 (2002).

[67] V. A. Mironov, N. Zharova, E. D'Humières, R. Capdessus, and V. T. Tikhonchuk, *Effect of the laser pulse temporal shape on the hole boring efficiency*. Plasma Physics and Controlled Fusion, **54(9)**, 095008 (2012).

[68] D. K. Singh, J. R. Davies, G. Sarri, F. Fiuza, and L. O. Silva, *Dynamics of intense laser propagation in underdense plasma: Polarization dependence*. Physics of Plasmas, **19(7)**, 073111 (2012).

[69] N. M. Naumova, S. V. Bulanov, T. Z. Esirkepov, D. Farina, K. Nishihara, F. Pegoraro, H. Ruhl, and A. S. Sakharov, *Formation of Electromagnetic Postsolitons in Plasmas*. Physical Review Letters, **87(18)**, 185004 (2001).

[70] R. Bingham, R. Short, E. Williams, D. Villeneuve, and M. C. Richardson, *The filamentation instability at short wavelengths*. Plasma Physics and Controlled Fusion, **26(9)**, 1077 (1984).

[71] S. C. Wilks, W. L. Kruer, M. Tabak, and A. B. Langdon, *Absorption of ultra-intense laser pulses*. Physical Review Letters, **69(9)**, 1383 (1992).

[72] A. P. L. Robinson, P. Gibbon, M. Zepf, S. Kar, R. G. Evans, and C. Bellei, *Relativistically correct hole-boring and ion acceleration by circularly polarized laser pulses*. Plasma Physics and Controlled Fusion, **51(2)**, 024004 (2009).

[73] Y. Ping, A. J. Kemp, L. Divol, M. H. Key, P. K. Patel, K. U. Akli, F. N. Beg, S. Chawla, C. D. Chen, R. R. Freeman, D. Hey, D. P. Higginson, L. C. Jarrott, G. E. Kemp, A. Link, H. S. McLean, H. Sawada, R. B. Stephens, D. Turnbull, B. Westover, and S. C. Wilks, *Dynamics of Relativistic Laser-Plasma Interaction on Solid Targets*. Physical Review Letters, **109(14)**, 145006 (2012).

[74] L. Willingale, S. R. Nagel, A. G. R. Thomas, C. Bellei, R. J. Clarke, A. E. Dangor, R. Heathcote, M. C. Kaluza, C. Kamperidis, S. Kneip, K. M. Krushelnick, N. Lopes, S. P. D. Mangles, W. Nazarov, P. M. Nilson, and Z. Najmudin, *Characterization of High-Intensity Laser Propagation in the Relativistic Transparent Regime through Measurements of Energetic Proton Beams*. Physical Review Letters, **102(12)**, 125002 (2009).

[75] G. Sarri, D. K. Singh, J. R. Davies, F. Fiuza, K. L. Lancaster, E. L. Clark, S. Hassan, J. Jiang, N. Kageiwa, N. Lopes, A. Rehman, C. Russo, R. H. H. Scott, T. Tanimoto, Z. Najmudin, K. A. Tanaka, M. Tatarakis, M. Borghesi, and P. A. Norreys, *Observation of Postsoliton Expansion Following Laser Propagation through an Underdense Plasma*. Physical Review Letters, **105(17)**, 175007 (2010).

[76] G. Sarri, S. Kar, L. Romagnani, S. V. Bulanov, C. A. Cecchetti, M. Galimberti, L. A. Gizzi, R. Heathcote, R. Jung, I. Kourakis, J. Osterholz, A. Schiavi, O. Willi, and M. Borghesi, *Observation of plasma density dependence of electromagnetic soliton excitation by an intense laser pulse*. Physics of Plasmas, **18(8)**, 080704 (2011).

[77] *ARCHER UK National Supercomputing Services. http://www.archer.ac.uk.*

[78] C. K. Birdsall and A. B. Langdon, *Plasma Physics via Computer Simulation.* Institute of Physics Publishing, Bristol (2005).

[79] C. Ren and W. B. Mori, *Physical picture for the laser hosing instability in a plasma.* Physics of Plasmas, **8(6)**, 3118 (2001).

[80] S. V. Bulanov and F. Pegoraro, *Stability of a mass accreting shell expanding in a plasma.* Physical Review E, **65(6)**, 066405 (2002).

[81] N. Naseri, S. G. Bochkarev, and W. Rozmus, *Self-channelling of relativistic laser pulses in large-scale underdense plasmas.* Physics of Plasmas, **17(3)**, 033107 (2010).

[82] H. Habara, K. Adumi, T. Yabuuchi, T. Nakamura, Z. L. Chen, M. Kashihara, R. Kodama, K. Kondo, G. R. Kumar, L. A. Lei, T. Matsuoka, K. Mima, and K. A. Tanaka, *Surface Acceleration of Fast Electrons with Relativistic Self-Focusing in Preformed Plasma.* Physical Review Letters, **97(9)**, 095004 (2006).

[83] P. Sprangle, C.-M. Tang, and E. Esarey, *Relativistic Self-Focusing of Short-Pulse Radiation Beams in Plasmas.* IEEE Transactions on Plasma Science, **15(2)**, 145 (1987).

[84] J. M. Dias, C. Stenz, N. Lopes, X. Badiche, F. Blasco, A. Dos Santos, L. Oliveira e Silva, A. Mysyrowicz, A. Antonetti, and J. T. Mendonça, *Experimental Evidence of Photon Acceleration of Ultrashort Laser Pulses in Relativistic Ionization Fronts.* Physical Review Letters, **78(25)**, 4773 (1997).

[85] E. M. Epperlein, *Kinetic theory of laser filamentation in plasmas.* Physical Review Letters, **65(17)**, 2145 (1990).

[86] W. B. Mori, *The physics of the nonlinear optics of plasmas at relativistic intensities for short-pulse lasers.* IEEE Journal of Quantum Electronics, **33(11)**, 1942 (1997).

[87] D. W. Forslund, J. M. Kindel, and E. L. Lindman, *Plasma simulation studies of stimulated scattering processes in laser-irradiated plasmas.* Physics of Fluids, **18(8)**, 1017 (1975).

[88] M. C. Kaluza, S. P. D. Mangles, A. G. R. Thomas, Z. Najmudin, A. E. Dangor, C. D. Murphy, J. L. Collier, E. J. Divall, P. S. Foster, C. J. Hooker, A. J. Langley, J. Smith, and K. M. Krushelnick, *Observation of a Long-Wavelength Hosing Modulation of a High-Intensity Laser Pulse in Underdense Plasma.* Physical Review Letters, **105(9)**, 095003 (2010).

[89] B. J. Duda, R. G. Hemker, K. C. Tzeng, and W. B. Mori, *A Long-Wavelength Hosing Instability in Laser-Plasma Interactions.* Physical Review Letters, **83(10)**, 1978 (1999).

[90] A. L. Lei, K. A. Tanaka, R. Kodama, K. Adumi, H. Habara, Y. Kitagawa, K. Kondo, T. Matsuoka, T. Tanimoto, T. Yabuuchi, K. Mima, K. Nagai, H. Nagatomo, T. Norimatsu, K. Sawai, K. Suzuki, W. Yu, H. Xu, X. Q. Yang, L.-h. Cao, H.-b. Cai, Y. Sentoku, A. Pukhov, R. Kumar, R. A. Snavely, R. R. Freeman, M. Yu, and J. Zheng, *Study of ultraintense laser propagation in overdense plasmas for fast ignition.* Physics of Plasmas, **16(5)**, 056307 (2009).

[91] W. Yu, L.-h. Cao, M. Y. Yu, H.-b. Cai, H. Xu, X. Yang, A. Lei, K. A. Tanaka, and R. Kodama, *Plasma channeling by multiple short-pulse lasers.* Laser and Particle Beams, **27(01)**, 109 (2009).

[92] T. Matsuoka, A. Lei, T. Yabuuchi, K. Adumi, J. Zheng, R. Kodama, K. Sawai, K. Suzuki, Y. Kitagawa, T. Norimatsu, K. Nagai, H. Nagatomo, Y. Izawa, K. Mima, Y. Sentoku, and K. A. Tanaka, *Focus optimization of relativistic self-focusing for anomalous laser penetration into overdense plasmas (super-penetration).* Plasma Physics and Controlled Fusion, **50(10)**, 105011 (2008).

[93] C. D. Murphy, R. M. G. M. Trines, J. Vieira, A. J. W. Reitsma, R. Bingham, J. L. Collier, E. J. Divall, P. S. Foster, C. J. Hooker, A. J. Langley, P. A. Norreys, R. A. Fonseca, F. Fiuza, L. O. Silva, J. T. Mendonça, W. B. Mori, J. G. Gallacher, R. Viskup, D. A. Jaroszynski, S. P. D. Mangles, A. G. R. Thomas, K. M. Krushelnick, and Z. Najmudin, *Evidence of photon acceleration by laser wake fields.* Physics of Plasmas, **13(3)**, 033108 (2006).

[94] J. Faure, Y. Glinec, A. Pukhov, S. Kiselev, S. Gordienko, E. Lefebvre, J.-P. Rousseau, F. Burgy, and V. Malka, *A laser–plasma accelerator producing monoenergetic electron beams.* Nature, **431(7008)**, 541 (2004).

[95] S. P. D. Mangles, C. D. Murphy, Z. Najmudin, a. G. R. Thomas, J. L. Collier, a. E. Dangor, E. J. Divall, P. S. Foster, J. G. Gallacher, C. J. Hooker, D. a. Jaroszynski, a. J. Langley, W. B. Mori, P. a. Norreys, F. S. Tsung, R. Viskup, B. R. Walton, and K. Krushelnick, *Monoenergetic beams of relativistic electrons from intense laser–plasma interactions.* Nature, **431(7008)**, 535 (2004).

[96] S. M. Hooker and C. E. Webb, *Laser Physics.* Oxford University Press, Oxford (2010).

[97] P. Maine, D. Strickland, P. Bado, M. Pessot, and G. Mourou, *Generation of Ultrahigh Peak Power Pulses by Chirped Pulse Amplification.* IEEE Journal of Quantum Electronics, **24(2)**, 398 (1988).

[98] G. S. Settles, *Schlieren and Shadowgraph Techniques: Visualizing Phenomena in Transparent Media.* Springer, New York, NY (2001).

[99] M. Deutsch, G. Hölzer, J. Härtwig, J. Wolf, M. Fritsch, and E. Förster, *$K\,\alpha$ and $K\,\beta$ x-ray emission spectra of copper.* Physical Review A, **51(1)**, 283 (1995).

[100] C. Hombourger, *An empirical expression for K-shell ionization cross section by electron impact.* Journal of Physics B: Atomic, Molecular and Optical Physics, **31(16)**, 3693 (1998).

[101] C. Reich, P. Gibbon, I. Uschmann, and E. Förster, *Yield Optimization and Time Structure of Femtosecond Laser Plasma $K\alpha$ Sources.* Physical Review Letters, **84(21)**, 4846 (2000).

[102] J. P. Santos, F. Parente, and Y.-K. Kim, *Cross sections for K-shell ionization of atoms by electron impact.* Journal of Physics B: Atomic, Molecular and Optical Physics, **36(21)**, 4211 (2003).

[103] L. C. Jarrott, M. S. Wei, C. McGuffey, F. N. Beg, P. M. Nilson, C. Sorce, C. Stoeckl, W. Theobald, H. Sawada, R. B. Stephens, P. K. Patel, H. S. McLean, O. L. Landen, S. H. Glenzer, and T. Döppner, *Calibration and characterization of a highly efficient spectrometer in von Hamos geometry for 7-10 keV x-rays*. Review of Scientific Instruments, **88(4)**, 043110 (2017).

[104] J. Hoszowska, J.-C. Dousse, J. Kern, and C. Rhême, *High-resolution von Hamos crystal X-ray spectrometer*. Nuclear Instruments and Methods in Physics Research Section A: Accelerators, Spectrometers, Detectors and Associated Equipment, **376(1)**, 129 (1996).

[105] C. M. Brenner, A. P. L. Robinson, K. Markey, R. H. H. Scott, R. Gray, M. Rosinski, O. Deppert, J. Badziak, D. Batani, J. R. Davies, S. M. Hassan, K. L. Lancaster, K. Li, I. O. Musgrave, P. A. Norreys, J. Pasley, M. Roth, H.-P. Schlenvoigt, C. Spindloe, M. Tatarakis, T. Winstone, J. Wolowski, D. Wyatt, P. McKenna, and D. Neely, *High energy conversion efficiency in laser-proton acceleration by controlling laser-energy deposition onto thin foil targets*. Applied Physics Letters, **104(8)**, 081123 (2014).

[106] C. M. Brenner, *Laser-Driven Proton Beams: Mechanisms for spectral control and efficiency enhancement*. Thesis, University of Strathclyde (2012).

[107] T. Matsuoka, C. McGuffey, M. Levin, S. S. Bulanov, V. Chyvkov, G. Kalintchenko, S. Reed, P. Rousseau, V. Yanovsky, A. Zigler, K. M. Krushelnick, and A. Maksimchuk, *Self-guided laser wakefield acceleration using ablated plasma targets*. Plasma Physics and Controlled Fusion, **51(9)**, 095003 (2009).

[108] J. Faure, C. Rechatin, A. Norlin, A. Lifschitz, Y. Glinec, and V. Malka, *Controlled injection and acceleration of electrons in plasma wakefields by colliding laser pulses*. Nature, **444(7120)**, 737 (2006).

[109] K. Nakamura, B. Nagler, C. Toth, C. G. R. Geddes, C. B. Schroeder, E. Esarey, W. P. Leemans, A. J. Gonsalves, and S. M. Hooker, *GeV electron beams from a centimeter-scale channel guided laser wakefield accelerator*. Physics of Plasmas, **14(5)**, 056708 (2007).

[110] J. Vieira, W. B. Mori, and P. Muggli, *Hosing Instability Suppression in Self-Modulated Plasma Wakefields*. Physical Review Letters, **112(20)**, 205001 (2014).

[111] T. C. Chiou, T. C. Katsouleas, C. Decker, W. B. Mori, J. S. Wurtele, G. Shvets, and J. J. Su, *Laser wakefield acceleration and optical guiding in a hollow plasma channel*. Physics of Plasmas, **2(1)**, 310 (1995).

[112] S. E. Segre, *A review of plasma polarimetry - theory and methods*. Plasma Physics and Controlled Fusion, **41(2)**, R57 (1999).

[113] K. A. Tanaka, R. Kodama, H. Fujita, M. Heya, N. Izumi, Y. Kato, Y. Kitagawa, K. Mima, N. Miyanaga, T. Norimatsu, A. Pukhov, A. Sunahara, K. Takahashi, M. Allen, H. Habara, T. Iwatani, T. Matusita, T. Miyakosi, M. Mori, H. Setoguchi, T. Sonomoto, M. Tanpo, S. Tohyama, H. Azuma, T. Kawasaki, T. Komeno, O. Maekawa, S. Matsuo, T. Shozaki, K. Suzuki, H. Yoshida, T. Yamanaka, Y. Sentoku, F. Weber, T. W. Barbee, and L. DaSilva, *Studies of ultra-intense laser plasma interactions for fast ignition*. Physics of Plasmas, **7(5)**, 2014 (2000).

[114] S. Palaniyappan, B. M. Hegelich, H.-C. Wu, D. Jung, D. C. Gautier, L. Yin, B. J. Albright, R. P. Johnson, T. Shimada, S. Letzring, D. T. Offermann, J. Ren, C. Huang, R. Hörlein, B. Dromey, J. C. Fernandez, and R. C. Shah, *Dynamics of relativistic transparency and optical shuttering in expanding overdense plasmas.* Nature Physics, **8(10)**, 763 (2012).

[115] L. Willingale, P. M. Nilson, C. Zulick, H. Chen, R. S. Craxton, J. Cobble, A. Maksimchuk, P. A. Norreys, T. C. Sangster, R. H. H. Scott, and C. Stoeckl, *Relativistic intensity laser interactions with low-density plasmas.* Journal of Physics: Conference Series, **688**, 012126 (2016).

[116] S. Ivancic, D. Haberberger, H. Habara, T. Iwawaki, K. S. Anderson, R. S. Craxton, D. H. Froula, D. D. Meyerhofer, C. Stoeckl, K. A. Tanaka, and W. Theobald, *Channeling of multikilojoule high-intensity laser beams in an inhomogeneous plasma.* Physical Review E, **91(5)**, 051101 (2015).

[117] G. Li, R. Yan, C. Ren, J. Tonge, and W. B. Mori, *Three-dimensional particle-in-cell simulations of laser channeling in fast ignition.* Physics of Plasmas, **18(4)**, 042703 (2011).

[118] B. Cohen, A. J. Kemp, and L. Divol, *Simulation of laser–plasma interactions and fast-electron transport in inhomogeneous plasma.* Journal of Computational Physics, **229(12)**, 4591 (2010).

[119] S. Chawla, M. S. Wei, R. Mishra, K. U. Akli, C. D. Chen, H. S. McLean, A. Morace, P. K. Patel, H. Sawada, Y. Sentoku, R. B. Stephens, and F. N. Beg, *Effect of Target Material on Fast-Electron Transport and Resistive Collimation.* Physical Review Letters, **110(2)**, 025001 (2013).

[120] L. Gremillet, G. Bonnaud, and F. Amiranoff, *Filamented transport of laser-generated relativistic electrons penetrating a solid target.* Physics of Plasmas, **9(3)**, 941 (2002).

[121] M. Tatarakis, J. R. Davies, P. Lee, P. A. Norreys, N. G. Kassapakis, F. N. Beg, A. R. Bell, M. G. Haines, and A. E. Dangor, *Plasma Formation on the Front and Rear of Plastic Targets due to High-Intensity Laser-Generated Fast Electrons.* Physical Review Letters, **81(5)**, 999 (1998).

[122] L. Willingale, P. M. Nilson, A. G. R. Thomas, J. Cobble, R. S. Craxton, A. Maksimchuk, P. A. Norreys, T. C. Sangster, R. H. H. Scott, C. Stoeckl, C. Zulick, and K. M. Krushelnick, *High-Power, Kilojoule Class Laser Channeling in Millimeter-Scale Underdense Plasma.* Physical Review Letters, **106(10)**, 105002 (2011).

[123] Y. Uematsu, S. Ivancic, T. Iwawaki, H. Habara, A. L. Lei, W. Theobald, and K. A. Tanaka, *Measuring the strong electrostatic and magnetic fields with proton radiography for ultra-high intensity laser channeling on fast ignition.* Review of Scientific Instruments, **85(11)**, 11E612 (2014).

[124] J. A. Delettrez and E. B. Goldman, *Numerical modeling of suprathermal electron transport in laser-produced plasmas. Report number 36.* Technical Report 36, Office of Scientific and Technical Information, Oak Ridge, TN (1976).

[125] T. R. Dittrich, O. A. Hurricane, D. A. Callahan, E. L. Dewald, T. Döppner, D. E. Hinkel, L. F. Berzak Hopkins, S. Le Pape, T. Ma, J. L. Milovich, J. C. Moreno, P. K. Patel, H.-S. Park, B. A. Remington, J. D. Salmonson, and J. L. Kline, *Design of a High-Foot High-Adiabat ICF Capsule for the National Ignition Facility*. Physical Review Letters, **112(5)**, 055002 (2014).

[126] J. L. Peterson, D. S. Clark, L. P. Masse, and L. J. Suter, *The effects of early time laser drive on hydrodynamic instability growth in National Ignition Facility implosions*. Physics of Plasmas, **21(9)**, 092710 (2014).

[127] J. D. Lindl, P. Amendt, R. L. Berger, S. G. Glendinning, S. H. Glenzer, S. W. Haan, R. L. Kauffman, O. L. Landen, and L. J. Suter, *The physics basis for ignition using indirect-drive targets on the National Ignition Facility*. Physics of Plasmas, **11(2)**, 339 (2004).

[128] B. Ramakrishna, S. Kar, A. P. L. Robinson, D. J. Adams, K. Markey, M. N. Quinn, X. H. Yuan, P. McKenna, K. L. Lancaster, J. S. Green, R. H. H. Scott, P. A. Norreys, J. Schreiber, and M. Zepf, *Laser-Driven Fast Electron Collimation in Targets with Resistivity Boundary*. Physical Review Letters, **105(13)**, 135001 (2010).

[129] L. Liao, W. Wu, C. Wang, M. Zhou, Z. Fu, and Y. Tang, *The collimation of intense relativistic electron beams generated by ultra-intense femtosecond laser in nanometer-scale solid fiber array*. Applied Physics Letters, **104(8)**, 083520 (2014).

[130] A. P. L. Robinson, D. J. Strozzi, J. Davies, L. Gremillet, J. J. Honrubia, T. Johzaki, R. Kingham, M. Sherlock, and A. A. Solodov, *Theory of fast electron transport for fast ignition*. Nuclear Fusion, **54(5)**, 054003 (2014).